

Structure-Property Correlation Studies of Carbonate Fluorides and Metal-Organic Energetic Solids

A Thesis submitted to University of Hyderabad for the award of
the degree of

Doctor of Philosophy

in Physics

by

Elaprolu Narsimha Rao

(10ACPP21)



ACRHEM, School of Physics

University of Hyderabad

Hyderabad-500 046

Telangana, India.

August 2018

Dedicated To
My Beloved Parents & Family
“for their love, endless support, encouragement & sacrifices”
(Parents:Shri. E. Ramamurthy-Vemkamma)
&
(Bother: Mr. E. Sreenivasa Rao-Rani)
&
(Sister: Mrs. R. Shireesha-Pulla Rao, Bhuvika)
&
(My Wife: Mrs. E. Bhavana Narsimha Rao)

Declaration

I, Elaprolu Narsimha Rao, hereby declare that the work presented in this thesis entitled “*Structure-Property Correlation Studies of Carbonate Fluorides and Metal-Organic Energetic Solids*” has been carried out by me under the supervision of Dr. G. S. Vaitheeswaran, ACRHEM, School of Physics, University of Hyderabad, Hyderabad, Telangana, India, as per the Ph.D. ordinances of the University. I declare, to the best of my knowledge, that no part of this thesis has been submitted for the award of a research degree of any other University. I hereby agree that my thesis can be deposited in Shodhganga/INFLIBNET.

(Elaprolu Narsimha Rao)
Reg. No: 10ACPP21.

Dr. G. S. Vaitheeswaran,
Thesis Supervisor,
ACRHEM, School of Physics,
University of Hyderabad.

Certificate

This is to certify that the thesis entitled “*Structure-Property Correlation Studies of Carbonate Fluorides and Metal-Organic Energetic Solids*” being submitted to the University of Hyderabad by **Elaprolu Narsimha Rao** (Reg. No. 10ACPP21), for the award of the degree of Doctor of Philosophy in Physics, is a record of *bonafide* work carried out by him under my supervision and is free of plagiarism. The matter embodied in this report has not been submitted to any other University or Institution for the award of any degree or diploma.

Further, these studies have the following publications before submission of the thesis for adjudication and have produced evidence for the same in the form of acceptance letter or the reprint in the relevant area of his research:

1. Elaprolu Narsimha Rao, S. Appalakondaiah, Yedukondalu Neelam, Ganapathy Vaitheeswaran, “Structural, electronic and optical properties of novel carbonate fluorides $ABCO_3F$ (A=K, Rb, Cs; B=Ca, Sr)”. Journal of Solid State Chemistry 2014, 212 (0), 171-179, Chapter of the dissertation where this publication appears Chapter 3.
2. E. Narsimha Rao, G. Vaitheeswaran, A. H. Reshak and S. Auluck, “Effect of lead and caesium on the mechanical, vibrational and thermodynamic properties of hexagonal fluorocarbonates: A comparative first principles study”, RSC Advances, 2016, 6, 99885-99897, Chapter of the dissertation where this publication appears Chapter 4.
3. E. Narsimha Rao, A. H. Reshak, S. Auluck and G. Vaitheeswaran, “Role of spin-orbit interaction on the nonlinear optical response of $CsPbCO_3F$ using DFT”, Physical Chemistry Chemical Physics, 2017, 19, 31255-31266, Chapter of the dissertation where this publication appears Chapter 5.

and has made presentations in the following conferences

1. Presented a poster entitled “First Principle Study of Carbonate Fluorides $ABC O_3F$ (A = K,Rb,Cs; B=Ca,Sr) : A New Class of NLO Materials” E.Narsimha Rao and G. Vaitheeswaran during Winter school held at JNCASR, Bangalore, during January-2015, India.
2. Presented a poster entitled “First Principle Study of Carbonate Fluorides $ABC O_3F$ (A = K,Rb,Cs; B=Ca,Sr) : A New Class of NLO Materials” E.Narsimha Rao and G. Vaitheeswaran during Workshop entitled “Workshop on Development of Binders and Plasticisers for Energetic Applications” held at ACRHEM, University of Hyderabad, Hyderabad, Telangana, India on December-2015.

Further the student has passed the following courses towards the fulfilment of course work requirement for PhD.

S.No.	Course Code	Name of the course	Credits	Pass/Fail
1	AC801	Laser Primer	02	Pass
2	AC803	Electronic Structure Theory	02	Pass
3	AC804	Combustion-I	02	Pass
4	AC805	Matlab	02	Pass
5	AC829	Electronic Structure Theory-2	02	Pass
6	AC807	Research methodology	04	Pass
7	MT806	Concepts & Material Science	04	Pass

Dr. G. S. Vaitheeswaran,
Thesis Supervisor,
ACRHEM, School of Physics,
University of Hyderabad.

Director,
ACRHEM,
University of Hyderabad.

Dean,
School of Physics,
University of Hyderabad.

A word of Gratitude

It is a great pleasure to express my heartfelt thanks to each and everyone who have helped me directly and indirectly to the successful completion of my doctoral thesis work. I always believe in “Maathru Devo Bhava!!! Pithru Devo Bhava!!! Acharya Devo Bhava!!! Athidhi Devo Bhava!!!”, so I feel blessed to start with a short note about my parents, younger brother, younger sister for their struggle and hard work to bring me to this stage. I can't be able to convey full details about this here, but I can do it in my book “I am Yours Struggle”. This thesis represents not only my work at the computer, it is a milestone in 14 years of my family members struggle after leaving our village with empty hands and heavy hearts. I still remember my family members silent tears and empty thoughts on that full moon day (Purnima) in the year of 2004. Even in that kind of painful situations also, my parents commitment and encouragement to make three of us study gave a real motivation which will never fadeout from our hearts. I remember each and every day of my parents struggles followed by many sleepless nights with empty stomach. My talented brother and lovely sister who got enough maturity in thoughts at their early age itself and they use to warn me when I loose my focus like a elder brother and sister. I always feel proud of my brother and sister who played a bigger role than me in saving our family. My brother is now M.Com holder and sister is M.Sc,B.Ed (Maths) holder. That is why not only my present thesis work, but whatever I achieve in future also, I firstly dedicate to these four. This doctorate they earned through me. I can proudly say that, by doing small watchman job and daily work in an apartment, my parents brought us to this stage. Since last two years (during my de-registration period) they continued to send money to make me study here without fellowship. These people are role models not only to me but they can be role models to the society. That's why I express my deep love from the bottom of my heart by calling them with a honorary doctorate as Dr. Elaprolu Ramamurthy, Dr. Elaprolu Vemkamma, Dr. Elaprolu Sreenivasa Rao, Dr. Elaprolu Shireesha (before marriage). Love you all. If god blesses us with some good opportunities in future, I would like to introduce you all to this world by achieving something remarkable in some field and through my book also.

I would like to thank Defence Research and Development Organisation **DRDO**, Ministry of Defence Govt. of India through **ACRHEM** for their financial support. I would like to acknowledge the present director **Shri Dr. Anil Kumar Aggarwal**, present acting director Prof. Anil Kumar Chaudhary and former directors (Prof. S. P. Tewari, Dr. K. Sethuva, Dr. K. Venkateswara Rao) and former acting directors (Prof. Ramakrishna Ramaswamy (former Vice chancellor, UOH), Prof. S. Venugopal Rao, Prof. M. Durga Prasad) of ACRHEM,

present dean School of Physics **Prof. Bindu Anubha Bambah** and past dean's for administrative support.

There are many people that I would like to thank for their kind support and encouragement since I have joined University of Hyderabad. First I extend my gratitude to **Prof. S. P. Tewari**, my previous supervisor (during August/2010 to August/2012) and former director of ACRHEM, through whom I got introduced to the field of research after finishing my M.Sc. He inspired me in many ways and taught basics about how to do research, how to choose a research problem etc. I worked as a experimental research scholar under his supervision from 30th Aug. 2010 to 30th Aug. 2012. Initially we planned to do high pressure experiments on high energy materials using Diamond Anvil Cell (DAC). As a part of this project, we performed our initial experiments on ammonium nitrate with available piston-cylinder experimental set-up in school of physics. We also initiated to perform other few experiments to study the phase morphology and hygroscopic reduction of ammonium nitrate by adding foreign salts to it. But, due to superannuation of Prof. S.P. Tewari in 2012, he was unable to guide me for further experimental work. Since there are no experimental positions available at that time in ACRHEM, I approached **Dr. G. S. Vaitheeswaran** (my present thesis supervisor) and asked to guide me further. He accepted and agreed to guide me in the theoretical studies of energetic materials by stopping experimental work. From August, 2012 I freshly started working on new problem entitled "Structure-Property Correlation Studies of Carbonate Fluorides and Metal-Organic Energetic Solids". Now I am submitting my theoretical research work under the supervision of Dr. G. S. Vaitheeswaran. I cannot forget his help in my difficult situations and I don't have words to express my gratitude and it is a matter of pride to have association with him. Most importantly, I would like to thank my thesis supervisor Dr. G. S. Vaitheeswaran for introducing me to the world of modelling and simulations using Density Functional Theory simulations and his constant guidance throughout the research work. This dissertation would not have been possible without his assistance, allowed me to discuss through user forums and experts in this field of research. I knew thanks itself is not sufficient. A special thanks to **Prof. M. C. Valsakumar**, IIT Palkkad, India, who gave further confidence in me during his stay in University of Hyderabad through his various theoretical classes, tutorials and valuable discussions on density functional theory. I always feel happy and lucky that I got a chance to be associated with him and listen to his classes, suggestions both in professional and personal level. I also thank Mrs. M. C. Valsakumar and other family friends for providing homely-hood at my working place Hyderabad.

I would like to thank my doctoral committee members **Dr. P. Prem Kiran**

and **Dr. G. Manoj Kumar**, ACRHEM, University of Hyderabad, for their continuous support (from 2010 to till today), valuable suggestions and critical comments during my experimental and theoretical works. Even though my topic of research work changed, these both showed their enormous patience and constantly encouraged during my doctoral committee presentations. I can't forget their help towards the completion of my doctoral research work.

I extend my gratitude to **Prof. S. Auluck**, Council of Scientific and Industrial Research - National Physical Laboratory, New Delhi, India and **Prof. Ali H. Reshak**, New Technologies-Research Center, University of West Bohemia, Czech Republic, for their crucial collaboration, fruitful suggestions for my manuscripts which are included in the thesis. I also would like to thank the **anonymous reviewers** for reviewing my publications to improve the quality of the research work. I am extremely thankful to other faculty members of ACRHEM **Prof. S. Venugopala Rao**, **Prof. A. K. Chowdary**, **Dr. Ashok Balakrishnan**, **Dr. Ashok Vudayagiri**, **Prof. K. C. James Raju**, **Prof. M. Ghanasyam Krishna** and **Dr. Anuj A. Vargese** for teaching me the concepts of research methodology, MATLAB, Laser primer, Combustion, Nonlinear Optics discussions, providing experimental facilities and High Energy Materials. My sincere thanks to **Dr. Dibakar Das** who taught me Concepts of Material science. My special thanks to **Prof. C. S. Sunandana** for his valuable suggestions while correcting my manuscripts. I also would like to thank other collaborator **Mr. P. Anees**, IGCAR, Kalpakkam, India. I also thank **all non-teaching staff of ACRHEM, School of Engineering Sciences & Technology** as well as **School of Physics** for their help in office related work. Last but not least, I would like to thank **CMSD** for providing me the computational facilities and **SoP, SoC, SEST (Nano Science and Technology)**, CIL University of Hyderabad for providing experimental facilities.

It has been a very pleasant experience to work in the warm and friendly atmosphere of my group members **Dr. S. Appalakondaiah**, **Dr. N. Yedukondalu**, **Dr. K. Ramesh Babu**, **Dr. Ch. Bheemalingam**, **S. Mondal**, **J. Prathap Kumar**, **J. Adivaiah**, **B. M. Abraham**, **Dr. Athar Parveen**, all **M.Tech** and **M.Sc project students**. Thank you as well to all simulation group members of the IIT-Hyderabad (**Dr. P. V. Sreenivasa Reddy**, **Dr. G. Shwetha**, **Mrs. P. C. Sreeparvathy**, **Dr. Swetarekha Ram** and **Dr. G. Vijay kumar**) for making the time during this period so enjoyable. I also thank my experimental group colleagues **Mr. Ch. Sreenivasulu**, **Mrs. Manasa**, **Dr. Ravi Prakash**, **Dr. D. Sreenivas** and I also remember **Dr. Sudha N. Kalagata (late)** and **Mr. M. Venkatesh (late)** and I pray to GOD for their eternal peace. I would like to thank all (> 100) my **ACRHEM, School of Physics, Chemistry, Mathemat-**

ics, Engineering Sciences & Technology and Humanities, School of Nano Science & Technology, Shivam hostel and UV-Physics Academy friends and SSC, Inter, Degree, MSc friends and other PhD colleagues from various labs in India, SR & BGNR Govt College physics faculty, Khammam for their help and support whenever I needed. I also would like to thank SERB School organizing committee on “Materials Modeling and Simulation across Length Scale” at Physics Department, University of Mumbai during December, 2013 & Winter School organizing committee on “Materials and Processes for Applications in Energy and Environment” during January, 2015 at JNCASR, Bangalore & CECAM ABINIT dynamical properties school organizing committee May-2014 in Lyon for accepting my application for the participation.

I love to mention my heartfelt thanks to my paternal grand parents **Elaprolu Gopaiah, Elaprolu Vemkamma** & my maternal grand parents **T. Narsimha(late), T. Seethamma (late)** for their love, every moral support and I pray to GOD for my maternal grand parents eternal peace. I have to mention my special and sincere thanks with love to my wife **E. Bhavana (B.E. Civil)**, sister-in-law **R. Ankitha** & her family members, sister-in-law **E. Rani (B.Sc, B.Ed)** & family members, brother in-law **Mr. R. Pulla Rao (FCI)** & family members and blood relatives brothers (**E. Ravi & family members, E. Krishna & family members, E. Rama Krishna & family members**), sisters (**Shireesha, Nagamani & family members**), relatives (**T. Rampandu & Lakshmi, G. Krishna Rao & Chandrakala, R. Srinu & Savtri, T. Gopaiah & Danamma, E. Narsimha (late)& Chilakamma, Raghavalu (late) & Lakshmi (late), E. Srinu Kamala, T. Krishnaiah, T. Muttaiah & all family members**), and family well wishers from CRG-Enclave: **Dr. Ragesh Garge & family members, Ch. Venugopala Rao (my Physics teacher) & family members, P. Sheshagiri Rao (my Maths teacher) & family members, M. Venkat Reddy & family members, P. Ravi garu & family members, SK Maulali (late) & family members, M. Venkateswara Rao & family members, P. Narsimha Reddy & family members, Ramakrishna garu & family members, Anand jain & family members, Ch. Ravi & family members, Rama Rao garu (late) & family members, K. Vasu garu & family members, Dinesh Jain & family members, Rajendhar garu & family members, Sarath garu & family members etc** and my beloved tuition sir **Shri. Veerabadra Chari garu & family members**, school, college teachers and other well wishers from my Pinapaka village, Thallada (MD) for their encouragement and moral support. My special special and special love to my daughter in-law (sisters daughter (new-born)) **R. Bhuvika (Gundu)** who came to this world on 21st Feb, 2017 and make us (me and my brother) to get married to her own aunts by next year 24th Feb, 2018.

Elaprolu Narsimha Rao

Contents

Contents	i
List of figures	iii
List of tables	vii
1 Introduction	1
1.1 Motivation	1
1.1.1 Non-linear optical (NLO) materials	1
1.1.2 High energy materials (HEM)	6
1.1.3 Scope of the thesis	8
2 Theoretical methods	15
2.1 Solids: A many-body problem	15
2.2 Density functional theory	19
2.2.1 The local-density approximation (LDA)	22
2.2.2 The generalised gradient approximation (GGA)	23
2.2.3 Dispersion correction methods	23
2.2.4 Tran-Blaha modified Becke-Johnson potential (TB-mBJ)	25
2.3 Density functional perturbation theory	27
2.3.1 General spectroscopic properties	30
2.4 Methodology	33
2.4.1 Pseudopotential method	33
2.4.2 Augmented Plane Wave (APW) method	34
2.4.3 Linearized Augmented Plane Wave (LAPW) method	35
2.4.4 APW+lo method	36
3 Alkali-Alkaline Carbonate Fluorides	43
3.1 Introduction	43
3.2 Calculation methods	45
3.3 Results and discussion	47

3.3.1	Structural and elastic properties	47
3.3.2	Electronic band structure	50
3.3.3	Optical properties	54
3.4	Conclusions	59
4	Lead Carbonate Fluoride CsPbCO₃F	67
4.1	Introduction	67
4.2	Calculation methods	69
4.3	Results and discussion	71
4.3.1	Structural, elastic and polycrystalline properties	71
4.3.2	Born effective charges (BEC) and static polarization	78
4.3.3	Vibrational modes and symmetry analysis	81
4.3.4	Thermodynamic properties	85
4.4	Conclusions	93
5	Role of spin-orbit interaction on optical response of CsPbCO₃F	99
5.1	Introduction	100
5.2	Calculation methods	102
5.3	Results and discussion	104
5.3.1	Electronic band structure and density of states (DOS)	104
5.3.2	Linear optical properties and birefringence	109
5.4	Conclusions	115
6	Structure-property correlation studies of K₂BDAF	121
6.1	Introduction	122
6.2	Calculation methods	124
6.3	Results and discussion	126
6.3.1	Crystal structure and mechanical stability	126
6.3.2	Born effective charges and vibrational properties	133
6.3.3	Phonon dispersion and thermodynamic properties	139
6.3.4	Electronic band structure and density of states	146
6.3.5	Linear optical properties and birefringence	150
6.4	Conclusions	155
7	Summary and future scope	163
7.1	Summary	163
7.2	Future scope	165
	List of publications	169

List of Figures

3.1	Experimental crystal structure of a) KCaCO_3F , b) KSrCO_3F , c) RbSrCO_3F , d) RbCaCO_3F and e) CsCaCO_3F	48
3.2	Calculated electronic band structure of (a) KCaCO_3F , KSrCO_3F and RbSrCO_3F , (b) RbCaCO_3F and CsCaCO_3F using TB-mBJ functional at experimental crystal structures.	53
3.3	Calculated electronic DOS of (a) KCaCO_3F , (b) KSrCO_3F and (c) RbSrCO_3F using TB-mBJ functional at experimental crystal structures [36].	54
3.4	Calculated electronic DOS of (a) RbCaCO_3F , (b) CsCaCO_3F using TB-mBJ functional at experimental crystal structures [36]	54
3.5	Charge density difference plot for KCaCO_3F , KSrCO_3F , RbSrCO_3F along $[0\ 0\ 1]$	55
3.6	Complex dielectric function of (a) KCaCO_3F , KSrCO_3F and RbSrCO_3F , (b) RbCaCO_3F and CsCaCO_3F calculated using TB-mBJ functional at experimental crystal structures[36].	56
3.7	Absorption and refractive indices of (a) KCaCO_3F , KSrCO_3F and RbSrCO_3F , (b) RbCaCO_3F and CsCaCO_3F calculated using TB-mBJ functional at experimental crystal structures.	58
4.1	Experimental crystal structure of CsPbCO_3F consist of CsF and PbCO_3 layers.	73
4.2	Calculated zone centre vibrational (IR) spectra in Far-IR, mid-IR, near IR regions of CsPbCO_3F and ABCO_3F (where $A = \text{K, Rb}$; $B = \text{Ca, Sr}$) (from left to right) at theoretical equilibrium structure.	86
4.3	Snapshots of different vibrational mode animations of carbonate fluorides materials.	87
4.4	Calculated thermodynamic properties enthalpy (H), free energy (F), entropy (S_V), heat capacity (C_V) and Debye temperature $\Theta(V)$ of carbonates at theoretical equilibrium structure up to 1000K temperature.	90

4.5	Calculated thermal conductivity (K) and thermal expansion (α) coefficients of carbonates at theoretical equilibrium structure . The K , α curves of KSr and RbSr are shifted upward by 1W/m K and $0.5(10^{-6}/\text{K})$ from the preceding curve for clarity.	91
5.1	Experimental crystal structures of CsPbCO_3F , RbSrCO_3F , KCaCO_3F , KSrCO_3F	103
5.2	Calculated electronic band structure with and without spin-orbit interaction effects of CsPbCO_3F at experimental crystal structure volume.	106
5.3	Calculated partial electronic band structure with and without spin-orbit interaction effects of CsPbCO_3F at experimental crystal structure volume.	107
5.4	Calculated DOS with and without spin-orbit interaction effects of CsPbCO_3F at experimental crystal structure volume.	108
5.5	Charge density difference plots of CsPbCO_3F along $[1\ 1\ 0]$ and $[1\ 0\ 1]$ planes from left to right.	108
5.6	Calculated real and imaginary parts of complex dielectric function with and without SOI effects of CsPbCO_3F at experimental crystal structure volume.	111
5.7	Calculated refractive index and absorption spectra with and without spin-orbit interaction effects of CsPbCO_3F at experimental crystal structure volume.	112
5.8	Calculated Birefringence of CsPbCO_3F with spin-orbit interaction effects, ABCO_3F ($A=\text{K, Rb}$; $B=\text{Ca, Sr}$) at experimental crystal structure volume.	115
6.1	Experimental crystal structure of Potassium 4,4'-Bis (dinitromethyl)-3,3'-azofurazanate ($\text{C}_6\text{N}_{10}\text{O}_{10}\text{K}_2$).	128
6.2	Experimental crystal structure of K_2BDAF and K_2DNABT (left to right) in y - z plane.	129
6.3	Experimental crystal structure of K_2BDAF and K_2DNABT (left to right) in x - y plane.	129
6.4	Snapshot images of few vibrational modes (M07 , M11 , M17 , M56 , M62 , M66 , M68 , M79 , M81 , M83) of K_2BDAF	143
6.5	Calculated IR-spectra of K_2BDAF , K_2DNABT crystal structures optimized at G06 level. Here, IR-spectra of K_2DNABT is recalculated as reported in "J. Chem. Phys, 143, 064508, 2015" and plotted on top of K_2BDAF IR-spectra for analysis purpose. . . .	144

6.6	Calculated total phonon density of states (top) and phonon dispersion curves (bottom) of K_2BDAF (red in color), K_2DNABT (blue in color) crystals optimized at G06 level, along the brillouin zone path $G(0\ 0\ 0) \rightarrow F(0\ 0.5\ 0) \rightarrow Q(0\ 0.5\ 0.5) \rightarrow Z(0\ 0\ 0.5) \rightarrow G(0\ 0\ 0)$	145
6.7	Calculated thermodynamic properties (Enthalpy (H), Entropy (S_V), Free energy (F), Heat capacity (C_V), $\Theta(V)$ Debye temperature) of K_2BDAF , K_2DNABT up to 1000K temperature at G06 level. . .	146
6.8	Calculated (a)partial density of states (DOS), (b) electronic band structure, (c) electron charge density maps of K_2BDAF crystal structure optimized at TB-mBJ level.	149
6.9	Calculated linear optical properties (real and imaginary parts of complex dielectric function; refractive index and absorption spectra) of K_2BDAF crystal structure at TB-mBJ level.	152
6.10	Calculated Birefringence of K_2BDAF and K_2DNABT at experimental crystal structure volume. Results are compared with $KCaCO_3F$, $KSrCO_3F$, $RbSrCO_3F$ and $CsPbCO_3F$ (with and without spin-orbit effects)[44].	153

List of Tables

3.1	The calculated ground state properties such as lattice parameters (a,c in Å) and volume (V in Å ³) of ABCO ₃ F (A = K, Rb, Cs; B = Ca, Sr) compounds using standard LDA, GGA and dispersion corrected (G06, OBS) exchange-correlational functionals along with the experimental data taken from Ref.36.	49
3.2	Calculated single crystal elastic constants (C _{ij} , in GPa), bulk modulus (B in GPa) of ABCO ₃ F (A = K, Rb, Cs; B = Ca, Sr) compounds calculated at the PW91+OBS theoretical equilibrium volume.	50
3.3	Calculated electronic band gaps (in eV) of ABCO ₃ F (A = K, Rb, Cs; B = Ca, Sr) compounds using with GGA-PBE, EV-GGA and TB-mBJ functionals within FP-LAPW method and compared with other calculations.	52
3.4	The observed optical transitions of ABCO ₃ F (A = K, Rb, Cs; B = Ca, Sr) from imaginary part of dielectric function using TB-mBJ electronic structure.	57
3.5	Linear optical properties such as real part of dielectric function (ε ₁ (ω)), absorption coefficient (α(ω)×10 ⁴ , cm ⁻¹), refractive indices (n _o and n _e) and birefringence (Δn) of ABCO ₃ F (A = K, Rb, Cs; B = Ca, Sr) compounds	59
4.1	Calculated ground state lattice vectors (a,c in Å), volume (V, in Å ³) of CsPbCO ₃ F, using LDA, PBE, PW91 and dispersion corrected PW91 (PW91+OBS) along with experimental data [8]	73
4.2	Calculated bond lengths (in Å) at OBS, PBE theoretical equilibrium structures of CsPbCO ₃ F and ABCO ₃ F (where A = K, Rb ; B = Ca,Sr) respectively along with experimental data[1, 8]	74
4.3	Calculated single crystal elastic constants C _{ij} ,bulk modulus B (in GPa units) of CsPbCO ₃ F for PBE,PW91,PW91+OBS theoretical equilibrium volume's	78

4.4	The Calculated bulk (B_X), shear moduli (G_X) values using the Voigt, Reuss, Hill approximations ($X=V,R,H$). Also listed the Poisson's ratio σ , B_H/G_H ratio. All values are calculated at the corresponding theoretical equilibrium volumes	79
4.5	Calculated values of c/a ratio, shear anisotropy factors (A_i)($i=1,2,3$), Young's modulus (E), crystal density (ρ), elastic-Debye temperature (Θ_D) at the theoretical equilibrium volumes	79
4.6	Calculated BEC's of Pb, Ca, Sr, F, Cs, Rb, K, C atoms at the theoretical equilibrium volume's along with previously reported [4] values in parenthesis	81
4.7	Calculated percentage of deviations of BEC's of Pb, Ca, Sr, F, Cs, Rb, K, C atoms at the theoretical equilibrium volumes	82
4.8	Calculated BEC's of O_1 , O_2 , O_3 atoms (have nominal ionic charge -2) at the theoretical equilibrium volumes	82
4.9	Calculated percentage of deviation's of BEC's of O_1 , O_2 , O_3 atoms from it's nominal ionic charge -2	82
4.10	The calculated zone centre high frequency vibrational modes (in cm^{-1}) of $CsPbCO_3F$ and $ABCO_3F$ (where $A = K, Rb$; $B = Ca, Sr$) and their assignments [Here I= IR active mode, R= Raman active mode]. Experimentally reported frequencies are given in parenthesis [1]	87
4.11	The calculated zone centre low frequency vibrational modes of $CsPbCO_3F$ and $ABCO_3F$ (where $A = K, Rb$; $B = Ca, Sr$) and their mode assignments [Here Trans.= Translation, Asymm.= Asymmetric, str.= Stretching]	88
4.12	The calculated thermal conductivities $k(W/m K)$ and thermal expansion coefficients $\alpha(10^{-6}/K)$ of carbonate fluorides at room temperature along with other hexagonal NLO materials data	92
5.1	Calculated energy band gaps of $CsPbCO_3F$ without and with inclusion of SOI at experimental volume. Results are compared with previously reported data.	105
5.2	The optical transitions of $CsPbCO_3F$ before and after inclusion of spin-orbit interactions observed from imaginary part of dielectric function and TB-mBJ band structure	111
5.3	Linear optical properties such as absorption coefficient ($\times 10^4 cm^{-1}$), refractive indices and birefringence of $KCaCO_3F$, $KSrCO_3F$ and $RbSrCO_3F$	111

5.4	The optical transitions of CsPbCO ₃ F derived from top of valence band to conduction band observed from imaginary part of dielectric function along [1 0 0]	113
5.5	The birefringence of CsPbCO ₃ F before and after inclusion of spin-orbit interactions obtained from imaginary part of dielectric function at TB-mBJ level. For comparison, birefringence of ABCO ₃ F (A=K, Rb; B=Ca, Sr) also calculated using our previous work[39]	114
5.6	The change in Born Effective charges (Δq) along x and z directions of different metal atoms of CsPbCO ₃ F, ABCO ₃ F (A=K, Rb; B=Ca, Sr)[28]	114
6.1	Calculated ground state lattice vectors (a, b and c, in Å), volume (V, in Å ³), density (ρ in gr/cc) of K ₂ BDAF, using LDA, PBE, PW91 and dispersion corrected PBE (PBE+G06), PW91 (PW91+OBS) along with experimental data [21]. The percentage of deviations in lattice parameters are given in parenthesis.	127
6.2	Calculated single crystal elastic constants C_{ij} and bulk modulus values for K ₂ BDAF, K ₂ DNABT using PBE+G06 theoretical equilibrium volume's.	131
6.3	The calculated polycrystalline elastic constants (bulk (B_X), shear moduli (G_X , B_H/G_H ratio) using the Voigt, Reuss, Hill approximations (X=V,R,H) and the Poisson's ratio σ , Young's modulus (E), micro hardness (H)). All values are calculated at the G06 equilibrium volumes	133
6.4	Calculated BEC's for all inequivalent atoms of K ₂ BDAF at the theoretical equilibrium volume (left side table). Actual ionic charges are O = -2, C = +4, K = +1, N = -3. Percentage of deviations of BEC's all inequivalent atoms are shown in (right side table) along xx, yy, zz directions.	135
6.5	Calculated BEC's for all inequivalent atoms of K ₂ DNABT at the theoretical equilibrium volume (left side table). Actual ionic charges are O = -2, C = +4, K = +1, N = -3. Percentage of deviations of BEC's all inequivalent atoms are shown in (right side table) along xx, yy, zz directions.	136
6.6	The calculated zone centre high frequency ($> 1000 \text{ cm}^{-1}$) vibrational modes of K ₂ BDAF and their mode assignments [Here Trans. = Translation, Asymm.= Asymmetric, str. = stretching]	140

6.7	The calculated zone centre mid frequency (from 300 cm^{-1} to 1000 cm^{-1}) vibrational modes and assignments of K_2BDAF [Here Trans. = Translation, Asymm.= Asymmetric, str. = stretching]	141
6.8	The calculated zone centre low frequency ($< 300\text{ cm}^{-1}$) vibrational modes of K_2BDAF and their mode assignments [Here Trans. = Translation, Asymm.= Asymmetric, str. = stretching]	142
6.9	Calculated energy band gaps of K_2BDAF at experimental crystal structure volume.	150
6.10	Linear optical properties such as absorption coefficient ($\times 10^4\text{ cm}^{-1}$), refractive indices and birefringence of K_2BDAF and K_2DNABT	151
6.11	The change in Born Effective charges along y-z (for K_2BDAF), z-y (for K_2DNABT) directions of different atoms.	153

Introduction

1.1 Motivation

In the present day scenario, human life is significantly dependent on various class of materials. Among them, two important class of materials (i.e. 1. Semiconducting optical materials 2. High energy materials (HEM)) are chosen for this present study. The semiconducting materials play a major role in developing new devices for modern photonic technologies [1, 2], whereas HEM's find applications in civil and military for homeland security purposes [3, 4]. Our quest is to explore them by performing different experimental, theoretical studies and design novel, efficient materials to develop compact devices that are required in everyday life. Hence, the structure-property correlations of recent technologically important nonlinear optical materials and newly synthesized high energy materials were explored in this thesis using density functional theory (DFT) simulations. A brief introduction to these materials was given in the next section.

1.1.1 Non-linear optical (NLO) materials

It is well known that, when an electromagnetic (EM) wave is focused on to a dielectric material, the propagation of EM wave will disturb the spatial and temporal electronic charge distribution of the constituent atoms. The resultant dipole moments create polarization in the material. Therefore the optical response of a material to the applied electric field (E) can be understood in terms of polarization (P) as

$$P \propto \epsilon_0 \times E \quad (1.1)$$

Here ϵ_0 is the permittivity of free space ($8.85418 \times 10^{-12} \text{ C}^2.\text{N}^{-1}.\text{m}^{-2}$ or $\text{C.V}^{-1}.\text{m}^{-1}$). It is known that electric field intensity due to bright sunshine (light source) is of 600 V.m^{-1} [5, 6]. Whereas, electric field due to the binding electron of Hydrogen atom can be written as

$$E_{atom} = \frac{1}{4\pi\epsilon_0} \frac{e}{a_0^2} \quad (1.2)$$

Here a_0 is the distance (Bohr radius) between the electron and the nucleus of Hydrogen atom.

$$a_0 = \frac{\hbar^2}{m \times e^2} \quad (1.3)$$

Here 'e' (electron charge) = $1.6 \times 10^{-19} \text{ C}$, 'm' is electron mass = $9.1 \times 10^{-28} \text{ gm}$, $\hbar = \frac{h}{2\pi} = 1.05457 \times 10^{-34} \text{ J.S}$. The resultant electronic intensity is equal to $5 \times 10^{11} \text{ V.m}^{-1}$ which is greater than the electronic intensity of the bright sunshine [6]. With this available light sources, it is possible to study only the linear polarization of a given crystal. But after the invention of laser in 1960 [9], it became possible to obtain 10^7 V.m^{-1} by focussing the high intensity laser beam (Ruby 694.3 nm) on to a quartz crystal. This experiment revealed the possibility of creating 10^{11} higher order (second) harmonic (347.15 nm) photons per pulse of incident wavelength [10]. The principle of superposition is no longer valid and polarization becomes nonlinear. Therefore polarization P can be written as,

$$P(E) = \epsilon_0[\chi^{(1)}E + \chi^{(2)}E + \chi^{(3)}E + \dots] \quad (1.4)$$

Here $\chi^{(2)}$, $\chi^{(3)}$ are known as second and third order dipole susceptibilities. Then, the nonlinear optical (NLO) polarization became interesting phenomena which arise due to the incident of high intensity laser radiation (order of $\geq 10^{10} \text{ V.m}^{-1}$) on to the crystal [7]. The even-order dipole susceptibilities are found to occur only in crystals that lack an inversion symmetry (noncentrosymmetric (NCS) materials). The magnitude of these susceptibilities mainly depends on the frequency of the electric field, chemical composition, crystal symmetry. The well known types of nonlinear phenomena's are second, third, high-harmonic generations,

difference frequency generation (DFG), optical rectification, Kerr effects and etc. These nonlinear effects have large scientific, medical and industrial applications by generating unknown coherent wavelengths in visible, ultraviolet (UV), deep-UV, infrared (IR) and even in terahertz (THz) regions [8]. The visible and UV lasers have applications in high-precision spectral analysis, data storage, optical communications and medical surgeries. The deep-UV lasers have applications in laser micromachining, semiconductor photolithography, material processing, photochemical synthesis and angle resolved photoemission spectroscopy [6–8]. Even though excimer lasers serve to emit isolated UV and deep-UV wavelengths with high output power, efficient and compact solid-state lasers with suitable nonlinear crystals are still needed in this region [6–8]. The IR lasers found applications in remote sensing and optical communications. Hence the invention of novel NLO crystals with good performances in all these spectral regions has huge demand. An efficient NLO material must possess the following properties [6–8] to generate the coherent wavelengths in different regions: (1). In UV and deep-UV region: large energy band gap (E_g) for UV transparency and larger high laser damage threshold (LDT), large second harmonic generation (SHG) coefficient ($d_{ij} > \text{KDP}$ ($d_{36} = 0.39 \text{ pm/V}$)) to get high conversion efficiency, suitable birefringence ($\Delta n = |n_o - n_e|$ (> 0.06 for UV and > 0.075 for deep UV)) to achieve proper phase matching condition. (2). In IR region: to achieve similar conversion efficiency as UV NLO materials the IR NLO material must possess $d_{ij} > 10 \times \text{KDP}$. The $\Delta n \sim 0.06$ and $\text{LDT} \sim 100 \text{ MW/cm}^2$ ($E_g \sim 3.0 \text{ eV}$). But, the larger birefringence would lead to larger walk-off angle and self focusing effect, which will lead to reduction in the conversion efficiency and sustainability of the material. Similarly, it is known that many explosive materials have strong absorption in 0.3-10 THz region in the optical spectra [11]. In order to detect them for homeland security purposes, new generation and detection methods of THz frequencies using NLO processes are in great need. Moreover, the larger band gap value results in reducing the NLO response of the crystal. Another practical difficulty is to synthesize a noncentrosymmetric crystal in larger sizes [12, 13]. Therefore achieving all these properties in the same crystal, which has good optical quality, larger in size (few centimeters), with good chemical and mechanical

stability within low cost is a difficult task. Hence there is significant importance to study the structure-property correlations of these materials in each and every point of view to design new NLO crystals and this kind of studies would provide a path to the experimental explorations.

Over the past few decades, researchers are trying to understand the chemical composition, micro structure and optical response mechanism of various NLO materials. The Chen's anionic group theory [14] is one of the well known theoretical models which is used to study the structure-property correlation studies of NLO materials. This theorem states that, "the overall nonlinearity of NLO crystal is equal to the geometrical superposition of the microscopic $\chi^{(2)}$ NLO-active anionic group". The change in chemical composition, increasing the density of relevant nonlinear functional group and adjusting the orientation of these structural units in the material are the basic underlying criteria's for the invention of new NLO crystals. A crystal with high density NLO-structural units with a good co-parallel alignment is known to give higher nonlinear coefficients. Till now few hundreds of NLO crystals (Organic, inorganic and semi-organic) are developed to reach the scientific and industrial needs [12, 13]. The anionic group, which have planar triangular structure with conjugated π -orbitals are known to be the source of larger SHG coefficients.

The well known inorganic NLO materials [1, 12, 13] are CsB₃O₅ (CBO), LiB₃O₅ (LBO), CsLiB₆O₁₀ (CLBO), β -BaB₂O₄ (BBO), Sr₂Be₂B₂O₇ (SBBO), KBe₂B₃F (KBBF), Rare-earth-borate crystals, KH₂PO₄ (KDP), KTiOPO₄ (KTP), LiNbO₃, KNbO₃, etc. Among the borates crystals family which are made up of [BO₃]³⁻, [BO₄]⁵⁻, [B₃O₆]³⁻, [B₄O₉]⁶⁻ anionic groups, the [BO₃]³⁻ structural unit compounds are found to show promising applications in UV and deep-UV regions. These materials are mostly ionic bonded solids and possess good birefringence (for example LBO - 0.04; CLBO - 0.052; BBO - 0.12; KBBF - 0.072; SBBO - 0.062), large nonlinear coefficients (LBO: $d_{31} = 0.67$, $d_{32} = 0.85$, $d_{33} = 0.04$ pm/V; BBO: $d_{22} = 2.3$ pm/V; KBBF: $d_{31} = 0.16$ pm/V), high melting point (for example CLBO-1115 K; RECOB-1683 K, 1753 K, 1783 K), large LDT value (RECB - 11.5 GW/cm²), good UV transparency (~ 150 nm). Most of these crystals are efficiently served for practical applications like frequency mixers, doublers and parametric generators.

However, few of these materials also suffer with good optical quality, toxicity (due to Be in KBBF), mechanical stability (KBBF-mechanically fragile) and moderate NLO coefficients. Therefore search for new inorganic NLO materials is still in progress. Researches are able to discover various new class of inorganic NCS materials by changing the $[BO_3]^{3-}$ like anionic groups such as $[CO_3]^{3-}$ [15, 16], $[NO_3]^{3-}$ [17], $[IO_3]^-$ [18] which have similar planar triangle structure. Therefore for this thesis work few recently synthesized carbonate fluorides family crystals were chosen and tried to explore the structure-property correlation studies in many possible ways.

The organic NLO crystals [1, 12, 13] are known to exhibit high nonlinear optical efficiency with a faster optical response due to the highly de-localized electrons. On the other hand, these crystals possess a smaller laser damage threshold values and relatively lower mechanical stabilities than inorganic NLO crystals. These difficulties are slowing down the usage of these materials in real time applications. The well known organic NLO crystals are Urea ($d_{36} = 1.17$ pm/V, LDT = 1.5 GW/cm²), Methyl p-hydroxybenzoate (p-MHB) C₈H₈O₃, L-arginine acetate (LAA) (optical transparency between 220 nm and 1500 nm and LDT, SHG values are comparable with KDP), N-(3-nitrophenyl) phthalimide (N₃NP), N-(4-nitrophenyl)-N-methyl-2-aminoacetonitrile (NPAN) (crystal size: $21 \times 15 \times 15$ mm³ grown in nitromethane solvent), 4-OCH₃-4-nitrochalcone (MNC) (NLO efficiency $5 \times$ KDP), 4-Ethoxybenzaldehyde-N-methyl 4-Stilbazolium Tosylate (EBST) (NLO efficiency 11 times greater than urea), Sulphanilic acid (SAA) single crystals (LDT = 7.6 GW/cm²) etc.

In the process of organic NLO material invention, the 4-N,N-dimethylamino-4-N-methyl-stilbazolium tosylate (DAST, C₂₃H₂₆N₂O₃S) crystal is discovered by Marder et al. in 1989 [19] and till date DAST is found to be the best SHG material with extremely large NLO susceptibility $\chi_{ijk}^{(2)}(-2\omega; \omega, \omega) = 580 \pm 30$ pm/V and low dielectric constant $\epsilon = 5.2$ at 1540 nm [20]. This C-H-N-O-S based organic DAST material is made up of CO₃, HO₃, NO₃ anionic groups. It has large birefringence ($\Delta n(0) = 0.55, 0.64$) value till date and found to be one of the best NLO material used for frequency conversion, THz generation, detection and high speed optical modulators [20]. Recently, 4-N,N-dimethylamino-4-N-methyl-stilbazolium 2-

naphthalenesulfonate (DSNS, $C_{26}H_{26}N_2O_3S$) single crystals are synthesized by Blanca Ruiz et al. which show 50% higher SHG efficiency than DAST crystal [21]. The DSNS crystallize in low symmetry crystal structure (Triclinic) with less number of atoms 58 in the unit cell ($z=1$, Volume = 564.1 \AA^3) than DAST (monoclinic, with 220 atoms in Unit cell, Volume = 2098.21 \AA^3) [21]. In spite of their composition similarity, the increment in NLO efficiency of DSNS crystal with better melting temperature of $300 \text{ }^\circ\text{C}$ than DAST ($256 \text{ }^\circ\text{C}$) strongly motivated us to investigate the structure-property correlation studies of similar kind of materials (like CHNO based explosive materials) which possess similar composition, structure to help in finding a new high quality nonlinear optical material.

1.1.2 High energy materials (HEM)

A HEM can be defined as “a chemical compound or mixture capable of the rapid release of stored potential energy” [3, 4, 22–24]. It contains both fuel + oxidizer and reacts readily upon applying the external stimuli like heat, shock, impact, friction, light, electric charge or combination of these conditions. Depending upon the density and chemical composition, the release of energy and gas will vary. Based on this, energetic materials are classified into explosives, propellants and pyrotechnics categories. Based on the difference in the sensitivity to the external stimuli, explosives are further classified as low, primary and secondary explosives. The reaction velocities of low explosives: < 1130 feet per second (fps), primary explosives: > 1130 (11000 to 21000) fps and secondary explosives: > 21000 fps. The propellant's and pyrotechnics comes under low explosives class. The well known low explosives are black powder and smokeless powder. Both are used for military and civilian applications. The propellants (for example ammonium nitrate, ammonium perchlorate and potassium nitrate) are designed to release gas under controlled conditions to perform useful work. Best example for this is the deflagration of gun powder to fire a bullet out of the barrel of gun. When control is lost on propellant explosion may occur. The pyrotechnics (pyro (“fire”), tekhnikos (“made by art”)) compounds (for example: white phosphorus(WP), red phosphorus(RP)) are used to produce light, smoke, heat and sound. These materials normally found applications in crackers, illumination devices and enter-

tainment purposes. The high explosives are designed to detonate and release high energy for military ordinance applications. They can be initiated by blasting caps, high temperature, shock and friction. The primary explosives (like Lead azide, Lead Styphnate) are extremely sensitive to small external stimuli and therefore dangerous to handle. These are used in firing/explosive train to initiate powerful secondary explosives. The secondary explosives (for example: RDX, HMX, TNT, TATB etc) are very stable when compared to primary explosives as they release huge energy in detonation. It is well known that all these high energy materials/explosives are basically made up of C-H-N-O composition and are too sensitive to any kind of external stimuli. Extensive research is going on to improve the thermal, mechanical, chemical stability and toxicity of explosives by changing the chemical composition and density, to reach the nations requirements. Hence, it is always important to explore the structure-property correlations of all these class of explosives before doing further experiments and to find civilian applications. For instance, the optical response studies of these highly light sensitive materials can find applications in detecting them, signal flares and in nonlinear optical domain also.

The present scenario in this field of research is to discover the Green high energy materials (GHEM) [25] (instead of well known toxic lead azide and lead styphnate) which produce non-toxic decomposition products for military munitions, construction, mining and demolition applications. In this class of materials, lead azide is found to be one of the well known and most sensitive primary explosives which crystallizes in orthorhombic, 'Pnma' centrosymmetric space group with decomposition temperature 315 °C [26]. Recent findings in this area of research lead to the invention of two new primary explosives Potassium 1,1'-Dinitramino-5,5'-bistetrazolate (K_2DNABT , $C_2K_2N_{12}O_4$) [27] and Potassium 4,4'-Bis (dinitromethyl)-3,3'-azofurazanate (K_2BDAF , $C_6K_2N_{10}O_{10}$) [28] which are more sensitive than lead azide. These two explosives crystallize in noncentrosymmetric P-1, triclinic symmetry with $z = 1$ (formula unit) per unit-cell. This composition and structural similarity of K_2DNABT , K_2BDAF with DSNS, DAST NLO crystal strongly motivated us to choose this compounds for the present case study. Moreover, the understanding of the underlying structure-property correlations

of noncentrosymmetric explosive materials are very important for explaining the (1) observation of polymorphic crystal phase transition's (β -HMX to δ -HMX at $\sim 170^\circ\text{C}$) [29–31], hotspot formation and ignition mechanism's via second harmonic generation response. (2) for stand-off detection of energetic material trace deposited on to the surfaces and interfaces via vibrational sum frequency generation [32, 33]. In addition, the vibrational studies of explosive materials play a crucial role in explaining the THz absorption and reflection responses and are useful to improve the existing THz detector technologies to detect HEM's [33]. Most importantly, insensitive noncentrosymmetric explosive material with better SHG properties than KDP NLO crystal can be used in frequency conversion, information encoding applications too. Use of Explosive materials for NLO applications may seem to be difficult but it was proposed to be possible (for example TATB which has 4 times higher nonlinear response that of urea) [34]. The TATB has large failure diameter, it cannot be detonated in small quantities and hence it is extremely insensitive [35]. But in explosives class, secondary explosives are found to relatively more insensitive to the external stimuli (i.e. light etc) than primary explosives. For optical application purposes, apart from stability material needs to respond faster to external stimuli. Moreover, understanding the decomposition mechanism, optical response of primary explosives through experiments is risky and challenging than secondary explosives. So, the best way to understand them is through DFT simulations. Hence, the primary explosives are chosen for our basic structure-property correlation study.

1.1.3 Scope of the thesis

In Chapter 2, brief discussion about the DFT methods and their implementations for capturing various kinds of atomic interactions were given. In Chapter 3, the basic structural, electronic and optical properties of recently synthesized ABCO_3F ($\text{A}=\text{K, Rb, Cs}$; $\text{B}=\text{Ca, Sr}$) crystals [15] were presented. These crystals have large SHG coefficients 1.30, 1.30, 1.41, 0.43, 0.43 pm/V for KSrCO_3F , RbSrCO_3F , KCaCO_3F , RbCaCO_3F , CsCaCO_3F respectively. All these crystals are iso-structural and crystallize in hexagonal symmetry with space groups $\text{P}\bar{6}\text{m}2$ and $\text{P}62\text{m}$, respectively. The experimentally reported crystal structures are opti-

mized with different exchange-correlation functionals (LDA, GGA). The role of van der Waals (vdW) interactions were explored by including suitable correction methods to standard DFT functionals. The standard LDA, GGA functionals and Tran-Blaha modified Becke-Johnson potential were employed to calculate the exact band gap values and related electronic, optical properties. Overall, from this chapter we tried to find a suitable exchange-correlation functionals for exploring the various structural and electronic related properties of layered alkali-alkaline earth carbonate fluorides. These results are published in “Journal of Solid State Chemistry, Volume 212, April 2014, Pages 171-179.”

In Chapter 4, we present the basic mechanical, vibrational and thermodynamic properties of $ABCO_3F$ ($A = K, Rb, Cs$; $B = Ca, Sr$) crystals along with $CsPbCO_3F$ crystal which was synthesized in 2013. This $CsPbCO_3F$ shows highest SHG coefficients $13 \times KDP d_{36} = 0.39$ pm/V among all the carbonate crystals till date. This material also crystallizes in hexagonal space groups $P\bar{6}m2$. We have optimized the experimental crystal structures with suitable exchange-correlation functionals and tried to explain the effect of metal atoms (especially Pb atom) on bonding (through Born Effective Charge analysis), mechanical (single, polycrystalline properties), phonon's (zone centre vibrational frequencies) and thermodynamic properties. The bending modes occurring at lower frequencies when compared to other studied compounds are found to be the main reason for lower bulk modulus value of $CsPbCO_3F$ [36, 37]. The bonding properties and intensity variations of vibrational modes were analysed from Born Effective Charge (BEC) information. Overall, we noticed that Lead based carbonate fluoride compound shows very interesting optical behaviour in IR region. We found that obtained huge BEC's variations for $CsPbCO_3F$ are the main reason for it's higher optical response. These results are published in “RSC Advances, Volume 6, Oct 06, Issue 102, 2016, Pages 99885-99897.”

In Chapter 5, the effect of spin-orbit interactions on various electronic, optical properties of $CsPbCO_3F$ crystal [36] were discussed. The calculated results confirms high NLO behaviour of $CsPbCO_3F$. We explored the crucial effect of spin-orbit interactions (SOI) (especially due to Pb, Cs atoms) on various important properties for an NLO crystal like electronic band structure, linear optical

properties and birefringence (through BEC analysis), possible optical transitions. Overall, our results are good in agreement with experiments and it is obvious from the present study that, CsPbCO_3F is a direct band gap insulator, large second harmonic generation and good phase matchable NLO crystal in the UV region. These results are published in “Physical Chemistry Chemical Physics, Oct 25, 2017,19, 31255-31266.”

In Chapter 6, the structure-property correlations of two newly synthesized noncentrosymmetric green primary explosives Potassium 4,4'-Bis (dinitromethyl)-3,3'-azofurazanate (K_2BDAF) [28], Potassium 1, 1' -Dinitramino -5,5'-bistetrazolate (K_2DNABT) [27] are explored using DFT simulations. We have explained the crucial reasons behind the high sensitivity and high optical response of chosen novel explosives through the structural (effect of vdW interactions), bonding (through BEC analysis), mechanical (single and polycrystalline properties), lattice dynamical (through zone centre vibrational frequencies and full phonon dispersion curves), electronic band structure and various linear optical (complex dielectric function, absorption, refraction, birefringence) properties. All the calculated results are correlated with experimentally reported impact, friction sensitivity parameters and successfully explained the reasons behind the high sensitivity of K_2DNABT . All the calculated properties clearly suggest that K_2BDAF is found to be more stable (mechanically and dynamically), more polarizable and easily detectable than K_2DNABT . The calculated optical properties (low dielectric constant, high birefringence value) suggests that, these studied explosive materials are showing better features for NLO applications like well known organic DAST and DSTMS crystals. We explained the reasons for this kind of optical response from the studied explosive materials. We strongly believe that, by doing suitable doping to stabilize these kind of HEM's and studying the structure-property correlation of noncentrosymmetric explosives can give a new way to design the “highly efficient nonlinear SHG material” for various optical technological applications. The work presented in this chapter is a new beginning in this direction. The results will be communicated for formal publication in high impact journal. Finally in chapter 7, the conclusions of thesis results and future scope were presented.

References

- [1] V. G. Dmitriev, G.G. Gurzadyan and D.N.Nikogosyan, *Handbook of Non-linear Optical Crystals*, Springer Series in Optical Sciences 64, Springer (1999).
- [2] R. W. Boyd, *Nonlinear Optics*, Second Edition, Academic Press (2008).
- [3] J. P. Agrawal, *High Energy Materials: Propellants, Explosives and Pyrotechnics*, WILEY-VCH Verlag GmbH Co. KGaA, Weinheim (2010).
- [4] Thomas M. Klapötke, *Chemistry of High Energy Materials*, Walter de Gruyter GmbH, Berlin/Boston (2015).
- [5] G. C. Baldwin, *Introduction to Nonlinear Optics*, Plenum Press, New York (1969).
- [6] W. Nie, *Adv. Mater.*, **5**, No.7/8, 520 (1993).
- [7] R. Arun Kumar, *Hindawi Publishing Corporation J. Chem.*, **2013**, 1 (2012).
- [8] X. Jiang, L. Kang, S. Luo, P. Gong, M. H. Lee and Z. Lin, *Int. J. Mod. Phys. B*, **28**, 27, 1430018 (2014).
- [9] T. H. Maiman, *Nature*, **187**, 493 (1960).
- [10] P. A. Franken, A. E. Hill, C. W. Peters and G. Weinreich, *Phys. Rev. Lett.*, **7**, 118 (1961).
- [11] M.A.Startsev and A.Y.Elezzabi, *ISRN Optics*, **2013**, 419507 (2013).
- [12] M. Jiang and Q. Fang, *Adv. Mater.*, **11**, No.13, 1147 (1999).
- [13] U. Charoen-In, *Growth Of Organic, Inorganic and Semi-Organic Crystals by Sankaranarayanan-Ramsamy (SR) Method and Their Characterization*, PhD thesis, Suranaree University of Technology, Thailand (2010).
- [14] C. Chuangtian, *Sci. Sin.*, **22**, 22, 756 (1979).

- [15] G. Zou, N. Ye, L. Huang and X. Lin, *J. Am. Chem. Soc.*, **133**, 49, 20001 (2011).
- [16] T. Tran, J. Young, J. M. Rondinelli and P. S. Halasyamani, *J. Am. Chem. Soc.*, **139**, 139, 1285 (2017).
- [17] Y. Song, M. Luo, C. Lin and N. Ye, *Chem. Mater.*, **29**, 896 (2017).
- [18] C.-L. Hu and J.-G. Mao, *Coord. Chem. Rev.*, **288**, 288, 1 (2015).
- [19] S. Marder, J. Perry and W. Schaefer, *Sci.*, **245**, 626 (1989).
- [20] M. Jazbinsek, L. Mutter and P. Gunter, *IEEE J. Sel. Top. Quantum Electron.*, **14**, 1298 (2008).
- [21] B. Ruiz, Z. Yang, V. Gramlich, M. Jazbinsek and P. Gunter, *J. Mater. Chem.*, **16**, 2839 (2006).
- [22] J. Pichtel, *Terrorism and WMDs: awareness and response*, CRC Press (2016).
- [23] S. Appalakondaiah, *First Principles Study of Layered and Molecular solids*, PhD Thesis, University of Hyderabad, Telangana, India (2015).
- [24] N. Yedukondalu, *Computational Study of Energetic Materials under Hydrostatic Compression*, PhD Thesis, University of Hyderabad, Telangana, India (2016).
- [25] T. Brinck, *Green Energetic Materials*, John Wiley Sons, Ltd (2014).
- [26] W. Zhu and H. Xiao, *The J. Phys. Chem. B*, **110**, 18196 (2006).
- [27] D. Fischer, T. M. Klapötke and J. Stierstorfer, *Angewandte Chemie International Edition*, **53**, 8172 (2014).
- [28] Y. Tang, C. He, L. A. Mitchell, D. A. Parrish, J. M. Shreeve, *Angewandte Chemie International Edition*, **55**, 5565 (2016).
- [29] L. Smilowitz, B. F. Henson, B. W. Asay and P. M. Dickson, *J. Chem. Phys.*, **117**, 3789 (2002).

- [30] L. Smilowitz, B. F. Henson, M. Greenfield, A. Sas, B. W. Asay and P. M. Dickson, *J. Chem. Phys.*, **121**, 5550 (2004).
- [31] B. F. Henson, B. W. Asay, R. K. Sander, S. F. Son, J. M. Robinson and P. M. Dickson, *Phys. Rev. Lett.*, **82**, 1213 (1999).
- [32] H. Kim, A. Lagutchev and D. D. Dlott, *Propellants, Explosives, Pyrotechnics*, **31**, 116 (2006).
- [33] J. Yinon, *Counter-terrorist Detection Techniques of Explosives*, Elsevier, UK., 279 (2007).
- [34] S. F. Son, B. W. Asay, B. F. Henson, R. K. Sander, A. N. Ali, P. M. Zielinski, D. S. Phillips, R. B. Schwarz, and C. B. Skidmore, *J. Phys. Chem. B*, **103**, 5434 (1999).
- [35] S. F. Rice and R. L. Simpson, *The Unusual Stability of TATB: A Review of the Scientific Literature*, Lawrence Livermore National Laboratory, Livermore, CA, Report UCRL-LR-103683 (1990).
- [36] G. Zou, L. Huang, N. Ye, C. Lin, W. Cheng and H. Huang, *J. Am. Chem. Soc.*, **135**, 49, 18560 (2013).
- [37] T. T. Tran, P. S. Halasyamani, and J. M. Rondinelli, *Inorg. Chem.*, **53**, 12, 6241 (2014).

Theoretical methods

In this chapter, the theoretical methods used in calculating various properties of the studied compounds are briefly discussed. We initially present the basic implementation of density functional theory (DFT) to solve the many-body problem of solids. Further, different exchange-correlational functionals like local density approximation (LDA), and generalized gradient approximation (GGA) and semi-empirical dispersion correction methods which are used to capture the weak intermolecular interactions are presented. A short description about the implementation of spin-orbit interactions and Tran Blaha-modified Becke Johnson (TB-mBJ) potential which are used to predict reliable electronic band gaps for the chosen compounds is given. Finally, we briefed the basic methodologies used for the present work.

2.1 Solids: A many-body problem

Solid is one form of matter consisting of electrons and nuclei coupled with strong Coulomb interactions between themselves and each other. All these interactions collectively give the total energy (E) of the system called Hamiltonian (\hat{H}) which consist of the following terms [1-3]:

$$\hat{H} = - \sum_{i=1}^{N_e} \frac{\hbar^2}{2m_i} \nabla_i^2 - \sum_{I=1}^{N_n} \frac{\hbar^2}{2M_I} \nabla_I^2 + \frac{e^2}{2} \sum_{I,J=1}^{N_n} \sum_{I \neq J} \frac{Z_I Z_J}{|R_I - R_J|} + \frac{e^2}{2} \sum_{i,j=1}^{N_e} \sum_{i \neq j} \frac{1}{|r_i - r_j|} - \frac{e^2}{2} \sum_{i=1}^{N_e} \sum_{I=1}^{N_n} \frac{Z_I}{|r_i - R_I|} \quad (2.1)$$

Here Z_I / Z_J and M_I / M_J denote the nuclear charge and mass. $r = \{r_i/r_j, i/j = 1, 2, \dots, N_e\}$ represents electronic coordinates and $R = \{R_I/R_J, I/J = 1, 2, \dots, N_n\}$ represents the nuclear coordinates. In the above equation first and second terms represent kinetic energy operators of electrons (\hat{T}_e) and nuclei (\hat{T}_N) respectively. Whereas the third, fourth and fifth terms represent the electrostatic interaction between nuclei-nuclei (\hat{V}_{N-N}), electron-electron (\hat{V}_{e-e}) and nuclei-electron (\hat{V}_{N-e}). Which can be simply written as

$$\hat{H} = \hat{T}_e + \hat{T}_N + \hat{V}_{N-N} + \hat{V}_{e-e} + \hat{V}_{N-e} \quad (2.2)$$

In order to study any property of solid one needs to solve the time-independent Schrödinger equation which has the following form.

$$\hat{H}|\psi\rangle = E|\psi\rangle \quad (2.3)$$

Here E and ψ are the energy eigenvalue and eigenstate or wave function of the system. In practice, these equations are only been exactly solved for one electron (Hydrogen) systems. Whereas, with the increase of number of interactions (many-body) in the solid, numerically solving the N -electron wave function with $3N$ spatial + N spin variables become almost impossible. The best choice to solve the above inseparable Schrödinger equation is to adopt few feasible approximations. The Born-Oppenheimer (BO) approximation [4] is the first one which helps to divide a many problem in to nuclear and electronic part.

As the nuclei are more massive than the electrons, the BO approximation states that nuclei can be considered as fixed in space with respect to electrons. Therefore nuclei kinetic energy will be zero and electrons will move in a constant Coulombic potential ($\hat{V}_{N-N} + \hat{V}_{N-e} \approx V_{ext}$) induced by the nuclei. Hence one can deal with the electron states separately by solving the following simplified electronic part of total Hamiltonian.

$$\hat{H} = \hat{T}_e + \hat{V}_{e-e} + V_{ext} \quad (2.4)$$

But due to the electron-electron correlation effects, solving this Hamiltonian also

need more efforts. Further, Free electron model, Hartree and Hartree-Fock approximations are used to calculate the actual \hat{V}_{e-e} based on the electron wave function [5] and are described below.

Free electron model, Hartree and Hartree-Fock approximations:

In free electron model, the outer most electrons in an atom are assumed to interact with each other like atoms and molecules in an ideal gas. Whereas, the core electrons and nuclei are taken as stationary. The inter electron coulomb repulsion is considered rather weak than the attraction between the electrons and positive ions. This Sommerfeld assumption was able to describe the conduction of metals only which is due to the fact that, the interaction among electrons is non negligible. Further, in Hartree approximation, the electrons are assumed as non-interacting. Therefore, many electron potentials can be written as the sum of single electron potential as shown below.

$$V_H = \sum_{i=1}^N V_{r_i} \quad (2.5)$$

In terms of electron wave functions, many-body wave function $\psi(r_1, r_2, r_3, \dots, r_N)$ can be written as product of individual electron wave functions $\phi(r_1)\phi(r_2)\dots\phi(r_N)$.

$$\psi(r_1, r_2, r_3, \dots, r_N) = \phi(r_1)\phi(r_2)\phi(r_3)\dots\phi(r_N) \quad (2.6)$$

Therefore Hamiltonian can be written as,

$$\hat{H} = \hat{T}_e + V_{ext} + \hat{V}_H \quad (2.7)$$

Here V_H is known as Hartree potential. In this approach, many-body problem can be solved by using variational principle by guessing the $\phi(r_i)$. But, the main limitation of Hartree approach is that, it is unable to capture the antisymmetric nature (Pauli's exclusion principle) of electron wave function to decide the form of effective potential. Here comes the Hartree-Fock approximation, in which the anti-symmetric and Coulombic nature of electrons are taken in to account with

the single Slater determinant as shown below.

$$\psi(r_1, r_2, r_3, \dots, r_N) = \frac{1}{\sqrt{N!}} \begin{vmatrix} \phi_1(r_1) & \phi_2(r_1) & \phi_3(r_1) & \dots & \phi_N(r_1) \\ \phi_1(r_2) & \phi_2(r_2) & \phi_3(r_2) & \dots & \phi_N(r_2) \\ \cdot & \cdot & \cdot & \dots & \cdot \\ \cdot & \cdot & \cdot & \dots & \cdot \\ \phi_1(r_N) & \phi_2(r_N) & \phi_3(r_N) & \dots & \phi_N(r_N) \end{vmatrix} \quad (2.8)$$

In this determinant, the exchange of two columns or rows is equivalent to exchange of two particles. When the two rows or columns are equal, the determinant becomes zero, which means that two identical electrons/fermions cannot occupy the same state (Pauli's exclusion principle). According to Hartree-Fock approximation, the antisymmetric wave function of two electron system will be of the form

$$\psi_{HF}(r_1, r_2) = (1/\sqrt{2})[\phi_1(r_1)\phi_2(r_2) - \phi_1(r_2)\phi_2(r_1)] \quad (2.9)$$

Therefore the many-electron Hamiltonian will be

$$\hat{H} = \hat{T}_e + V_{ext} + \hat{V}_{HF} \quad (2.10)$$

Here the \hat{V}_{HF} is the corrected potential of the HF approximation over the Hartree approximation and is given by

$$\hat{V}_{HF} = \int v_x(r, r')\phi_i(r'_i)dr' = - \sum_j^N \int \frac{\phi_j(r)\phi_j^*(r')}{|r_i - r_j|} \phi_i(r'_i)dr' \quad (2.11)$$

By applying this Hamiltonian on the ψ_{HF} , one can solve for the energy of the system by minimising the total energy with respect to the coefficients of expansion in the wave function. But in this approximation, due to the use of total wave function (N-one electron system) instead of separate single-particle wave functions of the system, the other electron-electron correlations are overlooked. Later, Thomas and Fermi approximation [6, 7] gave an idea of introducing the electron charge density instead of the wave function resulting in the famous Thomas-Fermi

approach to calculate the ground state energy. The resultant expression for the kinetic energy of the system based on the uniform electron gas is as follows,

$$T[n(r)] = \frac{3}{10}(3\pi^2)^{2/3} \int n^{5/3}(r)dr \quad (2.12)$$

Here $n(r)$ define the electron density. Therefore, the total energy of the system can be written as

$$E_{TF}[n(r)] = 2.871 \int n^{5/3}(r)dr - Z \int \frac{n(r)}{r}dr + \frac{1}{2} \int \int \frac{n(r)n(r')}{|r-r'|}drdr' \quad (2.13)$$

Here the second term is nuclear-electron attractive potential and third term is the electron-electron repulsive potential. Thus Thomas-Fermi approach gives an example of how to map a density $n(r)$ on to the total energy E instead of using the wave function. By using the variational principle, total energy of the system is minimized under the constraint of $\int n(r)dr = N$ and enormously simplified the actual many-body problem. However in this approximation the exchange, correlation effects are completely ignored. Therefore, further developments of these approximations lead to the evolution of the density functional theory (DFT) which is used in the present thesis for calculating the various properties of studied compounds.

2.2 Density functional theory

After the idea of Thomas and Fermi regarding energy functional of many-body systems, the next crucial step is to find the correct electron density instead of 3N-dimensional electron wave function that takes the fundamental central role in determining the external potential. Here comes the Density Functional Theory formalism which was mainly developed based on the two important theorems given by Hohenberg-Kohn in 1964 [8]. They proved that the ground state electron density uniquely determines this external potential. This will avoid the curse of dimensionality problem for solving many-body Hamiltonian in a reasonable amount of computational time. According to this, the many-body Hamiltonian

of the system is given by,

$$\hat{H} = -\frac{1}{2} \sum_i \nabla_i^2 - \sum_i v_{ext}(r_i) + \sum_{i \neq j} \frac{1}{|r_i - r_j|} \quad (2.14)$$

$$\text{where } v_{ext}(r_i) = - \sum_I \frac{Z_I}{|r_i - R_I|}$$

Where $v_{ext}(r_i)$ is the external potential.

First Theorem:

This theorem states that there is a one-to-one unique correspondence between the external potential and 3D-electron density. Therefore the electron density uniquely determines external potential of any system. Hence, the electron density governs the wave function and determines energy from which one can calculate properties of solids.

$$n(r) \Rightarrow v_{ext}(r) \Rightarrow H \Rightarrow \psi(r), E(r) \Rightarrow \text{properties} \quad (2.15)$$

Second Theorem:

This theorem defines a universal functional for the energy in terms of the density $n(r)$ and it is valid for any $v_{ext}(r)$. This theorem states that, the exact ground state electron density $n_0(r)$ will give lowest energy than the energy that is given by any other electron density $n(r)$. i.e. The electron density that minimises the energy functional is the ground state density $n_0(r)$ only.

$$E_0 = \psi_{min} \rightarrow n_0 \langle \hat{T}_e + V_{ext} + \hat{V}_{HF} \rangle \quad (2.16)$$

i.e.

$$E[n_0] \leq E[n] \quad (2.17)$$

The Kohn-Sham Equations:

The Kohn-Sham (KS) approach [9] states that, the many-body problem of an interacting system can be replaced by a non-interacting system with the same ground state electron density $n(r)$. With KS approach, the total energy equation is given

as,

$$E_{KS} = T[n] + \int v_{ext}(r)n(r)dr + \int \frac{n(r')}{|r-r'|}dr' + E_{xc}[n] \quad (2.18)$$

This is known as KS functional. Here $T[n]$ is the independent particle kinetic energy and is given by,

$$T[n] = -\frac{1}{2} \sum_{i=1}^N \langle \psi_i | \delta | \psi_i \rangle. \quad (2.19)$$

The second term (external potential ($V_{ext}[n]$)) describes the interaction between valence electrons and nuclei. The third term is Hartree potential (V_H) describes the electron-electron Coulomb potential and fourth term is the exchange-correlation energy (E_{xc}) which cannot be evaluated accurately. In general, the one particle KS equation can be written as,

$$H_{KS}\psi_i = E_{KS}\psi_i \quad (2.20)$$

here H_{KS} is the Kohn-Sham Hamiltonian and can be written as

$$\begin{aligned} H_{KS} &= [-\frac{1}{2}\nabla^2 + v_{eff}(r)] \\ v_{eff} &= v_{ext} + \int \frac{n(r')}{|r-r'|}dr' + v_{xc}. \end{aligned} \quad (2.21)$$

$$v_{xc} = \frac{\delta E_{xc}}{\delta n} \quad (2.22)$$

Therefore, if and only if the Hartree potential and exact form of exchange-correlation potential are known, it is possible to solve the above single-particle KS-equations using the DFT based algorithms to get the exact ground state density. The steps for solving the Kohn-Sham equations are given below: 1. Guess the initial electron density, 2. Calculate the effective potential, 3. Solve the single particle Kohn-Sham equation, 4. Calculate the new density from the wave function, 5. If this new density matches with initial electron density (if the self-consistency is achieved), then the final density is used for further calculations, if-else go to step 2, by adding some part of the output density to the input density and repeat the cycle until the self-consistency is achieved.

Even though KS-equation gives the exact solution, they actually describe the non-interacting system. However, to use the KS-equations for solving the many-body interacting systems, the exchange-correlation energy part has to be taken care off. Actually, the exchange energy (E_x) part will come due to anti-symmetric nature of the particles and it can be written as

$$E_x = -\frac{1}{2} \sum_{ij} \int \int \frac{\psi_i^*(r)\psi_i(r')\psi_j^*(r')\psi_j(r)}{|r-r'|} drdr' \quad (2.23)$$

Since the motion of electrons in the solid are correlated and corresponding correlation energy (E_c) will be equal to the difference between exact non-relativistic energy and Hartree-Fock energy. To calculate this $E_{xc} = E_x + E_c$ (which describe the undefined many-body exchange and correlation functional v_{xc} in KS-equations), different approximations like local (spin) density approximation (LDA), generalized gradient approximation (GGA) are developed and few of them are used in present thesis to obtain various properties.

2.2.1 The local-density approximation (LDA)

This approximation [9] assumes that, the exchange-correlation functional is simply integral over space of a function that depends only on local density at that point. i.e. 'local' value of density is considered as a homogeneous interacting electron gas. The E_{xc} can be approximated as,

$$E_{xc}^{LDA}[n(r)] = \int n(r)\epsilon_{xc}^{hom}(n(r))d^3r. \quad (2.24)$$

Where ϵ_{xc}^{hom} is exchange-correlation energy of electron gas with density $n(r)$. Being the first and simplest approximation, LDA is used to study the properties of slowly varying electron density systems. However, it failed to describe correct cohesive energies, bulk modulus and underestimate the lattice constants in insulators and metals. The extensions of LDA to first order electron density gradients leads to the development of generalised gradient approximations.

2.2.2 The generalised gradient approximation (GGA)

In 1990s, a useful generalized gradient approximations (GGA) for E_{xc} was developed. In this approach, the E_{xc} is assumed to depend on the electron density $n(r)$ and its gradients $\delta n(r)$ and it can be written as

$$E_{xc}^{GGA}[n(r)] = \int n(r) \epsilon_{xc}[n(r), \delta n(r)] d^3 r = \int n(r) \epsilon_{xc}^{hom} F_{xc}[n(r), \delta n(r)] d^3 r. \quad (2.25)$$

This functional is classified as semi-local density functionals. Here $\delta n(r)$ represent the non-local nature of real system and F_{xc} is a functional of $n(r)$ and $\delta n(r)$. This GGA-functional improved performance and accuracy over LDA in calculating the various physical quantities like total energies, lattice parameters of solids. The most commonly used GGA parameterizations are PBE by Perdew, Burke and Enzerhof and PW91 by Perdew and Wang. But, it is well known that, the conventional density functional are inadequate to treat weak (van der Waals) interactions. In the next section, we discuss the available methods for treating these vdW interactions properly.

2.2.3 Dispersion correction methods

It is known that vdW interactions are known to play a key role in crystal stability. These forces result from the interaction of fluctuating charge distributions in one atom/molecule with the adjacent atoms. As conventional DFT methods cannot provide correct $-1/R^6$ dependence of vdW force on R , hybrid semi empirical solutions are used as C_6/R^6 form in DFT to capture the atomic pairwise dispersion effects [10]. At long range, the interatomic potential is given by C_6^{ij}/R_{ij}^6 term. Here C_6^{ij} is known as dispersion coefficient between 'i' and 'j' atom which are located at a distance R_{ij} and C_6^{ij} is material dependent. To reduce the additional dispersion contribution at short range, the C_6^{ij}/R_{ij}^6 term is matched to DFT potential with multiplication of damping function $f(R_{ij}^0, R_{ij})$ [10]. Hence the total energy can be written as:

$$E_{tot} = E_{DFT} + E_{disp} \quad (2.26)$$

$$E_{tot} = E_{DFT} + S_6 \sum_{i=1}^N \sum_{j>i}^N Nf(S_R R_{ij}^0, R_{ij}) C_6^{ij} R_{ij}^{-6} \quad (2.27)$$

Here N denotes number of atoms, S_6 is global scaling factor which depends on the type of density functional used, 'f' is damping function. Various types of damping functions, C_6^{ij} coefficient calculations methods are proposed in order to capture the dispersion energy [10]. Hence the pair-wise additive correction is found to show good improvement in the results than standard LDA, GGA functionals for the molecular and layered materials [10]. We choose to use Grimme (DFT-D2) and Ortmann, Bechstedt and Schmidt (OBS) corrections to PBE, PW91 functionals in the present thesis and a brief discussion of these two methods are given below. The Grimme (DFT-D2) [11] corrections to PBE [12] and Ortmann, Bechstedt and Schmidt (OBS) [13] correction to PW91 were employed to capture the weak interactions in the present studied materials based on the pair-wise additive correction.

In the DFT-D2 [11] method, the dispersion energy can be written as

$$E_{disp} = -S_6 \sum_{i<j} \frac{C_6^{ij}}{R_{ij}^6} f_{damp}(R_{ij}) \quad (2.28)$$

Here C_6^{ij} represents the dispersion coefficient of i^{th} and j^{th} pair of atoms and R_{ij} is the inter-atomic distance. The S_6 is global scaling factor which depends only on the type of density functional used. Here

$$C_6^{ij} = \sqrt{C_6^i C_6^j}, C_6^i = 0.05 N I_p^i \alpha^i \quad (2.29)$$

$$f_{damp} = \frac{1}{1 + e^{-d(R_{ij}/R_r - 1)}} \quad (2.30)$$

Here I_p^i is atomic ionization potential, α^i is static dipole polarizability and N is equals to 2, 10, 18, 36 and 54 for 1-5 rows of periodic table respectively. f_{damp} is a damping factor and is necessary to avoid divergence for small R_{ij} values. R_r is sum of atomic van der Waals radii [11].

According to the OBS [13] correction to PW91, the dispersion energy is given

by

$$\epsilon_{ij}^{vdw} = -f_{ij}(R) \frac{C_6^{ij}}{R^6} \quad (2.31)$$

Here damping function $f_{ij} = 1 - \exp(-\lambda x_{ij}^n)$ which is one when $R (= |R_i - R_j|)$ is large and zero for small R values. Here $x_{ij} = \frac{R}{r_{cov}^i + r_{cov}^j}$. The dispersion coefficient C_6^{ij} is given by

$$C_6^{ij} = \frac{3}{2} \alpha_i \alpha_j \frac{I_i I_j}{I_i + I_j} \quad (2.32)$$

Here α_i/α_j is the polarizability of an atom at R_i/R_j and I_i/I_j is known as ionization potential. The I_i is a characteristic energy of the atom i . Hence, the resultant dispersion energy can be written as $E_{disp} = \frac{1}{2} \sum_{ij} \epsilon_{ij}^{vdw}$.

However, when compared to experiments both the LDA/GGA functionals results in different binding energies and are known to underestimate the band gap of insulators and semiconductors by 30-50%. But for the present study, calculating the exact band gap plays a major role in predicting accurate structure-optical response of the systems. This motivated us to search for alternative new functionals (Engel-Vosko GGA, TBmBJ, GW, hybrid functionals etc) which can give accurate band gaps as like experiments over LDA and GGA. We have mainly introduced TB-mBJ functionals in our calculations within the available computational resources. This functional is very well known to predict exact band gaps close to the experimental data with less computational power than GW and hybrid functionals. Therefore we have explained the formalism of TB-mBJ in the below section.

2.2.4 Tran-Blaha modified Becke-Johnson potential (TB-mBJ)

In 2006, Becke and Johnson (BJ) [14] proposed an exact exchange optimized effective potential (OEP) to calculate the accurate band gaps. Even though BJ potential shows improvement in calculating the band gap over LDA, PBE, it still underestimates band gap. Later Fabien Tran and Peter Blaha [15] proposed a simple modification to the BJ potential with a comparable accuracy of GW and hybrid

functionals. The BJ potential can be written as,

$$v_{x,\sigma}^{BJ}(r) = v_{x,\sigma}^{Slater}(r) + \frac{1}{\pi} \sqrt{\frac{5}{6}} \sqrt{\frac{t_\sigma(r)}{\rho_\sigma(r)}} \quad (2.33)$$

where,

$$v_{x,\sigma}^{Slater} = \sum_i \frac{\rho_{i,\sigma}}{\rho_\sigma} v_{x,\sigma}^{(i)} \quad (2.34)$$

$$v_{x,\sigma}^{(i)}(r_1) = -\frac{1}{\psi_{i,\sigma}^*(r_1)\psi_{i,\sigma}(r_1)} \sum_j \int \frac{\psi_{i,\sigma}^*(r_1)\psi_{j,\sigma}^*(r_2)\psi_{j,\sigma}(r_1)\psi_{i,\sigma}(r_2)}{r_{12}} d^3 r_2 \quad (2.35)$$

$$\rho_\sigma = \sum_{i=1}^{N_\sigma} |\psi_{i,\sigma}|^2 \quad (2.36)$$

Here $v_{x,\sigma}^{Slater}$ is exchange potential energy given by Slater, ρ_σ is electron density. Later Tran and Blaha replaced the $v_{x,\sigma}^{(i)}$ potential by Becke-Roussel potential ($v_{x,\sigma}^{BR}$) which are approximately equal. The Tran Blaha modified BJ potential can be written as,

$$v_{x,\sigma}^{TB-mBJ}(r) = c v_{x,\sigma}^{BR}(r) + (3c - 2) \frac{1}{\pi} \sqrt{\frac{5}{6}} \sqrt{\frac{t_\sigma(r)}{\rho_\sigma(r)}} \quad (2.37)$$

Here,

$$v_{x,\sigma}^{BR}(r) = -\frac{1}{b_\sigma(r)} (1 - e^{-x_\sigma(r)} - \frac{1}{2} x_\sigma(r) (e^{-x_\sigma(r)})) \quad (2.38)$$

$$t_\sigma = \frac{1}{2} \sum_{i=1}^{N_\sigma} \nabla^* \psi_{i,\sigma} \cdot \nabla^* \psi_{i,\sigma}$$

Here t_σ is the kinetic energy density and $x_\sigma(r)$ can be calculated from an equation which consists of ρ_σ , $\nabla \rho_\sigma$, $\nabla^2 \rho_\sigma$ and t_σ . Then $b_\sigma(r)$ can be obtained using the relation $b_\sigma = [x_\sigma^3 e^{-x_\sigma} / (8\pi \rho_\sigma)]^{1/3}$. The value of the 'c' parameter in TB-mBJ can be calculated using

$$c = \alpha + \beta \left(\frac{1}{V_{cell}} \int_{cell} \frac{|\nabla \rho(r')|}{\rho(r')} d^3 r' \right) \quad (2.39)$$

Here V_{cell} is the unit cell volume. In practice, while minimising the relative error in calculated band gaps of few solids [16, 17], the values of free parameters in the above equation becomes $\alpha = -0.012, \beta = 1.023\text{bohr}^{1/2}$. For $c=1$, the v^{TB-mBJ} potential = v^{BJ} potential. The calculated band gaps are known to increase monotonically with increase in the c -parameter. The experimental band gaps of solids with lower band gaps can be reproduced by TB-mBJ by varying c -parameter in between (1.1-1.3). For solids with larger band gaps, C -parameter can be varied from (1.4-1.7).

Overall, in the present thesis, we have used above functionals through two different DFT methods. The structural optimisations and lattice dynamic properties are calculated with plane wave pseudopotential (PW-PP) method as implemented through Cambridge Serial Total Energy Package (CASTEP) [18]. The electronic band structure and related properties are calculated by using full potential linearized augmented plane wave (FP-LAPW) method which is implemented in WIEN2k electronic structure code [19]. These two methods are briefly discussed in the next sections (see 2.4).

2.3 Density functional perturbation theory

In 1927 Born and Oppenheimer [20] proposed adiabatic approximation method to decouple the vibrational degrees of freedom from the electronic ones within a solid. According to this method, the lattice-dynamical properties of a solid system can be obtained by solving the energy eigenvalues and eigenfunctions. The resultant Hamiltonian which depends on the nuclear coordinates(R) can be written as

$$\hat{H}_{BO}(R) = \hat{T}_e + \hat{V}_{ee} + \hat{V}_{en} + \hat{V}_{nn} \quad (2.40)$$

The first term in above equation, \hat{T}_e represents kinetic energy of nucleus, remaining terms $\hat{V}_{ee}, \hat{V}_{en}, \hat{V}_{nn}$ represent electron-electron, electron-nuclei, nuclei-nuclei electrostatic interactions. The equilibrium geometry of the solid can be obtained by equating the interatomic forces (first derivative of Born-Oppenheimer

energy surface) to zero.

$$F_I \equiv -\frac{\partial E(R)}{\partial R_I} = 0 \quad (2.41)$$

The vibrational frequencies ω with respect to (w.r.to) the nuclear masses (say M_I , M_J), can be obtained by equating the second derivative of Born-Oppenheimer energy surface to zero

$$\det \left| \frac{1}{\sqrt{M_I M_J}} \frac{\partial^2 E(R)}{\partial R_I \partial R_J} - \omega^2 \right| = 0 \quad (2.42)$$

The basic tool used to solve this first, second derivatives of Born-Oppenheimer energy surface is the Hellmann-Feynman theorem. According to this, the first derivative of energy eigenvalue of Hamiltonian which depends on a parameter (say λ) can be written as,

$$\frac{\partial E_\lambda}{\partial \lambda} = \langle \psi_\lambda | \frac{\partial H_\lambda}{\partial \lambda} | \psi_\lambda \rangle \quad (2.43)$$

Here ψ_λ is the eigenfunction, E_λ is the eigenvalue. Similarly, in BO approximation, the nuclear coordinates acts as parameters. Therefore the resultant equation for force acting on I^{th} nucleus can be written as

$$F_I \equiv -\frac{\partial E(R)}{\partial R_I} = -\langle \psi(R) | \frac{\partial H_B O(R)}{\partial R_I} | \psi(R) \rangle \quad (2.44)$$

$$F_I \equiv -\int n_R(r) \frac{\partial V_R(r)}{\partial R_I} - \frac{\partial E_N(R)}{\partial R_I} \quad (2.45)$$

Here $n_R(r)$ is electron ground-state charge density, $V_R(r)$ is electron-nucleus interaction potential, $E_N(R)$ electrostatic interaction between different nuclei. The Hessian of Born-Oppenheimer (BO) energy surface now can be obtained by differentiating the Hellmann-Feynman forces w.r.to R as follows:

$$\frac{\partial^2 E(R)}{\partial R_I \partial R_J} = \int \frac{\partial n_R(r)}{\partial R_J} \frac{\partial V_{en}(R)}{\partial R_I} dr + \int n_R(r) \frac{\partial^2 V_{en}(R)}{\partial R_I \partial R_J} dr + \frac{\partial^2 V_{m}(R)}{\partial R_I \partial R_J} \quad (2.46)$$

The $n_R(r)$ and $\frac{\partial n_R(r)}{\partial R_I}$ (linear response of electron density) are the prerequisites to solve the Hessian matrix which usually called the inter-atomic force constants (IFC) matrix [21]. The Fourier transform of IFC will give us the required dynamical matrix in the reciprocal space. The vibrational frequencies obtained with this DFPT method are known to show good in agreement with the experiments with a few percents of error. In order to analyse the polarization mechanism in the studied material, we have used born effective charge analysis method. According to Huang's phenomena [21], in the long wavelength/low energy regions, long range Coulomb forces will give macroscopic electric fields for longitudinal optic phonon's. The general expression of energy as a function of phonon optic coordinates and the field can be written as,

$$E(u, E) = \frac{1}{2} M \omega_0^2 u^2 - \frac{\Omega}{8\pi} \epsilon_\infty E^2 - e Z^* u \cdot E \quad (2.47)$$

Here M is reduced mass, Ω is unit cell volume, ϵ_∞ is the static dielectric constant with fixed nuclei ($u=0$) position. Z^* is the Born effective charge of ions (coupling between u and E). The corresponding macroscopic electric polarization can be written as,

$$P = \frac{1}{\Omega} \sum_s e Z_s^* u_s + \frac{\epsilon_\infty - 1}{4\pi} E \quad (2.48)$$

Hence, the Born effective charge (Z^*) tensor of s^{th} ion can be defined as partial derivative of macroscopic polarization (P) w.r.to periodic displacement of all 's' ion at zero electric field. i.e.

$$eZ_s^{*\alpha\beta} = \Omega \frac{\partial P_\alpha}{\partial u_s^\beta} \Big|_{E=0} \quad (2.49)$$

The dielectric-constant tensor can be written as derivative of polarization (P) with respect to E at clamped nuclei.

$$\epsilon_\infty^{\alpha\beta} = \delta_{\alpha\beta} + 4\pi \frac{\partial P_\alpha}{\partial E_\beta} \Big|_{u_s(q=0)=0} \quad (2.50)$$

Hence, within the harmonic limit, DFPT is very well known technique used in the literature to calculate phonon frequencies, Born effective charges and dielectric properties. The results are known to match with experimental data within a few percents of error [22].

2.3.1 General spectroscopic properties

The external perturbation to electrostatic potential of a test charge can be written in terms of inverse dielectric matrix [21, 23] as follows:

$$\Delta V_{test}(r) = \int \epsilon^{-1}(r, r') \Delta V(r') dr' \quad (2.51)$$

The linear response of charge density to external perturbation can be written as

$$\Delta n(r) = \int \chi(r, r') \Delta V(r') dr' \quad (2.52)$$

Here $\chi(r, r')$ is electron polarizability. The above two response functions can be written as

$$\epsilon^{-1}(r, r') = \delta(r - r') - \int \frac{e^2}{|r - r_1|} \chi(r_1, r) dr_1 \quad (2.53)$$

The charge density response in terms of Kohn-Sham potential can be written as

$$\Delta n(r) = \int \chi_0(r, r') \Delta V_{eff}(r') dr' \quad (2.54)$$

Here $V_{eff} = V_{ext} + V_H + V_{xc}$. $\chi_0(r, r')$ is independent electron polarizability and it can be written in terms of Kohn-Sham orbitals as

$$\chi_0(r, r') = \sum_{n,m} \frac{f_n - f_m}{\epsilon_n - \epsilon_m} \psi_n^*(r) \psi_m(r) \psi_m^*(r') \psi_n(r') \quad (2.55)$$

Here f_n is known as occupancy of the state. $f_n = \theta[(\epsilon_F - \epsilon_n)/\sigma]$.

Therefore the perturbed Kohn-Sham potential and resultant response function (electron polarization) can be written as

$$\Delta V_{scf}(r) = \Delta V(r) + \int K(r, r') \Delta n(r') dr' \quad (2.56)$$

$$\begin{aligned} \chi(r, r') &= \chi_0(r, r') + \int \chi_0(r, r_1) K(r_1, r_2) \chi(r_2, r') dr_1 dr_2 \\ K(r_1, r_2) &= \left[\frac{1}{r_1 - r_2} + f_{xc}(r_1, r_2) \right] \end{aligned} \quad (2.57)$$

Here exchange-correlation kernel $f_{xc} = \frac{\delta V_{xc}(1)}{\delta n(2)} |n_{GS}$. It can be solved by using time dependent density functional theory approximations. The simplest way to solve for the microscopic electron polarization is to fix $f_{xc} = 0$ which is known as random phase approximation. The relation between the calculated microscopic

and experimentally measurable macroscopic dielectric function is given by

$$D(r, t) = \int dr' dt' \epsilon_M(r, r', t - t') E(r', t') \quad (2.58)$$

Here ‘D’ and ‘E’ are electric displacement and total electric field. As we deal with periodic systems in this thesis, the total macroscopic response function follows periodicity of external perturbation, but in microscopic scale the response function shows rapid oscillations with primitive cell. Therefore it is important to know this microscopic and macroscopic connection of response function. The relation between microscopic $\epsilon_{GG'=0}^{-1}(q, \omega)$ and macroscopic dielectric function ϵ_M is given by

$$\epsilon^M(q, \omega) = \frac{1}{\epsilon_{GG'=0}^{-1}(q, \omega)} \quad (2.59)$$

Here

$$\epsilon^{-1} = \frac{\delta(V_{ext} + V_{Hartree})}{\delta(V_{ext})} = 1 + v\chi \quad (2.60)$$

Here χ is the response function, G is the reciprocal lattice vector. By using this macroscopic dielectric function $\epsilon = \epsilon_1 + i\epsilon_2$ one can extract the other spectroscopic properties like absorption coefficient ($\alpha = \frac{\omega\epsilon_2}{nc}$), refractive index ($n = \sqrt{\epsilon} = n + ik$) etc. Here the imaginary part of dielectric function ϵ_2 can be calculated by using Kramers-Kronig (KK) relations. According to KK relations, the real and imaginary parts of a given complex function ($\chi = \chi_1(\omega) + i\chi_2(\omega)$) are related as follows:

$$\chi_1(\omega) = \frac{1}{\pi} P \int_{-\infty}^{\infty} \frac{\chi_2(\omega')}{\omega' - \omega} d\omega' \quad (2.61)$$

and

$$\chi_2(\omega) = -\frac{1}{\pi} P \int_{-\infty}^{\infty} \frac{\chi_1(\omega')}{\omega' - \omega} d\omega' \quad (2.62)$$

Here $\chi_1(\omega)$, $\chi_2(\omega)$ are the real and imaginary parts of complex function which are not independent and ‘P’ is Cauchy principal value.

Overall, using above described DFT methodology, we have calculated all the

ground state properties of chosen materials. As we know the importance of excited state properties of the studied optical materials [25], we would like to treat these effects by using advanced time dependent density functional theory in near future. We briefly explained the basic methodologies followed for this thesis in the next section.

2.4 Methodology

As the plane waves (PW) are very inefficient to describe the one electron wave functions near the nuclei, one needs to adopt pseudopotential methods or augmented PW basis set [26]. We briefly discuss about these methods one by one in the below section. Before explaining the LAPW method, we discuss about the Augmented Plane Wave (APW) method proposed by Slater.

2.4.1 Pseudopotential method

The rapidly varying valence wave functions will have nodes in them near the nucleus and to treat them using plane waves is much more expensive. For heavier elements it is going to be harder and harder to represent them. Moreover, it is known that, inner core electrons of nucleus don't take part in bonding and most of the other physical, chemical properties mainly occur due to the valence electrons. Therefore to solve the many-body Schrödinger equation, all-electron potential is approximated as pseudopotential by eliminating the core-electrons contribution set [26].

$$\left(\frac{1}{2}\nabla^2 + V\right)\psi = \varepsilon\psi \quad (2.63)$$

Where ψ is the all electron wave function with angular momentum l .

Hence the effective potential gives node-less wave function which will match with actual wave function of the system at large distance from nucleus and disagrees below cut-off. This pseudo wave function can be written in terms of j_l (spherical Bessel functions)

$$\psi_l^{ps} = \sum_{i=1}^n \alpha_i j_l^i \quad (2.64)$$

Here α_i is the fitting parameter. In the present thesis, we have used these pseudopotential methods for optimizing the experimental crystal structures and to evaluate mechanical (single, poly- crystal elastic constants), dynamical properties (zone centre vibrational spectra, complete phonon dispersion curves in the Brillouin zone) as implemented in CASTEP [18]. As there is a very strong influence of valence electron interactions on the bonding, electronic and optical properties, we used full potential-LAPW methods as implemented in WIEN2K [19] for further study.

2.4.2 Augmented Plane Wave (APW) method

Even though Pseudopotential methods are used to study various properties of a given system, some alternative basis sets are developed to consider core and semi-core electronic contribution. The Augmented Plane Wave (APW) Method is known to be the first one to discuss and this method is almost similar to PP method [26–28]. According to this, the (free)electrons far from the nucleus are treated with plane wave functions. Whereas the behaviour of electrons near nucleus (which behaves like electrons in free atom) are described by atomic like wave function. Therefore the space is divided into two parts as: (1). Muffin-tin (MT) region: The space occupied by the atom sphere of radius R_α ; (2). Interstitial (I) region: The space outside the muffin-tin sphere. The corresponding potential and the augmented plane wave can be written as,

$$V(r) = \begin{cases} \sum_{lm} V_{lm}(r) Y_{lm}(r) & (r \in MT) \\ \sum_G V_G e^{iG \cdot r} & (r \in I) \end{cases} \quad (2.65)$$

$$\phi_{k_n}^{APW}(r, \epsilon_l) = \begin{cases} \sum_{lm} A_{lm, k_n} u_l(r, \epsilon_l) Y_{lm}(r) & (r \in MT) \\ \frac{1}{\sqrt{V}} e^{i k_n \cdot r} & (r \in I) \end{cases} \quad (2.66)$$

Here V is unit cell volume, $G_n, k_n = k + G_n$ are reciprocal lattice vectors and

k is wave vector. The A_{lm} coefficients can be calculated by matching the atomic like wave functions and plane wave functions at a given l_{max} . The $Y_{lm}(r)$, $u_l(r, \epsilon_l)$ are spherical harmonics and the solutions of radial part of Schrödinger equation of an atom. Therefore the resultant wave function (ψ) used to solve Kohn-Sham equation is as follows:

$$\psi_k(r) = \sum_n c_n \phi_{k_n}(r) \quad (2.67)$$

Here, $\phi_{k_n}(r)$ is basis function, c_n is coefficient. For a free atom α , the $u_l(r, \epsilon_l)$ will vanish as $r (R_\alpha) \rightarrow \infty$, but in practice this condition doesn't apply, hence one needs to solve for ϵ_l numerically. It is known that, for a given l_{max} value there will be $l_{max}/(\pi R_\alpha)$ nodes per unit length for $Y_{lm}(r)$. The plane wave of time period $(2\pi/K_{max})$ will have $(2/(2\pi/K_{max})) = K_{max}/\pi$ nodes per unit length. Therefore in order to get proper match of atomic wave function (l_{max}) and plane wave function (K_{max}) with equal number of nodes the following condition should be satisfied: $R_\alpha \times K_{max} = l_{max}$. This equation allows us to choose proper muffin-tin radius, K_{max} , l_{max} combination. The muffin-tin radius if all atoms of given system should not vary too much, since it may leads to difficulty in choosing the suitable l_{max} value. However, the eigenvalues ' ϵ_l ' in 2.33 can be obtained by a self-consistent diagonalization method. Which leads to APW method slower than pseudopotential method.

2.4.3 Linearized Augmented Plane Wave (LAPW) method

Unlike in APW method, in this present method the $u_l(r, \epsilon_l)$ is attempted to calculate at a given energy using Taylor expansion [26] which will be of the form

$$u_l(r, \epsilon_l) = u_l(r, \epsilon_l^1) + (\epsilon_l - \epsilon_l^1) \dot{u}_l(r, \epsilon_l^1) + O((\epsilon_l - \epsilon_l^1)^2) \quad (2.68)$$

Here $\dot{u}_l = \partial u_l / \partial \epsilon_l$.

By adding first two terms in the above equation, the APW basis set will give LAPW basis set [26] as follows:

$$\phi_{k_n}^{LAPW}(r) = \begin{cases} \sum_{lm} [A_{lm,k_n} u_l(r, \epsilon_l) + B_{lm,k_n} \dot{u}_l(r, \epsilon_l)] Y_{lm}(r) & (r \in MT) \\ \frac{1}{\sqrt{V}} e^{ik_n \cdot r} & (r \in I) \end{cases} \quad (2.69)$$

Since $(\epsilon_l - \epsilon_l^1)$ is unknown, one more constant B_{lm,k_n} will be added for defining the atomic like wave function. These both constants can be obtained by matching the value and slope of wave functions at the sphere boundary. There is no difference in APW and LAPW basis sets for defining the plane waves in the interstitial region. This change in basis set leads to reduce the computational time, but it is comparable with the plane wave basis set. Till now, the core and valence states are treated with LAPW. In order to treat the states lying in between core and valence states i.e. semi-core states in 1991 David Singh [24] proposed a concept of local orbitals (LO). The corresponding basis set is given as:

$$\phi_{k_n}^{LAPW}(r) = \begin{cases} \sum_{lm} [A_{lm,LO} u_l(r, \epsilon_{1,l}) + B_{lm,LO} \dot{u}_l(r, \epsilon_{1,l}) + C_{lm,LO} u_l(r, \epsilon_{2,l})] Y_{lm}(r) & (r \in MT) \\ 0 & (r \notin MT) \end{cases} \quad (2.70)$$

A 'LO' is defined for a particular atom, for particular l and m values. It is zero in the muffin-tin spheres of other atoms and in the interstitial regions. Hence orbital is local and is not connected to the interstitial plane waves. The $A_{lm,LO}$, $B_{lm,LO}$, $C_{lm,LO}$ coefficients can be determined with a condition that LO is normalized and it should have zero value and slope at sphere boundary. Hence with this increased basis set valence and semi-core electrons (all electrons) can be treated properly to increase the accuracy. This LAPW+LO method is computationally bit slower than LAPW method.

2.4.4 APW+lo method

The nonlinear energy dependence eigenvalue problem of APW method and larger basis set problem of LAPW+LO method is combinedly removed by this APW+lo method [26]. This method uses two basis functions namely initial APW's with a fixed energy and another is local orbitals (lo's) type and can be represented as

follows:

$$\phi_{lm}^{APW+lo}(r) = \begin{cases} [A_{lm}u_l(r,\epsilon_l) + B_{lm}\dot{u}_l(r,\epsilon_l)]Y_{lm}(r) & (r \in MT) \\ 0 & (r \in I) \end{cases} \quad (2.71)$$

The A_{lm} , B_{lm} coefficients can be determined by normalization with a condition that local orbitals will have zero value at the sphere boundary but not the zero slope. Therefore APW and lo's are continuous at the boundary with \dot{u}_l is discontinuous. Hence APW + lo method with a small basis set like APW gives accurate results as that of the LAPW method via single disorganisation. The problem of semi-core states can be addressed by using another method called APW + lo + LO and corresponding basis set can be written as,

$$\phi_{LO}^{APW+lo}(r) = \begin{cases} [A_{lm,LO}u_l(r,\epsilon_{1,l}) + C_{lm,LO}u_l(r,\epsilon_{2,l})]Y_{lm}(r) & (r \in MT) \\ 0 & (r \notin MT) \end{cases} \quad (2.72)$$

There is no \dot{u}_l term here and $A_{lm,LO}$, $C_{lm,LO}$ coefficients can be determined by the requirement of LO is normalized and has no value (not zero slope) at the muffin-tin boundary. In case of heavier atoms, spin-orbit interaction plays a major role in determining the accurate energy eigenvalues. All the above mentioned APW methods are scalar relativistic methods and omit spin-orbit coupling effects. Later in 1980 A.H. MacDonald [29] proposed a second variational treatment to include spin-orbit interactions into the basis set and it can be given by:

$$\phi^{lms}(r) = (1/r) \begin{bmatrix} [\dot{P}_l Y_{lm} \chi_s] \\ [i(\sigma.r)[-Q_l + (1/2Mc\sigma)P_l \sigma.L] Y_{lm} \chi_s] \end{bmatrix} \quad (2.73)$$

Here

$$P_l^{kns}(r) = \begin{cases} \sum_{lm} [A_{lm,kn} \phi_{lms}(r) + B_{lm,kn} \dot{\phi}_{lms}(r)] & (r \in MT) \\ 0 & (r \notin MT) \end{cases} \quad (2.74)$$

The A_{lm} , B_{lm} are determined with condition that the large component and its spatial derivative will be continuous across the sphere boundary. For including the semi-core states of heavier elements suitable basis set is needed. All the basic

APW methods have only one p-type radial function which has similar behaviour as $p_{3/2}$ orbital. Whereas with this second variational treatment it is possible to obtain $p_{1/2}$ orbital which has different nodal structure [26]. In the present thesis for CsPbCO₃F crystal, we have used this method to capture the effect of spin-orbit interactions on various electronic and optical properties [30].

References

- [1] J. Kohanoff, *Electronic structure calculations for solids and molecules: Theory and Computational Methods*, Cambridge University Press, Cambridge (2006).
- [2] W. Koch and M.C. Holthausen, *A Chemist's Guide to Density Functional Theory*, Wiley Vch, New York (2002).
- [3] R.G. Parr and W. Yang, *Density Functional Theory fo Atoms and Molecules*, Oxford University Press, Oxford (1989).
- [4] M. Born and J. R. Oppenheimer, *Am. J. Phys.*, **84**, 451 (1927).
- [5] J. M.Wills, O.Eriksson, P.Andersson, A.Delin, O.Grechnyev and M.Alouani, *Full-Potential Electronic Structure Method*, Springer Series in Solid-State Sciences 167, Springer-Verlag Berlin Heidelberg (2010).
- [6] L. H. Thomas, *Proc. Cambridge Phil. Soc*, **23**, 542 (1927).
- [7] E. Fermi, *Z. Phys.*, **48**, 73 (1928).
- [8] P. Hohenberg and W. Kohn, *Phys. Rev.*, **136**, B864 (1964).
- [9] W. Kohn and L. Sham, *Phys. Rev.*, **140**, A1133 (1965).
- [10] S. Appalakondaiah, *Firrst pricniples study of layered and molecular solids*, Doctoral thesis, University of Hyderabad (2015).
- [11] S. Grimme, *J. Compu. Chem.*, **27**, 1787 (2006).
- [12] J. P. Perdew, M. Ernzerhof and K. Burke, *J. Chem. Phys.*, **105**, 9982 (1999).
- [13] F. Ortman, F. Bechstedt and W. G. Schmidt, *Phys. Rev. B*, **73**, 205101 (2006).
- [14] A. D. Becke and E. R. Johnson, *J. Chem. Phys.*, **124**, 221101 (2006).
- [15] F. Tran and P. Blaha, *Phys. Rev. Lett.*, **102**, 226401 (2009).

- [16] D. Koller, F. Tran and P. Blaha, Phys. Rev. B, **85**, 155109 (2012).
- [17] D. Koller, F. Tran and P. Blaha, Phys. Rev. B, **83**, 195134 (2011).
- [18] S. J. Clark, M. D. Segall, C. J. Pickard, P. J. Hasnip, M. J. Probert, K. Refson and M. C. Payne, Zeitschrift fuer Kristallographie, **220 (5-6)**, 567 (2005).
- [19] P. Blaha, K. Schwarz, G. K. H. Madsen, D. Kvasnicka and J. Luitz, *WIEN2k, An Augmented Plane Wave + Local Orbitals Program for Calculating Crystal Properties*, Karlheinz Schwarz, Techn. Universit at Wien, Austria (2001).
- [20] M. Born and J. R. Oppenheimer, Am. J. Phys., **84**, 451 (1927).
- [21] S. Baroni, S. D. Gironcoli. A. D. Corso and P. Giannozzi, Rev. Mod. Phys., **73**, 515 (2001).
- [22] M. J. Verstraete and Z. Zanolli, *Lecture Notes of the 45th IFF Spring School Computing Solids- Models, ab initio methods and supercomputing*, Forschungszentrum Jülich (2014).
- [23] B. Wang, *Electronic structure and optical properties of solar energy materials*, Ph.D thesis, KTH, Sweden (2014).
- [24] D. Singh, Phys. Rev. B, **43**, 6388 (1991).
- [25] L. Kronik and J. B. Neaton, Ann. Rev. Phys. Chem., **67**, 587 (2016).
- [26] S. Cottenier, *Density Functional Theory and the family of (L)APW-methods: a step-by-step introduction*, Instituut voor Kern-en Stralingsfysica, K.U.Leuven, Belgium (2002).
- [27] K. Schwarz, P. Blaha and G.K.H. Madsen, Comput. Phys. Commun, **147**, 71 (2002).
- [28] M. Petersen, F. Wanger, L. Hufnagel, M. Scheffler, P. Blaha and K. Schwarz, Comput. Phys. Commun, **126**, 294 (2000).
- [29] A. H. MacDonald, W. E. Pickett and D. D. Koelling, J. Phys. C: Solid St. Phys., **13**, 2675 (1980).

- [30] E. Narsimha Rao, G. Vaitheeswaran, Ali H. Reshak and S. Auluck, *Phys. Chem. Chem. Phys.*, **19**, 31255 (2017).

ABCO₃F (A = K, Rb, Cs; B = Ca, Sr)

In the present study, first-principles calculations were performed to explore electronic structure and optical properties of layered alkali-alkaline earth carbonate fluorides which attract attention in the domain of nonlinear optics. The calculated lattice parameters and volumes with and without inclusion of van der Waals (vdW) correction methods to standard density functional methods were compared with experiments. It is observed that vdW interactions are predominant in RbCaCO₃F and CsCaCO₃F as compared with other computed compounds. The calculated bulk modulus from single crystal elastic constants reveals that these materials are all relatively harder than KH₂PO₄ (KDP) crystal. It is also found that these materials are wide band gap insulators as obtained from Tran-Blaha modified Becke-Johnson potential. The linear optical properties such as dielectric function, refractive indices, birefringence and absorption spectra are presented. Finally, the calculated birefringence values indicate that these crystals could be promising for producing phase matching in the deep ultraviolet region.

3.1 Introduction

Over the past decades, exploring knowledge of nonlinear optical (NLO) materials has become an attractive area of research due to their technological and industrial usage for generating shorter pulses with available lasers [1–13]. The anionic

group, which contains planar triangular structure and conjugated π -orbitals are believed to be the source of large SHG coefficients. As mentioned in the introduction chapter, the borate NLO crystals are mainly made up of four anionic groups such as $[\text{BO}_3]^{3-}$, $[\text{BO}_4]^{5-}$, $[\text{B}_3\text{O}_6]^{3-}$, and $[\text{B}_4\text{O}_9]^{6-}$. Among these borate anionic groups, $[\text{BO}_3]^{3-}$ possesses planar structure with large microscopic second order susceptibility and a moderate birefringence, and is found to be the most suitable structural unit of borate crystals for UV and deep-UV light generation. These crystals are used for many practical applications since past few decades. In addition to borate crystals, nitrates ($[\text{NO}_3]^-$) and carbonates ($[\text{CO}_3]^{2-}$) are found to have similar planar triangular structure. Therefore it is believed that, they can also exhibit larger nonlinear optical responses. But, nitrates can dissolve easily in water which prevents their use in industrial applications and the carbonates are stable in air but difficult to grow as single crystals.

The fluorocarbonates are known to occur in alkaline rock complexes, natural minerals [2] and very few studies are available in the literature for these compounds. For the past few decades numerous attempts were made to synthesize these carbonate based crystals at laboratory scales [2]. Initially in this group of crystals, the $\text{A}_2\text{A}'\text{CO}_3\text{F}$ ($\text{A}, \text{A}' = \text{K}, \text{Rb}, \text{Cs}$) fluorocarbonate series was reported by Albert et al [14, 15], KCaCO_3F [16, 35] phase was discovered by West Fletcher in 1992, lead carbonate fluoride single crystal $\text{Pb}_2\text{F}_2\text{CO}_3$ was reported by Bengt Aurivillius in 1983 [18]. These crystals are known as the starting carbonate materials in this field. Recent experimental and theoretical attempts in this direction have yielded many new novel carbonate fluoride crystals with good chemical, mechanical stability and strong nonlinear optical responses up to 530 [19] times higher than $\alpha\text{-SiO}_2$ which is the highest among all the carbonate fluoride crystals known till date. The fluoride-oxygen based compounds are found to be useful as a matrix for bi-doped rare earth compounds also [20].

Recently, Zou et al [36] synthesized a series of alkali-alkaline earth carbonate fluoride crystals ABCO_3F ($\text{A} = \text{K}, \text{Rb}, \text{Cs}$; $\text{B} = \text{Ca}, \text{Sr}$), which possess low wave-

length absorption edges (less than 200 nm) and larger SHG coefficients than well known KH_2PO_4 (KDP) crystal. In these class of materials, the $[\text{CO}_3]$ groups are co-parallel, which leads to a large macroscopic SHG coefficients 1.30, 1.30, 1.41 pm/V for KSrCO_3F , RbSrCO_3F , KCaCO_3F . Whereas two thirds of $[\text{CO}_3]$ groups are parallel and one third are anti parallel, resulting in the lesser SHG coefficients 0.43, 0.43 pm/V for RbCaCO_3F , CsCaCO_3F , respectively. [36] Among these materials KSrCO_3F , RbSrCO_3F , KCaCO_3F (with $Z=1$) and RbCaCO_3F , CsCaCO_3F (with $Z=3$) are iso-structural and crystallize in hexagonal crystal symmetry with space groups $\text{P}\bar{6}\text{m}2$ and $\text{P}\bar{6}2\text{m}$, respectively. All these structures exhibit the stacking of $[\text{AF}]_\infty$ ($A = \text{K, Rb, Cs}$) and $[\text{B}(\text{CO}_3)]_\infty$ ($B = \text{Ca, Sr}$) layers along c-axis and the co-planar alignment of $[\text{CO}_3]$ triangles perpendicular to c-axis. The triangular planar structure of $[\text{CO}_3]^{2-}$ is responsible for the larger SHG coefficients. Very recently Kang et al [37] proposed two novel NLO materials such as KBeCO_3F and $\text{RbAlCO}_3\text{F}_2$ for deep-UV region applications by using the first-principles calculations. Therefore it is interesting to study the fundamental structure-property correlation of this newly synthesized alkali-alkaline earth carbonate fluoride NLO crystals. Hence, in this study initial density functional theory calculations are performed on this carbonate series NLO crystals.

3.2 Calculation methods

The first-principles calculations were performed using two different Density Functional Theory (DFT) approaches; the structural and elastic properties are calculated by using the plane wave pseudopotential (PW-PP) method which is implemented through CASTEP code.[38, 39] The exchange-correlation potential is described in both generalized gradient approximation (GGA) with Perdew-Burke-Ernzerhof (PBE) [40], Perdew and Wang (PW91)[41] parameterization and local density approximation (LDA) with Ceperley and Alder [42] parameterized by Perdew and Zunger (CA-PZ) [43, 44]. The electron-ion interactions were de-

scribed by using Vanderbilt type ultra-soft pseudopotential [45]. All the studied compounds have alternate MF (M = K, Rb, Cs) and MCO₃ (M = Ca, Sr) layers stacked along c-axis [36] and the layers are bonded through weak van der Waals (vdW) forces. Therefore, semi empirical dispersion correction methods have been used to treat vdW interactions, the Ortman, Bechstedt and Schmidt [46] (OBS) correction to PW91, as well as Grimme [47] corrections to PBE. In these two methods, a correction of the form $E_{ij} = f(R) \times C_6^{ij} \times R_{ij}^{-6}$ is added to the DFT total energy for each pair (ij) of atoms separated by a distance R_{ij} . $f(R)$ is a damping function, which is necessary to avoid divergence for small values of R , and C_6^{ij} is the dispersion coefficient for the atom pair (ij) and the C_6^{ij} coefficients are dependent only on the chemical species. The kinetic energy cut-off of 640 eV was used and the first Brillouin zone of the unit cell sampled by using Monkhorst-Pack scheme [48] of k-points with a spacing of about 0.04\AA^{-1} . The convergence criteria for optimization of unit cell has been done by relaxing the forces ($< 5 \times 10^{-4}$ eV/Å), energies ($< 5 \times 10^{-6}$ eV), and stress tensors (< 0.02 GPa) on each atom.

The electronic structure and optical properties are calculated by using full potential linearized augmented plane wave (FP-LAPW) method which is implemented in WIEN2k [49]. In general, the standard DFT functionals such as LDA and GGA usually underestimate the energy-band gap by 30-40% when compared to experiments due to the lack of the derivative discontinuities of the exchange-correlation potential with respect to occupation number. In order to get reliable energy band gaps, one has to use more sophisticated methods such as hybrid functionals (HSE, PBE0), GW approximation, EV-GGA and TB-mBJ potentials [51]. It is well known that hybrid and GW calculations are computationally very expensive, the later methods are computationally cheap to reproduce band gaps. The EV-GGA functional obtained by optimization of the exchange-correlation potential V_{ex} instead of the energy E_{ex} . TB-mBJ is also a newly developed semi-local potential, which uses information from kinetic energy density along with the charge density employed in standard DFT functionals. The EV-GGA and

TB-mBJ functionals cannot be used for total energy calculations but instead yields very much improved band gaps in a wide variety of materials and TB-mBJ potential is good enough in reproducing accurate energy band gaps when compared to EV-GGA, which are comparable with experiments. In order to achieve energy eigenvalue convergence, the wave functions in the interstitial region were expanded using plane waves with a cut-off of $K_{max} = 8/R$ MT, self-consistency was obtained using 39 k-points in the irreducible Brillouin zone (IBZ). The frequency dependent optical properties were calculated using dense k-points (320) in IBZ.

3.3 Results and discussion

3.3.1 Structural and elastic properties

Initially, ground state properties of these compounds were obtained with both LDA as well as GGA by using PW-PP method. The experimental crystal structure [36] (see Fig 3.1) is used as an input for each calculation and minimized the total energies, forces and stresses on each atom of the unit cell. The obtained volumes are underestimated by about 7% with LDA whereas overestimated by 4% within GGA. The GGA functional reproduce the experimental values over LDA. Moreover, the crystal structures consist of alternately stacked layers $[AF]_{\infty}$ ($A = K, Rb, Cs$) and $[B(CO_3)]_{\infty}$ ($B = Ca, Sr$) and all the adjacent layers are connected by infinite B-F-B chains parallel to c-axis. Since the layers are weakly bonded through the van der Waals forces, which cannot be treated well with standard LDA/GGA functionals, the dispersion corrected methods such as G06 and OBS implemented through GGA functional are used. The calculated ground state properties with G06 and OBS methods are in very good agreement with experimental results [36] and the volumes differ only by about 1%. This effect is mainly observed in heavy metal carbonates such as $RbCaCO_3F$ and $CsCaCO_3F$ than rest of the studied carbonates and GGA functional is good enough to reproduce the ground state

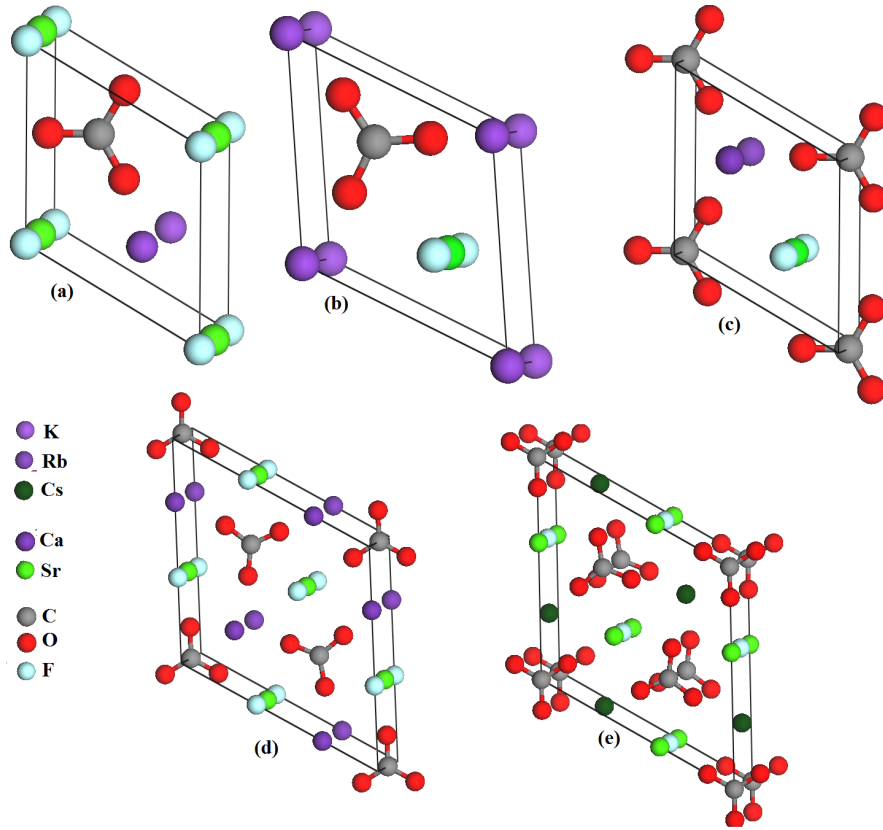


Figure 3.1: Experimental crystal structure of a) KCaCO_3F , b) KSrCO_3F , c) RbSrCO_3F , d) RbCaCO_3F and e) CsCaCO_3F .

properties of KSrCO_3F , RbSrCO_3F and KCaCO_3F and all these ground state properties are tabulated in Table 3.1. Since the G06 scheme is not yet implemented for 6th and 7th period elements of the periodic table we are unable to test it for CsCaCO_3F (see Table 3.1).

One of the key requirements for NLO materials is mechanical stability and this can be investigated by calculating the single crystal elastic constants of a material. These are fundamental properties for crystalline solids to describe the mechanical stability and stiffness of the solid against the applied strains. Stress-Strain method has been used to calculate the elastic constants. The compounds of the present

Table 3.1: The calculated ground state properties such as lattice parameters (a,c in Å) and volume (V in Å³) of ABCO₃F (A = K, Rb, Cs; B = Ca, Sr) compounds using standard LDA, GGA and dispersion corrected (G06, OBS) exchange-correlational functionals along with the experimental data taken from Ref.36.

Symmetry	Compound	Parameter	CA-PZ	PBE	PW91	G06	OBS	Expt ^a .
P6m2 (Z=1)	KCaCO ₃ F	a	4.972	5.159	5.150	5.131	5.091	5.096
		c	4.337	4.487	4.479	4.445	4.432	4.455
		V	92.87	103.48	102.91	101.37	99.49	100.23
	KSrCO ₃ F	a	5.132	5.320	5.314	5.280	5.257	5.259
		c	4.583	4.746	4.738	4.681	4.687	4.695
		V	104.55	116.36	115.89	113.03	112.24	112.50
	RbSrCO ₃ F	a	5.177	5.371	5.363	5.329	5.310	5.300
		c	4.667	4.835	4.825	4.765	4.781	4.790
		V	108.35	120.81	120.22	117.21	116.79	116.53
P6̄2m (Z=3)	RbCaCO ₃ F	a	8.987	9.300	9.285	9.214	9.199	9.197
		c	4.324	4.489	4.482	4.421	4.434	4.446
		V	302.52	336.32	334.74	325.12	325.02	325.77
	CsCaCO ₃ F	a	9.102	9.420	9.403	-	9.319	9.299
		c	4.432	4.607	4.596	-	4.546	4.540
		V	318.02	354.09	352.01	-	341.98	340.05

^a Ref. 36.

study crystallize in the hexagonal structure and hence they have five independent elastic constants namely C_{11} , C_{33} , C_{44} , C_{12} , and C_{13} . It is well known that, Born's criteria [52] of mechanical stabilities in a hexagonal crystal structure leads to the following restrictions.

$$C_{ii} > 0 \ (i=1,3,4), \ C_{11} > C_{12}, \ (C_{11} + C_{12})C_{33} > 2C_{13}^2$$

The computed values of C_{ij} (see Table 3.2) satisfy the above mentioned criteria implying the mechanical stability of these materials. In addition, it is also found that $C_{33} > C_{11}$, which shows the mechanical anisotropic behaviour along two crystallographic axes. The obtained elastic constants are listed in Table 3.2. Besides the single crystal elastic constants, the single crystal bulk modulus of these materials also calculated and the obtained bulk modulus follows the decreasing trend from $\text{KCaCO}_3\text{F} \rightarrow \text{RbCaCO}_3\text{F} \rightarrow \text{CsCaCO}_3\text{F}$; $\text{KCaCO}_3\text{F} \rightarrow \text{KSrCO}_3\text{F}$ and $\text{RbCaCO}_3\text{F} \rightarrow \text{RbSrCO}_3\text{F}$. This implies that the bulk modulus decreases in

Table 3.2: Calculated single crystal elastic constants (C_{ij} , in GPa), bulk modulus (B in GPa) of $ABCO_3F$ ($A = K, Rb, Cs$; $B = Ca, Sr$) compounds calculated at the PW91+OBS theoretical equilibrium volume.

Parameter	C_{11}	C_{33}	C_{44}	C_{12}	C_{13}	B
KCaCO ₃ F	103.3	119.7	23.9	31.2	23.8	53.7
KSrCO ₃ F	94.6	106.5	15.7	30.1	16.9	47.1
RbSrCO ₃ F	88.9	97.4	18.3	27.9	21.7	46.4
RbCaCO ₃ F	98.6	104.2	8.9	42.1	21.1	52.0
CsCaCO ₃ F	93.1	90.2	22.3	37.4	27.6	51.1

the presence of heavy metal atom due to increase of ionic radius in all these materials. However, the calculated bulk modulus of all these compounds are lesser than BBO (60 GPa) [53] and higher than KDP (27 GPa) [53] crystals. This behaviour indicates that, the presently studied compounds are relatively harder than KDP crystal and softer than BBO crystal.

3.3.2 Electronic band structure

Electronic structure calculations not only predict physical and chemical properties of the materials, but they also provide good insight to the experimentalists to synthesize novel materials for various applications. For instance, Kang et al [37] proposed two novel NLO materials and they find applications in the deep-UV region, which are yet to be synthesized. Now we discuss our results pertaining to electronic properties of $ABCO_3F$ ($A = K, Rb, Cs$; $B = Ca, Sr$) compounds through energy band structures and density of states. Since there are no precise experimental band gaps available for the presently investigated compounds, we have calculated the same using three different exchange-correlational functionals (GGA, Engel-Vosko (EV)-GGA and TB-mBJ) as implemented in WIEN2k. It is well known from the literature, [54–58] that the standard DFT functional LDA/GGA always underestimate band gap for the semiconductors and insulators. However, EV-GGA functional improves the band gap over LDA/GGA functionals and the semi-local potential TB-mBJ provides enhanced band gaps

than rest of the above mentioned functionals. In the present case, one could clearly see that the obtained band gaps are found to increase from GGA to EV-GGA then to TB-mBJ and are presented in Table 3.3. Also the band profiles are similar for all three exchange-correlational functionals. However, the reported experimental band gap value of these compounds are above 6.3 eV from optical absorption and our calculated band gaps with TB-mBJ functional are found to be around 7.9 eV for all these compounds. Recently, Kang and his co-workers [37] reported the band gaps of these compounds are around 6.3 eV with hybrid functionals and the difference between our calculations and Kang et al [37] results may be due to different methods used in the calculations. Though our predicted TB-mBJ band gaps differ by 1.6 eV from hybrid functional band gaps, these are comparable with the well known NLO materials such as lithium triborate (7.8 eV) [59], cesium triborate (7.3 eV) [60] and β -barium borate (6.4 eV) [59]. We hope our calculations will stimulate experimentalist to measure exact band gap of these materials. The calculated TB-mBJ band structures of the investigated compounds are shown in Fig 3.2. It is found that these materials are direct band gap insulators as the band gap occurs along A-A direction for KCaCO_3F , KSrCO_3F , and RbSrCO_3F and Γ - Γ for RbCaCO_3F and CsCaCO_3F between the valence band maximum (VBM) and conduction band minimum (CBM). Also, it can be seen that the valence bands are very flat due to CO_3 triangular planar unit similar to that of BO_3 units in borate crystals [24].

The calculated density of states (DOS) for KCaCO_3F , KSrCO_3F , RbSrCO_3F and RbCaCO_3F , CsCaCO_3F using TB-mBJ functionals are in Fig 3.3 and Fig 3.4, respectively. It is clearly seen from the PDOS, the oxygen 2p-states dominate near the Fermi level about -2 eV for all the materials. The states from fluorine atom are mainly predominant between -2 to -3 eV in KCaCO_3F , KSrCO_3F , and RbSrCO_3F (see Fig 3.3) whereas it is situated between -1 to -3 eV in RbCaCO_3F and CsCaCO_3F (see Fig 3.4) compounds. There is an overlap between 2p-states of carbon and oxygen atoms in the valence band region above -4 eV. The bottom

Table 3.3: Calculated electronic band gaps (in eV) of $ABCO_3F$ ($A = K, Rb, Cs$; $B = Ca, Sr$) compounds using with GGA-PBE, EV-GGA and TB-mBJ functionals within FP-LAPW method and compared with other calculations.

Compound	present			other ^a			
	GGA-PBE	EV-GGA	TB-mBJ	PBE	PBE0	B3LYP	sX-LDA
KCaCO ₃ F	4.45	4.99	7.92	3.90	6.31	5.84	5.85
KSrCO ₃ F	4.20	4.60	7.99	3.80	6.27	5.79	5.72
RbSrCO ₃ F	4.25	4.69	7.88	3.94	6.37	5.92	5.83
RbCaCO ₃ F	4.39	4.96	7.46	3.79	6.29	5.84	5.74
CsCaCO ₃ F	4.66	5.25	7.15	4.21	6.39	6.17	6.14

^a Ref.37

of the conduction band is mainly composed of 2p-states of carbon, oxygen atoms at about 8 eV and d-states of metal atoms (Ca, Sr, Rb, Cs) between 10 to 12 eV in all the compounds. Overall, an ionic behaviour found between alkali-alkaline earth atoms, CO₃ and F groups near the Fermi level. In addition to this, a strong covalent behaviour was observed between carbon and oxygen atoms within CO₃ anionic group. The bonding picture of these compounds can be more clearly showed from the charge density maps by plotting in specific crystallographic directions. As mentioned earlier these compounds are iso-structural, so one can expect the charge density of these compounds to be similar. The calculated charge density distribution for KCaCO₃F, KSrCO₃F, RbSrCO₃F along [0 0 1] are shown in Fig 3.5. From this, we observe that the charges are located between carbon and the neighboring oxygen atoms, which indicates a strong covalent bonding between these atoms within anionic CO₃ group. This is consistent with calculated DOS, which also shows strong overlapping between 2p-states of carbon and oxygen atoms (see Fig 3.3 and 3.4). Moreover, the charge density distribution of remaining atoms is almost invisible (see Fig 3.5) implying ionic bonding between metal and anions.

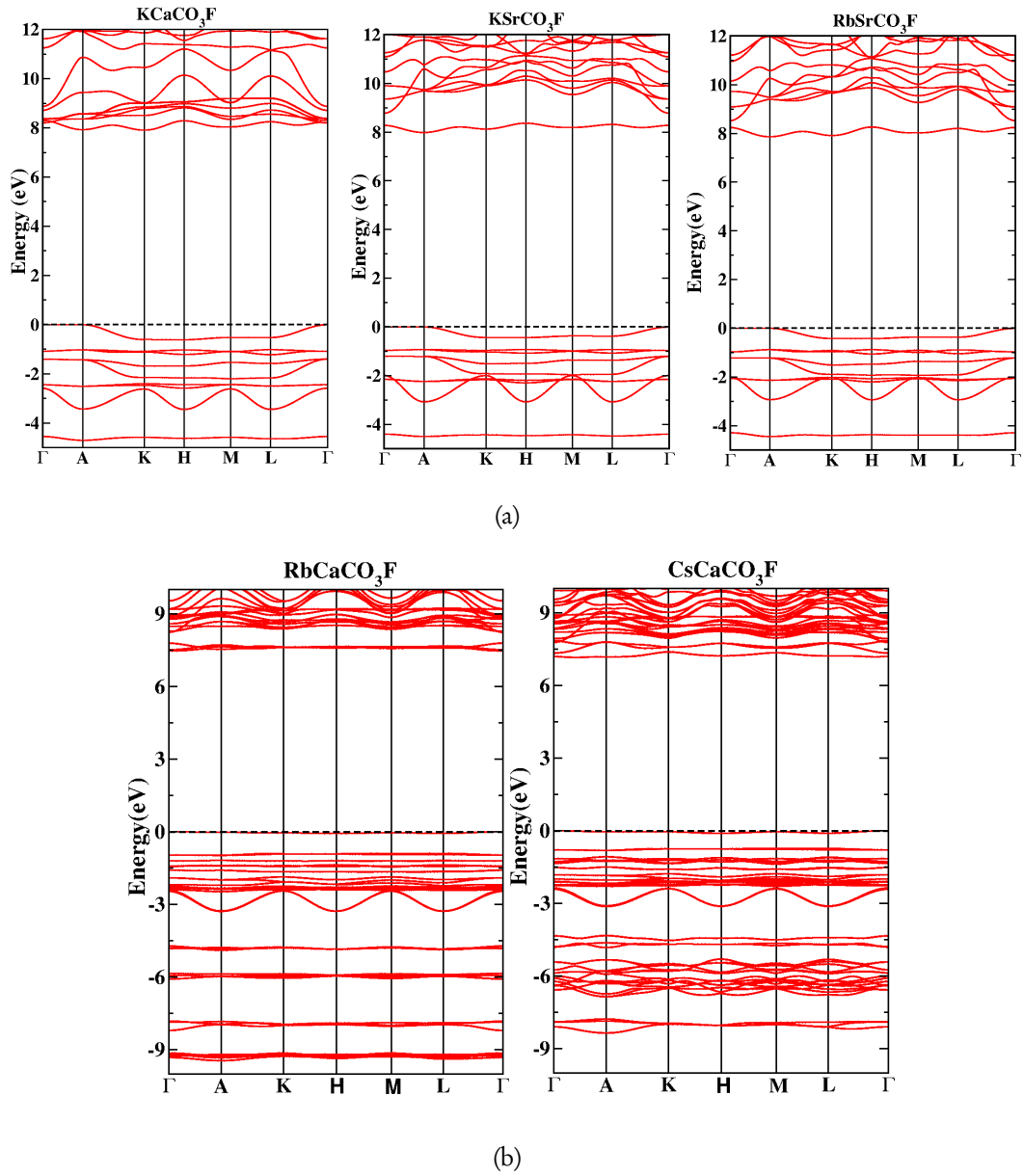


Figure 3.2: Calculated electronic band structure of (a) KCaCO_3F , KSrCO_3F and RbSrCO_3F , (b) RbCaCO_3F and CsCaCO_3F using TB-mBJ functional at experimental crystal structures.

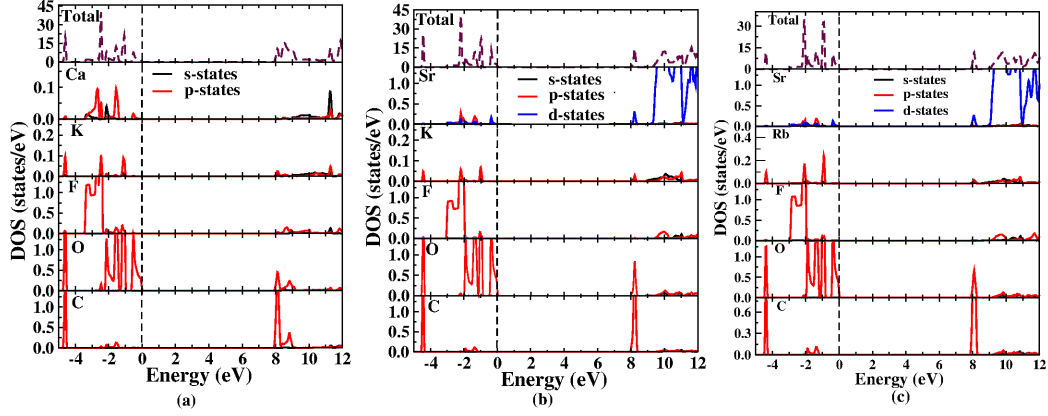


Figure 3.3: Calculated electronic DOS of (a) KCaCO_3F , (b) KSrCO_3F and (c) RbSrCO_3F using TB-mBJ functional at experimental crystal structures [36].

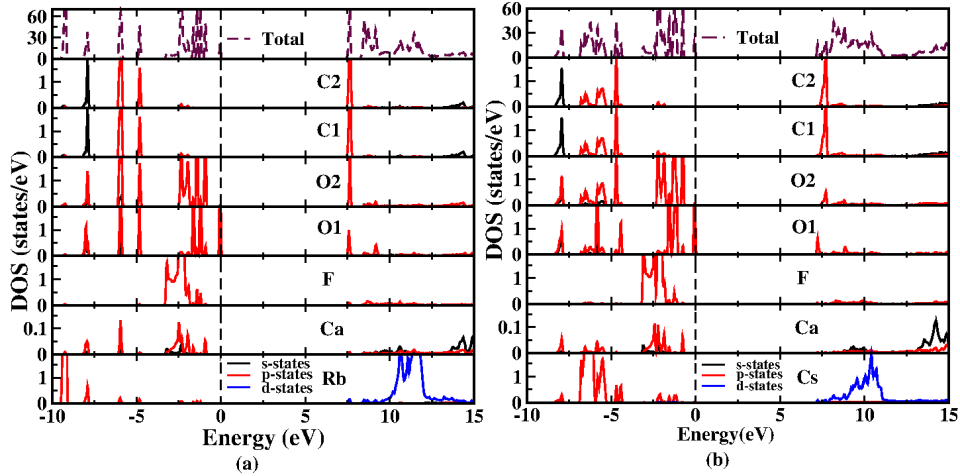


Figure 3.4: Calculated electronic DOS of (a) RbCaCO_3F , (b) CsCaCO_3F using TB-mBJ functional at experimental crystal structures [36]

3.3.3 Optical properties

The optical properties of these studied compounds are calculated using TB-mBJ functional. The optical properties of matter can be described by means of the transverse dielectric function $\epsilon(q, \omega) = \epsilon_1(\omega) + i\epsilon_2(\omega)$ where q is the momentum transfer in the photon-electron interaction and ω is the energy transfer. In the present study we have used electric-dipole approximation for the calculations, ac-

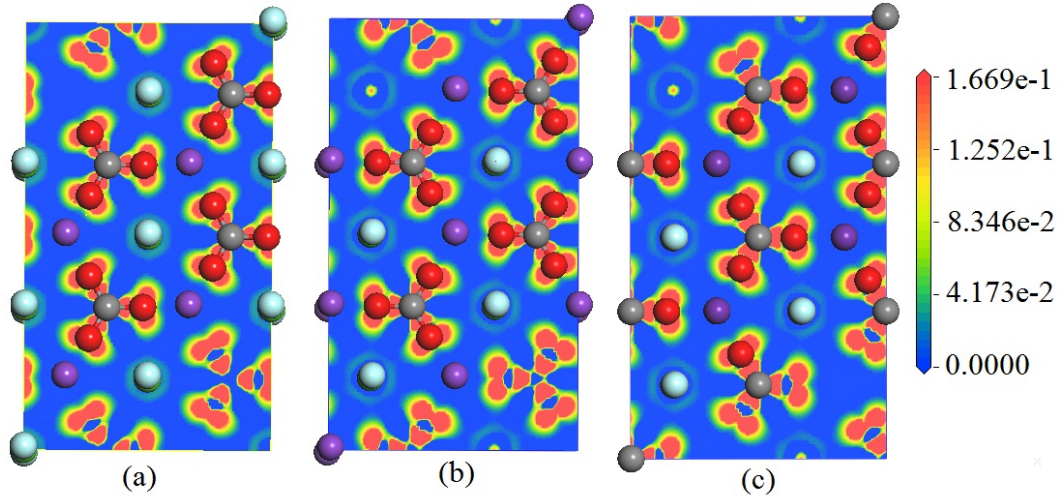


Figure 3.5: Charge density difference plot for KCaCO_3F , KSrCO_3F , RbSrCO_3F along $[0\ 0\ 1]$

According to which at $q = 0$, the momentum transfer from the initial state to the final state is neglected. The imaginary part of the dielectric tensor represents the direct interband transitions between valence band and conduction band states. According to the dipole selection rule, the inter band transitions only occurs in momentum quantum number of states which differ by unity. In order to calculate $\epsilon_1(\omega)$ using Kramers-Kronig transformation, it is necessary to evaluate the absorption spectrum to high energies in order to achieve a converged result for the dispersion. So we have calculated $\epsilon_2(\omega)$ up to 18 eV above the Fermi level. The knowledge of both the real and imaginary parts of the dielectric function allows the calculation of important optical properties such as absorption, refractive index and birefringence of the materials. The investigated compounds crystallize in the hexagonal symmetry, and this allows two non zero components of the dielectric tensor along $[1\ 0\ 0]$ and $[0\ 0\ 1]$ directions. Fig 3.6 shows the real (above) and imaginary (below) part of the dielectric function of ABCO_3F compounds. For simplicity, the prominent peaks are labelled as A, B, C, D, E along $[1\ 0\ 0]$ and P, Q, R, S, T along $[0\ 0\ 1]$ directions for all these compounds. We have

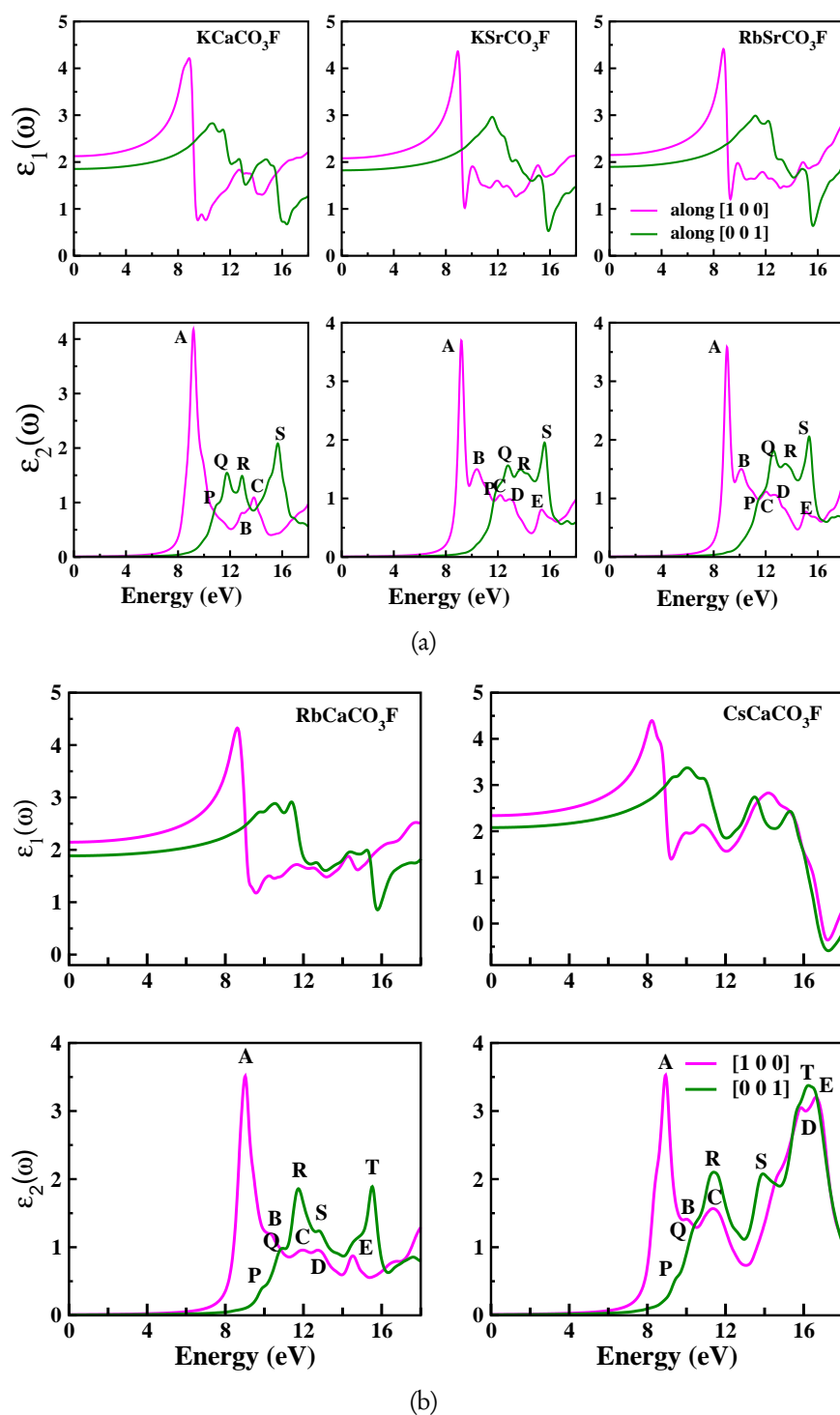


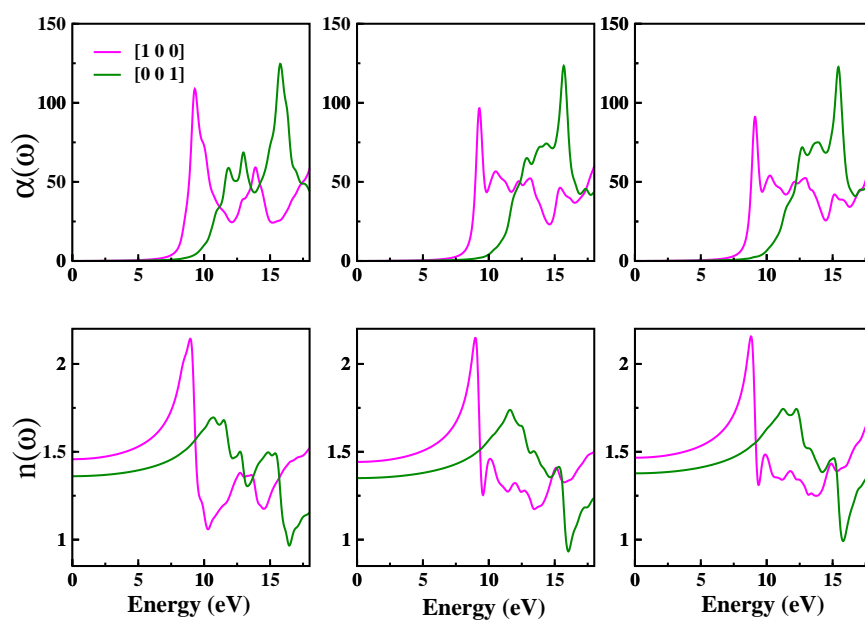
Figure 3.6: Complex dielectric function of (a) KCaCO_3F , KSrCO_3F and RbSrCO_3F , (b) RbCaCO_3F and CsCaCO_3F calculated using TB-mBJ functional at experimental crystal structures[36].

Table 3.4: The observed optical transitions of $ABCO_3F$ ($A = K, Rb, Cs$; $B = Ca, Sr$) from imaginary part of dielectric function using TB-mBJ electronic structure.

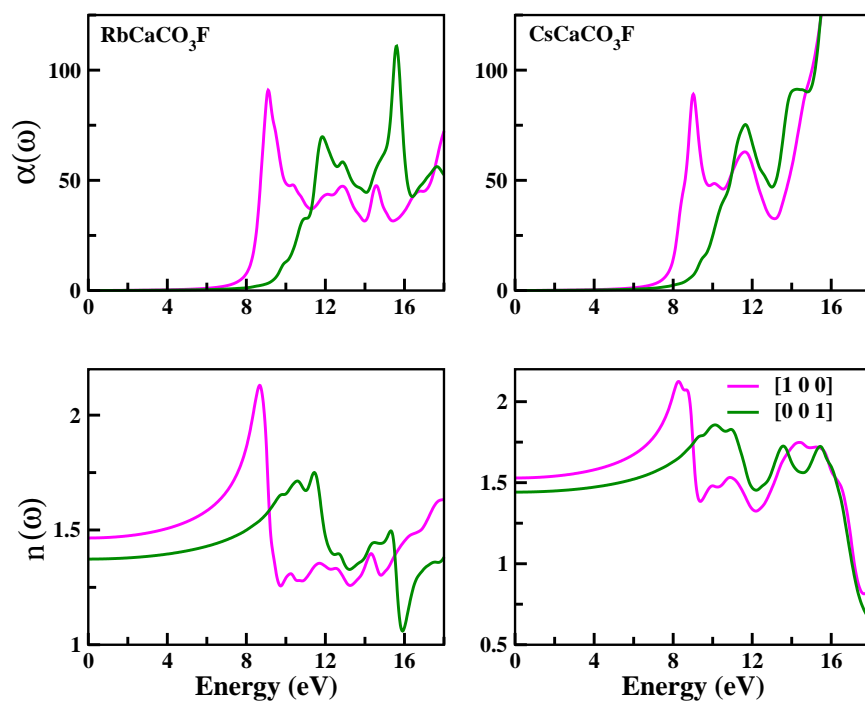
Direction	Peak	KCaCO ₃ F	KSrCO ₃ F	RbSrCO ₃ F	RbCaCO ₃ F	CsCaCO ₃ F
along [100]	A	9.23	9.21	9.05	9.06	8.91
	B	12.87	12.21	10.16	10.42	10.01
	C	13.82	12.87	12.07	11.94	11.35
	D	—	13.07	12.85	12.87	15.85
	E	—	15.32	15.12	14.58	16.62
along [001]	P	10.96	11.92	11.63	9.94	9.45
	Q	11.77	12.78	12.65	10.87	10.36
	R	12.92	13.69	13.53	11.79	11.37
	S	15.68	15.66	15.34	12.90	13.91
	T	—	—	—	15.55	16.27

observed several inter band transitions for these peaks by using our calculated TB-mBJ band structure from the imaginary part of the dielectric function, and the major contributions are tabulated in Table 3.4.

The peaks in imaginary part of dielectric function mainly arises due to inter band transitions between VBM and CBM in the different energy regions: a) $O(p) \rightarrow M(d)$ in 9-13 eV, b) $F(p) \rightarrow M(d)$ in 13-15 eV and c) $C/O(p) \rightarrow M(d)$, where M is Ca, Sr, Rb, Cs. From the imaginary part of the dielectric tensor, we can calculate the real part of dielectric constant $\epsilon_1(0)$ of these materials and the corresponding values are given in Table 3.5. The absorption spectra of these compounds are shown in Fig 3.7 (a), which shows large anisotropy in two crystallographic directions. The calculated absorption coefficients are presented in Table 3.5 and they indicate that absorption of these compounds lies in UV-region, which is in good agreement with experiments [36]. The calculated index of refraction in two different directions are shown in Fig 3.7 (b). From the figure, it can be seen that around 10 eV, all the materials show highest refractive indices and the calculated index of refraction at zero energy is tabulated in Table 3.5. We have also derived birefringence of all the compounds by using index of refraction between two directions of the unit cell. It is well known that, birefringence (Δn) is an important property to achieve the phase matching conditions and relatively large



(a)



(b)

Figure 3.7: Absorption and refractive indices of (a) KCaCO_3F , KSrCO_3F and RbSrCO_3F , (b) RbCaCO_3F and CsCaCO_3F calculated using TB-mBJ functional at experimental crystal structures.

Table 3.5: Linear optical properties such as real part of dielectric function ($\epsilon_1(\omega)$), absorption coefficient ($\alpha(\omega) \times 10^4$, cm^{-1}), refractive indices (n_o and n_e) and birefringence (Δn) of ABCO_3F ($A = \text{K, Rb, Cs}$; $B = \text{Ca, Sr}$) compounds

	$\epsilon_1^{[100]}(\omega)$	$\epsilon_1^{[001]}(\omega)$	$\alpha^{[100]}(\omega)$	$\alpha^{[001]}(\omega)$	n_o	n_e	$\Delta n (n_o - n_e)$
KCaCO ₃ F	2.1	1.0	106.1	31.8	1.4577	1.3611	0.0966
KSrCO ₃ F	2.1	0.9	95.6	41.6	1.4424	1.3503	0.0921
RbSrCO ₃ F	2.2	1.0	90.7	34.3	1.4663	1.3775	0.0889
RbCaCO ₃ F	2.15	1.89	90.3	10.7	1.4651	1.3732	0.0919
CsCaCO ₃ F	2.34	2.08	89.4	13.7	1.5291	1.4418	0.0873

value ($\Delta n \geq 0.08$) is observed in BO_3 group materials. However, the calculated Δn for all studied compounds are greater than 0.08 (shown in Table 3.5), which implies that these compounds are good phase matchable materials as borate group crystals.

3.4 Conclusions

In summary, the structural and elastic properties of alkali-alkaline earth carbonate fluoride NLO crystals were studied using plane wave pseudopotential method, whereas electronic and optical properties of these compounds studied using FP-LAPW method based on density functional theory. The calculated ground state properties of RbCaCO₃F and CsCaCO₃F using semi empirical dispersion correction method (OBS) are in good agreement with experimental data in contrast to standard LDA/GGA functionals. The single crystal elastic properties as well as bulk modulus of these materials also predicted at the OBS equilibrium volume. This analysis shows that all these compounds are mechanically stable and strong anisotropy exists between two crystallographic axes. From the calculated band structure and density of states, it is concluded that these compounds are direct band gap insulators and also a considerable enhancement is obtained in the band gap of these materials using TB-mBJ functional over EV-GGA and GGA-PBE. The major optical transitions have been observed between O/C (p -states) \rightarrow M (d -states), where (M = Ca, Sr, Rb, Cs). Finally, the other optical constants such

as absorption spectra, refractive indices and birefringence of these crystals also predicted. From the calculated absorption spectra, it is found that these materials have strong absorption in UV region and the birefringence of these compounds indicates the larger phase matching in these crystals. The present study will be helpful for potential use of these materials in NLO applications.

References

- [1] C.Chen, Y.Wang, B.Wu, K.Wu, W.Zeng and L.Yu, *Nature.*, 373, 322 (1995).
- [2] J. D.Grice, V.Maisonneuve and M.Lebanc, *Chem. Rev.*, 107, 114 (2007).
- [3] C.Chen, Z.Lin and Z.Wang, *Appl. Phys. B.*, 80, 1 (2005).
- [4] B.Ferguson and X.C.Zhang, *Nature Matter.*, 1, 26 (2002).
- [5] P. Becker, *Adv. Matter.*, 10, 979 (1998).
- [6] L. F.Mei, Y. B. Wang and C. T. Chen, *Mater. Res. Bull.*, 29, 81 (1994).
- [7] C. D.McMillen, and J. W.Kolis, *J. Cryst. Growth.*, 310, 2033 (2008).
- [8] C. T.Chen, Y. B.Wang, B. C.Wu, K. C.Wu, W. L.Zeng and L. H.Yu, *Nature.*, 373, 322(1995).
- [9] Y.Yang, S. L.Pan, H. Y.Li, J.Han, Z. H.Chen, W. W.Zhao and Z. D.Zhou, *Inorg. Chem.*, 50, 2415 (2011).
- [10] Y.Yang, S. L.Pan, J.Han, X. L.Hou, Z. X.Zhou, W. W. Zhao, Z .H. Chen and M.Zhang, *Cryst. Growth Des.*, 11, 3912 (2011).
- [11] S. C.Wang and N.Ye, *J. Am. Chem. Soc.*, 133, 11458 (2011).
- [12] S.Pan, J. P.Smit, B.Watkins, M. R.Marvel, C. L.Stern and K. R.Poepelmeier, *J. Am. Chem. Soc.*, 128, 11631 (2006).
- [13] L. M. Caroline, *Growth and Characterization of Some Organic and Semior- ganic Amino Acid Based Nonlinear Optical Single Crystals*, PhD Thesis, Bharath University, Chennai, India (2010).
- [14] J.Arlt and M.Jansen, *Z. Naturforsch.*, 45b, 943 (1990).

- [15] B. Albert, J. Arlt, M. Jansen and H. Erhardt, *Z. Anorg. Allg. Chem.*, **607**, 13 (1992).
- [16] X.-L. Chen, M. He, Y.-P. Xu, H.-Q. Li and Q.-Y. Tu, *Acta Cryst. E*, **60**, i50 (2004).
- [17] Y. P. Sun, Q. Z. Huang, L. Wu, M. He and X. L. Chen, *J. Alloys Compd.*, **417**, 13 (2006).
- [18] B. Aurivillius, *Acta Chem. Scand.*, **A37**, 159 (1983).
- [19] G. Zou, L. Huang, N. Ye, C. Lin, W. Cheng and H. Huang, *J. Am. Chem. Soc.*, **135**, 18560 (2013).
- [20] G. Lakshminarayana, J. A. Torres, T. C. Lin, I.V. Kityk and M. P. Hehlen, *J. Alloys Compd.*, **601**, 67 (2014).
- [21] R. Arun Kumar, *J. Chem.*, 2013, 154862 (2013).
- [22] Y.-N. Xu and W. Y. Ching, *Phys. Rev. B.*, **41**, 5471 (1990).
- [23] A. Borstzky, R. Brunger, Ch. Huang and R. Wallenstien, *Appl. Phys. B.*, **52**, 55 (1991).
- [24] Y.-N. Xu, W. Y. Ching and R. H. French, *Phys. Rev. B.*, **48**, 17695 (1993).
- [25] J. Li, C.-G. Duan, Z.-Q. Gu and D.-S. Wang, *Phys. Rev. B.*, **57**, 6925 (1998).
- [26] Z. Lin, J. Lin, Z. Wang, C. Chen and M.-H. Lee, *Phys. Rev. B.*, **62**, 1757 (2000).
- [27] D.S. Wang, *Bull. Mater. Sci.*, **26**, 159 (2003).
- [28] C. T. Chen, L. Bai, Z. Z. Wang and R. K. Li, *J. Cryst. Growth.*, **292**, 169 (2006).
- [29] C. Chen, *Sci. Sin.*, **22**, 756 (1979).

- [30] C. T.Chen, B. C. Wu, A. D.Jian and G.M.You, *Sci. Sinica Ser.*, **12**, 235 (1985).
- [31] C. T.Chen and G.-Z.Liu, *Ann. Rev. Mater. Sci.*, **16**, 203 (1986).
- [32] C. T.Chen, Y. C.Wu, A. D.Jiang, B. C.Wu and G. M.You, *J. Opt. Soc. Am. B.*, **6**, 616 (1989).
- [33] C. T.Chen, Y.Wu and R.Li, *J. Cryst. Growth.*, **99**, 790 (1990).
- [34] Y. C.Wu, T.Sasaki, S.Nakai, A.Yokotani, H.Tang, C.T.Chen, *Appl. Phys. Lett.*, **62**, 2614 (1993).
- [35] Y. P. Sun, Q. Z.Huang, L.Wu, M.He, X. L.Chen, *J. Alloys compd.*, **417**, 13 (2006).
- [36] G.Zou, N.Ye, L. Huang and X.Lin, *J. Am. Chem. Soc.*, **133**, 20001 (2011).
- [37] L.Kang, Z.Lin, J.Qin, C.Chen, *Sci. Rep.*, **3**, 1366 (2013).
- [38] M. C.Payne, M. P.Teter, D. C.Allen, T.A.Arias, J. D. Joannopoulos, *Rev. Mod. Phys.*, **64**, 1045 (1992).
- [39] M. D.Segall, P. J. D.Lindon, M. J.Probert, C. J.Pickard, P. J.Hasnip, S. J.Clark, M. C.Payne, *J. Phys: Condens. Matter.*, **14**, 2717 (2002).
- [40] J.P. Perdew, K.Burke, M.Ernzerhof, *Phys. Rev. Lett.*, **77**, 3865 (1996).
- [41] J. P.Perdew and Y.Wang, *Phys. Rev. B.*, **45**, 13244 (1992).
- [42] D. M.Ceperly and B.Alder, *J. Phys. Rev. Lett.*, **45**, 566 (1980).
- [43] J. P.Perdew and A.Zunger, *Phys. Rev. B.*, **23**, 5048 (1981).
- [44] J. P.Perdew and A.Zunger, *Phys. Rev.B.*, **45**, 13244 (1992).
- [45] D.Vanderbilt, *Phys. Rev. B.*, **41**, 7892 (1990).

- [46] F.Ortmann, F.Bechstedt and W. G. Schmidt, Phys. Rev. B., 73, 205101 (2006) .
- [47] S.Grimme, J. Comp.Chem., 27, 1787 (2006).
- [48] H. J.Monkhorst and J. D.Pack, Phys. Rev. B., 13, 5188(1976).
- [49] P.Blaha, K.Schwarz, G. K. H.Madsen, D.Kvasnicka and J.Luitz, WIEN2K, an Augmented Plane Wave + Local Orbitals Program for Calculating Crystal Properties ed K Schwarz (Wien, Austria: Technical Universitat) ISBN 3-9501031-1-2. (2001).
- [50] E.Engel and S. H. Vosko, Phys. Rev. B., 47, 13164 (1993).
- [51] F.Tran and P.Blaha, Phys. Rev. Lett., 102, 226401 (2009).
- [52] M.Born and K.Huang, Dynamical Theory of Crystal Lattices, Oxford University Press: Oxford, U.K., (1998).
- [53] M. Bass, C.DeCusatis, J.Enoch, V.Lakshminarayanan, G.Li, C.MacDonald, V.Mahajan and E. V.Stryland, Handbook of Optics, 3rd Ed. Vol. IV: Optical Properties of Materials, Nonlinear Optics, Quantum Optics, (2009).
- [54] D. J. Singh, Phys. Rev. B, 82, 205102 (2010).
- [55] D.Koller, F.Tran and P.Blaha, P. Phys. Rev. B., 85, 155109(2012).
- [56] D.Koller, F.Tran and P.Blaha, Phys. Rev. B, 83, 195134 (2011).
- [57] H.Dixit, R.Saniz, S.Cottenier, D.Lamoen and B.Partoens, J. Phys.: Condens. Matter., 24, 205503 (2012).
- [58] J. A.Camargo-Mart ez and R.Baquero, Phys. Rev. B, 86, 195106 (2012).
- [59] R. H. French, J. W.Ling, F. S.Ohuchi and C. T.Chen, Phys. Rev. B., 44, 8496 (1991).

- [60] Y. C.Wu, T.Sasaki, S.Nakai, A.Yokotani, H.Tang and C. T.Chen, Appl. Phys. Lett., 62, 2614 (1993).

Lead Carbonate Fluoride

CsPbCO_3F

In this chapter, the structural, elastic (single and polycrystalline), vibrational (IR spectra) and thermodynamic properties of CsPbCO_3F were broadly discussed.

4.1 Introduction

The recent studies reported in the literature and our previous chapter conclusions reveal that a new possible carbonate based group of NLO materials can serve as better candidate, like borates in UV and deep-UV frequency window [1-4, 7]. These crystals having $[\text{CO}_3]^{2-}$ unit as an anionic group with similar planar triangular structure arrangement as $[\text{BO}_3]^{3-}$, are proved to show good phase matchable behaviour in UV region with 3.33 (A= K, Rb and B= Sr), 3.61 (A= K and B= Ca), 1.11 (A= Rb, Cs and B= Ca) and 1.20 (A= Cs and B= Ba) times larger nonlinear coefficients than d_{36} (0.39 pm/V) of KDP crystal with good mechanical stability (bulk modulus 50 GPa) [1, 2]. Meanwhile, Kang et. al [7], theoretically proposed a new series of ABeCO_3F and AAlCO_3F_2 (A=Li, Na, K, Rb, Cs) compounds with IIA and IIIA light metal cations substitution in ABCO_3F series using density functional theory calculations. This study suggests the applications of carbonate fluoride materials in the deep-UV region by further reducing the absorption edges to around 150 nm. Recently, Zou et. al [8] synthesized a highly nonlinear lead carbonate fluoride crystal CsPbCO_3F by

solid state reactions. It crystallizes in noncentrosymmetric space group $P\bar{6}m2$ with $a=5.3888 \text{ \AA}$, $c=5.1071 \text{ \AA}$ with a monomolecular unit cell. The structure consists of alternately stacked $PbCO_3$ and CsF layers perpendicular to c -axis connected by $Pb-F-Pb$ chains parallel to c -axis. More recently in 2014, Thao Tran et al [4] synthesized $RbPbCO_3F$ crystal structure along with $CsPbCO_3F$ through solvothermal and conventional solid state techniques and found that $CsPbCO_3F$ crystallizes in noncentrosymmetric space group $P\bar{6}m2$ with $a=5.393 \text{ \AA}$, $c=5.116 \text{ \AA}$ with $Z=1$ formula unit per unit cell. Even though there are some dissimilarities existing between previously reported structures by Zou et al. and Thao Tran et al., in both cases the observed nonlinear coefficients are 530, 160 times higher than $\alpha\text{-SiO}_2$ crystal respectively. This seems to be the record value among all the reported carbonate fluoride materials till now. This uniqueness of the material and its promising optical responses are known to arise from $p\text{-}\pi$ interaction between Pb^{2+} and $[CO_3]^{2-}$ within $[Pb(CO_3)]$ layers strongly motivated us in addressing the in-depth structure-property correlation issues in this material through density functional theory approach. Moreover, the Lead based semiconductor materials like chalcogenides are known to show promising longer wavelength applications (infrared optoelectronics). Due to the lower direct band gap values ($E_g \sim 0.2 \text{ eV}$), high static dielectric constant (10^3 to 10^4) and high mobilities of charge carriers (up to $106 \text{ cm}^2/\text{V.s}$) these materials are known as best candidates for far-infrared spectral range applications [5]. This also motivated us to choose $CsPbCO_3F$ crystal for the present study.

In this chapter, we address the origin of NLO response of $CsPbCO_3F$, $ABCO_3F$ ($A=K, Rb$; $B=Ca, Sr$) crystals from the lattice dynamics point of view. We report the role of van der Waals (vdW) interactions in predicting the stability of the lead carbonate crystal structure and single crystal elastic constants. The polycrystalline properties of $CsPbCO_3F$, $RbSrCO_3F$, $KSrCO_3F$, $KCaCO_3F$ materials are also extracted from single elastic constant values using Voigt, Reuss, Hill approximations [9–11]. Zone centre vibrational frequencies (infrared (IR) spectra)

are calculated using density functional perturbation theory (DFPT) approach and complete mode assignments are analyzed in detail. We have examined the nature of directional bonding and intensity variations of different vibrational modes in detail based on the calculated Born effective charge (BEC) tensors. We report the thermodynamic properties which are crucial in exploring the practical applicability (durability) of an NLO material. To the best of our knowledge, such studies are not reported till now in the literature for the presently studied novel carbonate fluorides. In order to explore more about the vibrational nature of the bonds, we further turned our focus on the heat-conduction process. The thermodynamic properties entropy, Debye temperature, heat capacity, enthalpy, thermal expansion and intrinsic lattice thermal conductivity at different temperatures ranging from 5 K to 1000 K are reported. We have compared the obtained results with experimentally reported thermal conductivity values of several hexagonal types of NLO materials. Since there are several recent reports on crystal structures of carbonate fluoride materials, we explore the crucial structure-property correlation in carbonate group compounds on different aspects. We believe that, the properties studied in this work related to lattice dynamics part such as mechanical, vibrational and thermodynamic properties would open up new possibilities in the world of NLO materials.

4.2 Calculation methods

First-principles calculations play a very important role in explaining the structure-property correlations of various materials. Details obtained from these simulations are therefore very useful for the new developments in the domain of nonlinear optical materials and their possible practical applications. In the present work, we have used a quantum mechanics based Cambridge Series of Total Energy (CASTEP) program [12, 13], which works based on the plane-wave pseudopotential (PP) method. In order to calculate various structure dependent prop-

erties of the present carbonate materials of interest, we have taken the experimental structural details as given in references [1, 8]. Experimental geometry of CsPbCO_3F , ABCO_3F ($A = \text{K, Rb}$; $B = \text{Ca, Sr}$) are optimized with maximum tolerance's for energy 5.0×10^{-6} (eV/atom), stress 0.02 GPa, displacement 5.0×10^{-4} Å. Forces between atoms are minimized up to 0.01 eV/Å. Electron-ion interactions are treated using Vanderbilt Ultra-soft pseudopotential [18] to calculate the ground state structural and elastic properties with 380 eV cut-off energy. The Broyden-Fletcher-Goldfarb-Shanno (BFGS) minimizer is used for cell parameter optimization [19]. Local-density approximation (LDA) [14–16], Generalized gradient approximation (GGA) of Perdew-Burke-ErnZerhof (PBE) [17], Perdew-Wang 91 (PW91) [16] are used as exchange-correlation functionals to account the electron-electron interactions. The Ortmann-Bechstedt-Schmidt (OBS) [20] correction to PW91 is used to treat the weak van der Waals (vdW) interaction effects. Norm conserving pseudopotential [21] are used with the valence electrons of atoms as Pb ($5s^2 5p^6 5d^{10} 6s^2 6p^2$), Cs ($5s^2 5p^6 6s^1$), F ($2s^2 2p^5$), O ($2s^2 2p^4$), C ($2s^2 2p^2$), K ($3s^2 3p^6 4s^1$), Ca ($3s^2 3p^6 4s^2$), Rb ($4s^2 4p^6 5s^1$), Sr ($4s^2 4p^6 5s^2$) to calculate BEC's and zone centre vibrational frequencies of CsPbCO_3F , ABCO_3F ($A = \text{K, Rb}$; $B = \text{Ca, Sr}$) within the framework of density functional perturbation theory (DFPT) [22] with 1300 eV cut-off energy. It is well known that DFPT is an efficient technique over finite displacement method to calculate vibrational properties with similar accuracy in lower computational time. Moreover, it allows calculating the crystal response to the external electric field, atomic displacements [23]. From these results, it is possible to obtain various properties like vibrational intensities, Born effective charges etc. These DFPT and finite element methods are framed within the harmonic approximation [23]. The $11 \times 11 \times 10$ Monkhorst-Pack [26] k-grid with 80 irreducible k-points is used. The spacing 0.02 1/Å between k-points is used for better accuracy. The Born effective charge tensors for the compounds of present interest are obtained using linear response method through Gonze approximation [24]. The relation

between Born effective charges and vibrational mode intensities are as follows [25]. $I_i = [\sum_{j,k} F_{ij}^l A_{j,k}]^2$; $A_{ij} = \partial E / \partial q_i \partial \mu_j$. Here, A is atomic polar tensor or Born effective charge tensor, E total energy, q_i is Cartesian coordinate, F^l is eigenvector, μ_j is dipole moment. The thermodynamic properties like lattice heat capacity, Debye temperature, thermal conductivity, thermal expansion are also calculated for four iso-structural crystals ($z=1$) within the quasi-harmonic approximation. For metals at low T, the heat capacity can be represented by a sum of two terms. The electron contribution is proportional to T and the lattice contribution is proportional to T^3 (this is the Debye T^3 law). Thus, for metals, the Debye model can only be said to be approximate for the specific heat. But it gives a good approximation for the low-temperature heat capacity of insulators and semiconductors where other contributions from highly mobile conduction electrons are absent. We computed these properties to have an overview of how these materials would behave under temperature. Our work could be a starting point and motivation to the experimental workers in future. More details are presented in the results and discussion part, thermodynamic properties section.

4.3 Results and discussion

4.3.1 Structural, elastic and polycrystalline properties

The layered noncentrosymmetric material CsPbCO₃F under investigation crystallizes in $\bar{P}6m2$ (187) space group with lattice parameters $a = b = 5.3888 \text{ \AA}$, $c = 5.1071 \text{ \AA}$, $\alpha = \beta = 90 \text{ (deg)}$, $\gamma = 120 \text{ (deg)}$. The unit cell consists of one formula unit ($Z=1$) and the atoms Cs, C, F, Pb, O are situated at 1a, 1d, 1e, 1f, 6m Wyck-off sites. Moreover, the reported crystal structure of CsPbCO₃F is made up of alternate [Pb(CO₃)], [CsF] layers along c-axis in x-y plane as shown in Fig 4.1. The adjacent layers parallel to c-axis are connected through F-Pb-F bonds. The iso-structural ABCO₃F (A = K, Rb; B = Ca, Sr) compounds are also found to crystallize in same space group $\bar{P}6m2$ with hexagonal in crystal structure with $Z=1$

formula unit. The slight increment in lattice parameters and volumes are noted upon changing the heavier metal atoms in these structures, which is expected [1, 2]. Hereafter we are naming the above said 4 crystals KCaCO_3F , KSrCO_3F , RbSrCO_3F , CsPbCO_3F as KCa , KSr , RbSr , CsPb for simplicity. The atomic sites occupied by different atoms in KCa , KSr , RbSr phases are as follows. K, K, Rb at 1a, 1e, 1c; Ca, Sr, Sr at 1b, 1f, 1f; C atoms at 1d, 1d, 1b; O atoms at 3k, 3k, 3k; F atoms at 1a, 1e, 1e respectively. In all the crystals oxygen atoms are located at $\text{mm}2$ site symmetry, whereas all other atoms K, Rb, Ca, Sr, C, O, F are occupying $\bar{6}\text{m}2$ site symmetry out of 5 possible site symmetries for 187 space group. In this section we verify the effect of these different Wyckoff site occupancy's, chemical composition variations on structural, mechanical, polycrystalline properties in a detailed manner. As a first step, to obtain the correct lattice parameters and volume, we have optimized the experimental crystal structure of CsPbCO_3F using LDA functional, GGA (by applying PBE) exchange-correlation functionals as implemented in CASTEP code. The obtained ground state structural properties of lattice parameters and volume are given in Table 4.1. In comparison to the experimental data, we found that optimized volume with LDA is underestimated by 6.8%, with PBE functional overestimated by 4%, which is a considerable deviation from the experimental value. In order to capture the effect of non-bonding interactions between the adjacent layers, one needs to optimize the system with dispersion corrected schemes to the standard DFT functionals. Since the Grimme (G06) [27] corrections are not implemented for Pb, Cs elements for the present case, we performed further structural optimizations with PW91 functional and Ortmann et al. (OBS) correction [20] to PW91. The obtained volumes with PW91 (see Table 4.1) are also overestimated by >3% before including the vdW effects, with PW91+OBS the unit cell volume is slightly overestimated by 1% and is in relatively good agreement with experimentally reported data. Moreover, after inclusion of vdW corrections, improvement is observed in the prediction of lattice parameter 'a'. Whereas, 'c' is well reproduced before and after vdW interac-

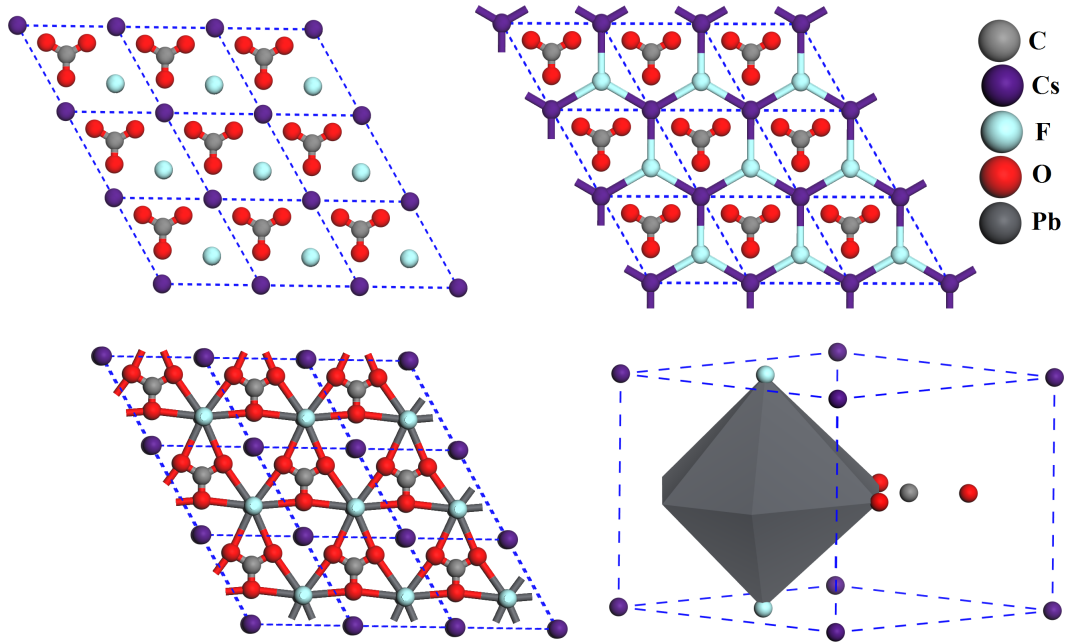


Figure 4.1: Experimental crystal structure of CsPbCO₃F consist of CsF and PbCO₃ layers.

Table 4.1: Calculated ground state lattice vectors (a, c in Å), volume (V , in Å³) of CsPbCO₃F, using LDA, PBE, PW91 and dispersion corrected PW91 (PW91+OBS) along with experimental data [8]

Symmetry	Compound	Parameter	LDA	PBE	PW91	PW91+OBS	Experiment
P $\bar{6}m2$ ($Z=1$)	CsPbCO ₃ F	a	5.322	5.515	5.507	5.477	5.388
		c	4.876	5.059	5.046	5.011	5.107
		V	119.648	133.275	132.577	130.215	128.437

tion's taken in to account. The percentage of deviations in 'a' with PBE, PW91, PW91+OBS functionals are 2.3%, 2.2%, 1.6% with respect to experimental value. With LDA functional 'a', 'c' are underestimated by 1.2%, 4.5%. Overall the results of structural optimization of CsPb indicates that the OBS correction method has reproduced the experimental results more accurately. The calculated bond lengths with OBS, PBE functionals are displayed in Table 4.2. We find that our calculations are in good agreement with experimental data for all the studied compounds.

Table 4.2: Calculated bond lengths (in Å) at OBS, PBE theoretical equilibrium structures of CsPbCO₃F and ABCO₃F (where A = K, Rb ; B = Ca,Sr) respectively along with experimental data[1, 8]

KCaCO ₃ F			KSrCO ₃ F			RbSrCO ₃ F			CsPbCO ₃ F		
Bond	Cal	Exp	Bond	Cal	Exp	Bond	Cal	Exp	Bond	Cal	Exp
Ca-F	2.248	2.2276	Sr-F	2.367	2.3478	Sr-F	2.405	2.3950	Pb-F	2.481	2.5536
Ca-O	2.585	2.5552	Sr-O	2.662	2.6397	Sr-O	2.686	2.6603	Pb-O	2.717	2.7084
Ca-C	2.977	2.9426	Sr-C	3.062	3.0367	Sr-C	3.088	3.0600	Pb-C	3.122	3.1110
Ca-K	3.731	3.6907	Sr-K	3.870	3.8385	Sr-Rb	3.914	3.8858	Pb-Cs	3.988	4.0250
K-O	2.808	2.7765	K-O	2.951	2.9260	Rb-O	2.998	2.7950	Cs-O	3.080	3.1420
K-F	2.977	2.9426	K-F	3.062	3.0367	Rb-F	3.088	3.0600	Cs-F	3.122	3.1120
C-O	1.295	1.2853	C-O	1.299	1.2910	C-O	1.299	1.2960	C-O	1.296	1.2810

At a fundamental level, the material response to the applied stress can be understood from the magnitude of elastic constants. Bulk modulus of a material will explain the response to isotropic compression. In order to predict these fundamental mechanical equilibrium properties, which are more sensitive to lattice vectors, we have used optimized crystal structure obtained with PW91+OBS functional. According to the symmetry elements, for hexagonal crystal the 36 independent elastic coefficients of 6x6 tensor matrix will reduce to just 5 independent constants. These C_{11} , C_{33} , C_{44} , C_{12} , C_{13} constants for the present studied hexagonal structure and the bulk modulus (B) values are calculated using stress-strain method. The obtained single crystal mechanical properties with OBS functional are presented in Table 4.3 along with PBE and PW91 functionals calculated values for comparison. To the best of our knowledge there are no experimental elastic constants reported in the literature for comparison. The obtained elastic constants before and after inclusion of vdW interactions satisfy Born's mechanical stability criteria derived for hexagonal system [37].

$$C_{ii} > 0 \ (i=1,3,4), \ C_{11} > C_{12}, \ (C_{11} + C_{12})C_{33} > 2C_{13}^2.$$

The lead carbonate crystal obeys this criterion and confirms its good mechanical stability. The variations in calculated elastic constants with PBE, PW91 and PW91+OBS functionals are related to the differences in their optimized lattice

parameters with each functional as shown in Table 4.1. Strong anisotropy for the externally applied strain along ‘a’, ‘c’ crystallographic directions is observed from the C_{11} , C_{33} values (see Table 4.3). The relation $C_{33} > C_{11}$ from the calculated results indicates that the crystal is more compressible along a-axis direction than c-axis for the applied strains. This effect can be attributed to weak bonding interactions between CO₃, Lead atoms (Pb-O) than the interlayer ionic interactions through F-Pb-F bonds. The bond lengths information of (Pb-O) > (Pb-F) also confirming the same (see Table 4.2). The huge differences in calculated elastic constants C_{11} , C_{33} with DFT and vdW (7.3 GPa; 9 GPa) also indicates that the accurate prediction of interactions between (CO₃, Pb) and adjacent CsF, PbCO₃ layers play an important role in explaining the crystal stability. The obtained bulk modulus value with and without vdW effect, 40 GPa & 41.5 GPa respectively indicates that, CsPbCO₃F is a soft material among all the ABCO₃F (where A = K, Rb, Cs; B = Ca, Sr) carbonate fluoride crystals and is harder than well known KH₂PO₄ (KDP) crystal (27 GPa) [38], α -SiO₂ (38 GPa) [38] and softer than β -BaB₂O₄ (BBO) crystal (60 GPa) [38]. In comparison to our previous study [2], we noticed that the presence of heavy metal Pb atom in its iso-structures like CsCaCO₃F (51.1 GPa), KSrCO₃F (47.1 GPa), KCaCO₃F (53.7 GPa), RbSrCO₃F (46.4 GPa), RbCaCO₃F (52.0 GPa) further reduced the hardness of the material by 22%, 13.5%, 22.7%, 11.8%, 25.3% respectively due to the increase in the atomic radii. The hardness of the studied carbonate fluoride materials follows the trend. KCaCO₃F > RbCaCO₃F > CsCaCO₃F > KSrCO₃F > RbSrCO₃F > CsPbCO₃F;

The occurrence of carbonate materials in alkaline rock complexes and their availability in powder forms, different size crystals at laboratory scales motivated us to also focus on their polycrystalline properties [6]. Since nonlinear optical materials are subjected to high power lasers for various applications like in high power nonlinear optical devices, frequency conversion applications [38], it is worthful to know their polycrystalline properties. We made an attempt to calculate different polycrystalline properties such as bulk modulus, shear mod-

ulus, Young's modulus, Poisson's ratio, shear anisotropy factors, elastic-Debye temperature from the single crystal elastic constants data. At first level, we have calculated the bulk (B_x), shear (G_x) modulus of CsPbCO₃F with Voigt (B_V , G_V), Reuss (B_R , G_R), Hill (B_H , G_H) approximations [9–11] by using the single crystal elastic constants. The average of the obtained values from Voigt, Reuss methods are taken as the suitable polycrystalline values as suggested by Hill for hexagonal symmetry [28, 29, 32]. We have also calculated similar properties of another isostructural compounds ABCO₃F (A=K, Rb; B=Ca, Sr) of lead carbonate fluoride based on the reported single crystal elastic constants in our previous work Nar-simha Rao et al [2]. The obtained results are compared and shown in Table 4.4. The relations for hexagonal systems which we have used in our calculations are described as follows: $B_V = (2/9) (C_{11} + C_{12} + 2C_{13} + ((1/2)C_{33}))$;

$$G_V = (1/30) (C_{11} + C_{12} + 2C_{33} - 4C_{13} + 12C_{55} + 12C_{66});$$

$$B_R = (C_{11} + C_{12})C_{33} - 2C_{12}^2 / (C_{11} + C_{11} + 2C_{33} - 4C_{13});$$

$$G_R = 15/(18B_V/C_2) + (6/(C_{11} - C_{12})) + 6/C_{44} + 3/C_{66};$$

$$\text{here } C_2 = (C_{11} + C_{12})C_{33} - 2C_{13}^2;$$

$$B_H = (1/2) (B_V + B_R); G_H = (1/2) (G_V + G_R); C_{66} = (1/2) (C_{11} - C_{12});$$

It is clear from the results that, the upper and lower limits of bulk moduli's (B_V , B_R) are found to be almost similar for the studied materials, whereas the results (Table 4.4) show considerable variations. Moreover, it is observed that $B_H > G_H$, which indicates that mechanical stability of the studied compounds is limited largely by shear moduli. KCa has a large G_H value, whereas CsPb is having lowest value among the studied carbonates. This indicates that bond restoring energy for the applied elastic shear strain is decreasing with increase of atomic number of metal atoms in the studied carbonates. In addition, according to Pugh's criterion [30, 31] the calculated B_H / G_H ratios > 1.75 indicates the ductile nature of studied crystals except KCa (1.67) which is found to be brittle. It was found that, the ductile nature of the studied materials increase with an increase in atomic radii of metal atoms. This behaviour is accompanied by the diversity present

in the calculated elastic constants values. Overall, Hills approximation of bulk modulus also confirms that CsPb is the softest material among all the carbonate materials. As a next step, we verified the resistance of the studied materials to the applied uniaxial tensions, stability against the shear strain there by calculating Young's modulus (E), Poisson's ratio (σ) [32]. Where $E = 9GB / (G + 3B)$; $\sigma = (E / 2G) - 1$. It is well known that, the magnitude of the Poisson's ratio is 0.1 for covalent, 0.25 for ionic materials [33]. In the present study, the obtained σ values (0.25) point to the mixed ionic-covalent nature of the studied carbonates. From another point of view, it is known that when magnitude of σ is 0.5 no change in volume occurs. From the obtained results as shown in Table 4.4, it is clear that large volume change can occur with elastic deformation of the studied crystals and it is relatively more for CsPb crystal than other carbonates. Overall the change in volume against the applied uniaxial strain in the studied layered materials increases with the metal atom's atomic radii from K to Sr and Sr to Pb. These observations are consistent with the calculated anisotropy factors.

Secondly, three shear anisotropy factors A_1 , A_2 , A_3 , elastic Debye temperature Θ_D for studied hexagonal materials at crystal density ρ [34, 35] are also calculated and analyzed. Where $A_1 = 2C_{44} / (C_{11} - C_{12})$; $A_2 = C_{33} / C_{11}$; $A_3 = C_{12} / C_{13}$. The obtained values are presented in Table 4.5 along with c/a ratios. It is observed that, calculated c/a ratios of studied crystals show increment with metal atom atomic radii. It is clear from the results that, all three anisotropy factors show considerable deviation from unity. This indicates that all the studied crystals possess large mechanical anisotropy. For studied carbonates, the anisotropy factor A_1 increased from 0.4-0.8, A_2 shows an almost constant value 1.1 whereas A_3 is showing a decreasing trend from 1.7-1.2. This is in consistent with the obtained decreasing trend of hardness (bulk modulus) of the studied materials upon insertion of heavier metal atoms. This behaviour might be arising due to the variations of inter layer interactions in (CO₃, metal atom) layer and intra layer interactions between (CO₃, metal atom) and K/Rb/Cs-F adjacent layers. Moreover, the de-

Table 4.3: Calculated single crystal elastic constants C_{ij} , bulk modulus B (in GPa units) of CsPbCO_3F for PBE, PW91, PW91+OBS theoretical equilibrium volume's

Method	Functional	C_{11}	C_{33}	C_{44}	C_{12}	C_{13}	B
DFT	PBE	63.0	71.9	15.7	34.9	24.0	40.4
DFT	PW91	67.1	71.3	15.6	37.3	22.0	40.7
vdW	PW91+OBS	70.2	80.2	16.3	31.8	22.4	41.5

creasing trend of C_{11} from $\text{KCaCO}_3\text{F} \rightarrow \text{KSrCO}_3\text{F} \rightarrow \text{RbSrCO}_3\text{F} \rightarrow \text{CsPbCO}_3\text{F}$ indicates that bonding between CO_3 group and metal atoms is becoming more ionic in nature. The increasing trend of C_{33} from $\text{CsPbCO}_3\text{F} \rightarrow \text{RbSrCO}_3\text{F} \rightarrow \text{KSrCO}_3\text{F} \rightarrow \text{KCaCO}_3\text{F}$ indicates that the interactions between alternate layers get strengthened. As a next step, elastic Debye temperature calculations are performed. It is well known that Debye temperature is a limit, below which the lattice shows stability mainly due to low electron phonon-coupling. Since at lower temperatures this quantity arises purely because of lattice modes, we made an attempt to calculate elastic Debye temperatures of the carbonate crystals based on the relations given in reference [36] between Young's modulus, shear modulus, bulk modulus and crystal density ρ and results are presented in Table 4.5. Results show that Θ_D decreases from KCa (479.7 K) to KSr (385.6 K) to RbSr (350.4 K) to CsPb (239.8 K). This trend suggests that the low melting point for lead carbonate fluoride and high for KCa. Since these crystals are newly synthesized, there are no experimental data available in the literature for above calculated properties. We expect that our simulated results will be helpful as a reference for material engineers in selection of the studied materials for real time applications.

4.3.2 Born effective charges (BEC) and static polarization

Born effective charge (BEC or, Z^*) is a fundamental quantity that demonstrates the coupling between electrostatic fields and lattice displacements. In order to explore more about the structural distortion, covalent and ionic bonding nature, local dipole moments and resulting polarization [39–42] of the present NLO crys-

Table 4.4: The Calculated bulk (B_X), shear moduli (G_X) values using the Voigt, Reuss, Hill approximations ($X=V,R,H$). Also listed the Poisson's ratio σ , B_H/G_H ratio. All values are calculated at the corresponding theoretical equilibrium volumes

Compound	B_V	B_R	B_H	G_V	G_R	G_H	σ	B_H/G_H
KCaCO ₃ F	53.7	53.8	53.8	33.2	31.1	32.1	0.25	1.67
KSrCO ₃ F	47.0	47.0	47.0	28.1	23.6	25.9	0.26	1.81
RbSrCO ₃ F	46.5	46.5	46.5	25.8	23.6	25.9	0.26	1.79
CsPbCO ₃ F	41.5	41.7	41.6	19.9	19.1	19.5	0.29	2.13

Table 4.5: Calculated values of c/a ratio, shear anisotropy factors (A_i)($i=1,2,3$), Young's modulus (E), crystal density (ρ), elastic-Debye temperature (Θ_D) at the theoretical equilibrium volumes

Compound	c/a	A_1	A_2	A_3	E	ρ	Θ_D
KCaCO ₃ F	0.869	0.6	1.1	1.3	80.4	2.538	479.7
KSrCO ₃ F	0.892	0.4	1.1	1.7	65.6	2.935	385.6
RbSrCO ₃ F	0.900	0.6	1.0	1.2	65.5	3.464	350.4
CsPbCO ₃ F	0.914	0.8	1.1	1.4	50.6	5.345	239.8

tals of interest, we have computed BEC's of all non-equivalent ions using linear response formalism as implemented in CASTEP code. The obtained results are shown in Table 4.6 and Table 4.8. The corresponding percentage of deviations from corresponding nominal ionic charges are shown in Table 4.7 and Table 4.9. The obtained results satisfy the acoustic sum rule, $\sum_k Z_{k,ii}^* = 0$ which in turn indicates good convergence of our calculations [44]. Moreover, it is known that, the BEC tensors obtained using linear-response and Berry's phase approach will be at the same level of accuracy [43]. The obtained large deviations in born effective charges from its nominal ionic charge indicate that these studied crystals possess mixed covalent-ionic behaviour. The BECs of CsPbCO₃F show larger deviations when compared to other crystals studied which also confirms that lead carbonate fluoride shows a more covalent nature. Moreover, BEC values are found to be highly direction dependent for the studied hexagonal structures which belong to $\bar{P}6m2$ space group. The diagonal elements of BEC tensors at carbon, fluorine, potassium, strontium, lead follows the relation $Z_{11}^* = Z_{22}^* \neq Z_{33}^*$. Whereas at

oxygen atoms, effective charges are more asymmetric and follows the relation $Z^*_{11} \neq Z^*_{22} \neq Z^*_{33}$. We compared the BEC tensors of CsPbCO₃F with the previously reported values by Thao Tran et al, [4] and results are found to be similar.

More specifically, the charge anisotropy ‘around metal atoms’ shows increment from Ca → Sr → Pb and it was found that $Z^*_{11} > Z^*_{33}$. This informs us that the covalent nature of these crystals is increased drastically upon increasing the atomic size of the metal atom in the carbonate fluoride crystals. However, it is more along ‘a’ direction (bond between metal-oxygen atoms of carbonate group (inter layer interactions)) bond than along ‘c’ (metal-fluorine bond between adjacent layers (intra layer interactions)) direction. In case of CsPb compound these Z^*_{11} , Z^*_{33} anisotropies around metal atoms are found to be ~ 60%, ~ 30% higher when compared to other KCa, KSr, RbSr crystals. The charge anisotropy ‘around fluorine atoms’ in all the studied crystals along ‘a’ axis is increased as follows RbSr → KCa → KSr → CsPb. It is clear from calculated data (as shown in Table 4.6), that the BEC of fluorine atom for the studied materials is deviated from its ionic charge -1 as follows: Along a-axis → CsPb(-0.87) < KSr(-0.91) < KCa(-0.94) < RbSr(-0.98); Along c-axis → CsPb(-2.90) > KSr(-1.81) > RbSr(-1.76) > KCa(-1.73). This confirms that ionic nature of fluorine bond with Rb, K, K, Cs in RbSr, KCa, KSr, CsPb compounds got enhanced. Whereas in ‘c’ direction anisotropy of fluorine increased from KCa → RbSr → KSr → CsPb. This indicates that, the bond between fluorine and Ca (in KCa), Sr (in RbSr), Sr (in KSr), Pb in (CsPb) is becoming more covalent in nature. Especially in the CsPb phase, the deviation of charge from its ionic value increases along ‘a’ (by ~ 4%) and ‘c’ (by ~ 100%) directions when compared with the other KCa, RbSr, KSr phases. The BECs of the O₁, O₂ and O₃ oxygen atoms in all the studied crystals show more or less similar deviation when compared to their nominal ionic charge of -2. This confirms the strong covalent bonding behaviour between carbon and oxygen atoms inside the anionic group. Overall, it has been found that BEC values are strongly affected by change in atoms at A, B site in ABCO₃F (where A = K, Rb, Cs and B = Ca,

Sr, Pb) and atomic bonds associated with them.

4.3.3 Vibrational modes and symmetry analysis

Study of fundamental vibrational properties of functional groups present in the crystal plays a crucial role in understanding the structure details and inter-molecular interactions in the low energy region. In this section we present the zone centre vibrational frequencies of CsPbCO₃F and other three iso-structural compounds ABCO₃F (A=K, Rb; B=Ca, Sr) crystals. The mode assignments of all the obtained frequencies are analyzed and are shown in Table 4.10, 4.11. All these four iso-structural compounds crystallize in $\overline{P6}m2$ space group, having single formula unit (7 atoms/cell). According to symmetry rules for $D_{3h}(-6m2)$ point group, the atoms of CsPbCO₃F, KSrCO₃F compounds are occupying Wyckoff positions as (Pb, Sr)-1*f*, F-1*e*, (Cs, K)-1*a*, C-1*d*, O-3*k*. A slightly different atomic configuration in case of KCaCO₃F are as follows : K-1*e*, Ca-1*b*, F-1*a*, C-1*d*, O-3*k* positions and for RbSrCO₃F atoms are situated at Sr-1*f*, Rb-1*c*, F-1*e*, C-1*b*, O-3*k* sites. According to the symmetry group theory analysis [45], the distribution of 3 acoustic (external) and 18 optical (internal) possible vibrational modes for these set of compounds are as follows.

$$\Gamma_{acoustic} = A_2'' \oplus E'$$

$$\Gamma_{optic} = A_1' \oplus A_2' \oplus 4A_2'' \oplus 5E' \oplus E''$$

The calculated 21 frequency modes from the present study are in good agreement with above mentioned group theory representations for all the crystals.

Table 4.6: Calculated BEC's of Pb, Ca, Sr, F, Cs, Rb, K, C atoms at the theoretical equilibrium volume's along with previously reported [4] values in parenthesis

Atom	Ionic	KCaCO ₃ F		KSrCO ₃ F		RbSrCO ₃ F		CsPbCO ₃ F	
		Z* ₁₁	Z* ₃₃	Z* ₁₁	Z* ₃₃	Z* ₁₁	Z* ₃₃	Z* ₁₁	Z* ₃₃
Ca,Sr,Pb	+2	2.42	2.31	2.43	2.36	2.47	2.37	3.63(3.7)	3.17(3.0)
F	-1	-0.94	-1.73	-0.91	-1.81	-0.98	-1.76	-0.87(-0.9)	-2.90(-2.9)
Cs,Rb,K	+1	1.15	1.30	1.18	1.29	1.20	1.40	1.28(1.3)	1.56(1.5)
C	+4	2.86	0.14	2.86	0.10	2.97	0.06	2.87(2.8)	0.05(0.04)

Table 4.7: Calculated percentage of deviations of BEC's of Pb, Ca, Sr, F, Cs, Rb, K, C atoms at the theoretical equilibrium volumes

Atom	KCaCO ₃ F		KSrCO ₃ F		RbSrCO ₃ F		CsPbCO ₃ F	
	Z* ₁₁	Z* ₃₃	Z* ₁₁	Z* ₃₃	Z* ₁₁	Z* ₃₃	Z* ₁₁	Z* ₃₃
Ca,Sr,Pb	21.05	15.65	21.75	18.15	23.6	18.95	81	58.6
F	-5.7	73.6	-8.2	81.8	-2	75.9	-12.7	190.5
Cs,Rb,K	15.6	30.3	17.8	29.4	20.7	40.6	28.3	56.6
C	-28.5	-96.4	-28.42	-97.47	74.25	-98.52	-28.27	-98.65

Table 4.8: Calculated BEC's of O₁, O₂, O₃ atoms (have nominal ionic charge -2) at the theoretical equilibrium volumes

KCaCO ₃ F			KSrCO ₃ F			RbSrCO ₃ F			CsPbCO ₃ F		
Z* ₁₁	Z* ₂₂	Z* ₃₃	Z* ₁₁	Z* ₂₂	Z* ₃₃	Z* ₁₁	Z* ₂₂	Z* ₃₃	Z* ₁₁	Z* ₂₂	Z* ₃₃
-1.61	-2.04	-0.67	-2.27	-1.43	-0.64	-1.66	-2.11	-0.69	-2.24(-2.3)	-2.36	-0.62 (-0.6)
-2.26	-1.39	-0.67	-1.64	-2.06	-0.64	-2.34	-1.43	-0.69	-2.43(-2.3)	-2.17	-0.62 (-0.6)
-1.61	-2.04	-0.67	-1.64	-2.06	-0.64	-1.66	-2.11	-0.69	-2.24(-2.3)	-2.36	-0.62 (-0.6)

Table 4.9: Calculated percentage of deviation's of BEC's of O₁, O₂, O₃ atoms from it's nominal ionic charge -2

KCaCO ₃ F			KSrCO ₃ F			RbSrCO ₃ F			CsPbCO ₃ F		
Z* ₁₁	Z* ₂₂	Z* ₃₃	Z* ₁₁	Z* ₂₂	Z* ₃₃	Z* ₁₁	Z* ₂₂	Z* ₃₃	Z* ₁₁	Z* ₂₂	Z* ₃₃
-19.5	2	66.5	13.5	-28.5	-68	-17	5.5	65.5	12	18	-69
13	-30.5	66.5	-18	3	-68	+17	-28.5	65.5	21.5	8.5	-69
-19.5	2	66.5	-18	3	-68	-17	5.5	65.5	12	18	-69

Apart from 3 acoustic modes, among the 18 possible optical modes we observe that four modes (A_2'') are infra-red (I) active, three modes (E'' , A_1') are Raman (R) active, 10 modes (E') are combined infra-red + Raman active (I+R). Interestingly one silent mode is observed with A_2' symmetry from our results for all the compounds. Negligible change in polarization and dipole moment due to CO₃ rotational mode (see Fig 4.3) could be the possible origin.

The calculated modes in the 'higher frequency region' (> 600 cm⁻¹) are in good agreement with the available experimental data as shown in Table 4.10. These modes arise due to the vibration of CO₃ unit alone for all the studied compounds. The vibrations of CO₃ unit observed based on CASTEP animations and in refer-

ence to the previous reports [46, 47] are assigned as follows. The frequency mode between 660 and 690 cm⁻¹ corresponds to doubly degenerate asymmetric in-plane bending; between 820 and 840 cm⁻¹ is due to symmetric out-of-plane bending; between 1030 and 1060 cm⁻¹ is because of symmetric stretching (breathing mode); between 1370 and 1430 cm⁻¹ is due to doubly degenerate asymmetric stretching. Further, in the ‘lower frequency region’ (< 400 cm⁻¹), vibrational modes for all the present investigated compounds mainly arise from the librational, translational, rotational motions of CO₃ group and stretching, bending motion of metal atom (M) - F (where M = Ca, Sr, Pb) bonds (see Fig 4.3). Whereas in ‘mid frequency region’, in contrast to the experimental results[8], we do not observe any Pb-F vibrational mode at 407 cm⁻¹ in case of CsPbCO₃F. It is clear from Fig 4.2, 407 cm⁻¹ mode is further shifted down to the lower frequency side. The larger values of BEC’s suggests that, the presence of dominant LO-TO splitting might be the possible reason for this discrepancy. The low frequency mode assignments are analyzed as shown in Table 4.11 and it is found that at least one silent mode is observed for every studied compound. Snapshots of all these CO₃ vibration’s are shown in Fig 4.3 for further reference.

It is observed from the calculated IR spectra that all peaks (from 1–8), as shown in Fig 4.2, are red shifted with an increase in the atomic number. The changes in intensity of the different frequencies are attributed to variation in the probability of vibrational transition occurrence from the ground state to the excited states. Due to the same symmetry of the studied crystals, equal number of absorption peaks (8) are found to occur in the spectra. As a starting point, we analyzed the reasons for the frequency shifts and the origin of the intensity variations will be discussed based on the obtained BEC’s later.

In the higher frequency region (> 600 cm⁻¹), the peak number 8 (I+R mode) corresponding to the asymmetric vibration of CO₃ group, is red-shifted considerably from KCa → RbSr → CsPb with a slight variation in the intensity. Whereas in case of KSr and RbSr the peak position is almost constant. The existence of di-

rectional bonding (covalent/ionic) interactions between anionic group and metal atoms, causes this frequency shift due to increment in the atomic mass of metal atoms. From Table 4.6 and Table 4.8 it is clear that, anisotropy in BEC's of carbon and oxygen atoms are almost constant for KCa, KSr and similarly for RbSr, CsPb. This manifests similar intensities of peak 8 for (KCa, KSr) and (RbSr, CsPb) compounds. A slight increment in intensity from KCa, KSr \rightarrow RbSr, CsPb is attributed due to differences in the carbon and oxygen BEC deviations from their respective nominal ionic charges. In addition, the obtained trends in bond lengths between metal atom and oxygen atoms (Pb-O) > (Sr-O) > (Ca-O) suggests that, bending of CO₃ in CsPb to occur at lower frequencies than the other studied crystals. This could be the possible reason behind the soft nature (41.6 GPa) of CsPb than KCa (53.8 GPa). Moreover, KSr and RbSr possess almost similar hardness (47.0 GPa, 46.5GPa) due to similar Sr-O interactions.

Position and intensity of peak number 7 (IR active) which arises from the symmetric bending of CO₃ group, is almost constant for all the studied crystals and in turn suggesting the IR absorption of this mode is less affected with respect to atomic number of metal atoms. The peak 6 which is active in infra-red and Raman, arises due to asymmetric in-plane bending mode of CO₃. This peak shows less shift in peak position but huge intensity increment in case of lead carbonate fluoride compared to other carbonates. This can be due to the larger change in BEC's of both 'C' and 'O' atoms of lead carbonate fluoride in xy-plane (Z^*_{11} , Z^*_{22}) than other studied crystals. The different effective charges of C, O atoms in lead carbonate material makes CO₃ more polarizable. The peak 5 (IR active mode) corresponds to asymmetric stretching mode of Ca-F, Sr-F bond and is red shifted with constant intensity from KCa \rightarrow KSr \rightarrow RbSr. Interestingly no peak corresponding to Pb-F bond is observed in this region as reported in the literature. The reason for this shift is attributed to different bond lengths of Ca-F is 2.248 Å in KCa, Sr-F is 2.367 Å in KSr and Sr-F is 2.405 Å RbSr crystals. In the lower frequency range (below 200 cm⁻¹), the spreading of the vibrational spectrum is

different for each of the studied carbonates as shown in Fig 4.2. Even though compounds from KSrCO₃F to CsPbCO₃F are iso-structural, their IR spectra below 200 cm⁻¹ are very different and frequencies are spreading over in equal region 50 - 200 cm⁻¹. Whereas in case of KCaCO₃F it is between 100-200 cm⁻¹, for RbSrCO₃F lies in-between 75-175 cm⁻¹. It is observed from the Table 4.11 that the highest intensity mode in this region (see Fig 4.2) arises due to the combination of symmetric bending of Ca/Sr/Pb - F bond and translation of CO₃ group. In case of KCaCO₃F, KSrCO₃F, RbSrCO₃F the position of this highest intensity peak is almost constant but for lead carbonate fluoride is red-shifted due to heavier mass of the lead atom. In the lower frequency window, the higher intensity modes (peak 5, 3 in KCa, peak 4, 5 in KSr, RbSr and peak 5, 4, 3) are mainly found to arise because of Ca-F, Sr-F, Pb-F vibrations along with CO₃ vibrations. The intensities of remaining optical modes in this window are found to be higher for CsPbCO₃F compound which also confirms the effect of higher BEC's.

Overall the higher intensities for all the IR modes of lead carbonate fluoride is observed, suggesting that it is optically more active material in IR region than other studied carbonates. The contribution from CO₃ group vibrations (peak 6, 8) in the near IR region to the optical response is more in case of CsPb than others. Our results show a similar trend and give a hint about the different optical responses of carbonate fluorides for the same incident light of 1064 nm which was reported in the literature [1, 8] as 13.6, 3.61, 3.33 and 3.33 higher nonlinear coefficients than the well known KDP crystal.

4.3.4 Thermodynamic properties

Investigation of the thermal behaviour of a nonlinear optical material is important in exploring the knowledge about the crystal growth issues, solid state physics and chemistry, crystal chemistry and its possible practical applications [49]. It is known that thermal expansion of the crystal can lead to changes in the shape/dimension of the sample and specific heat can impact the damage threshold thereby limiting

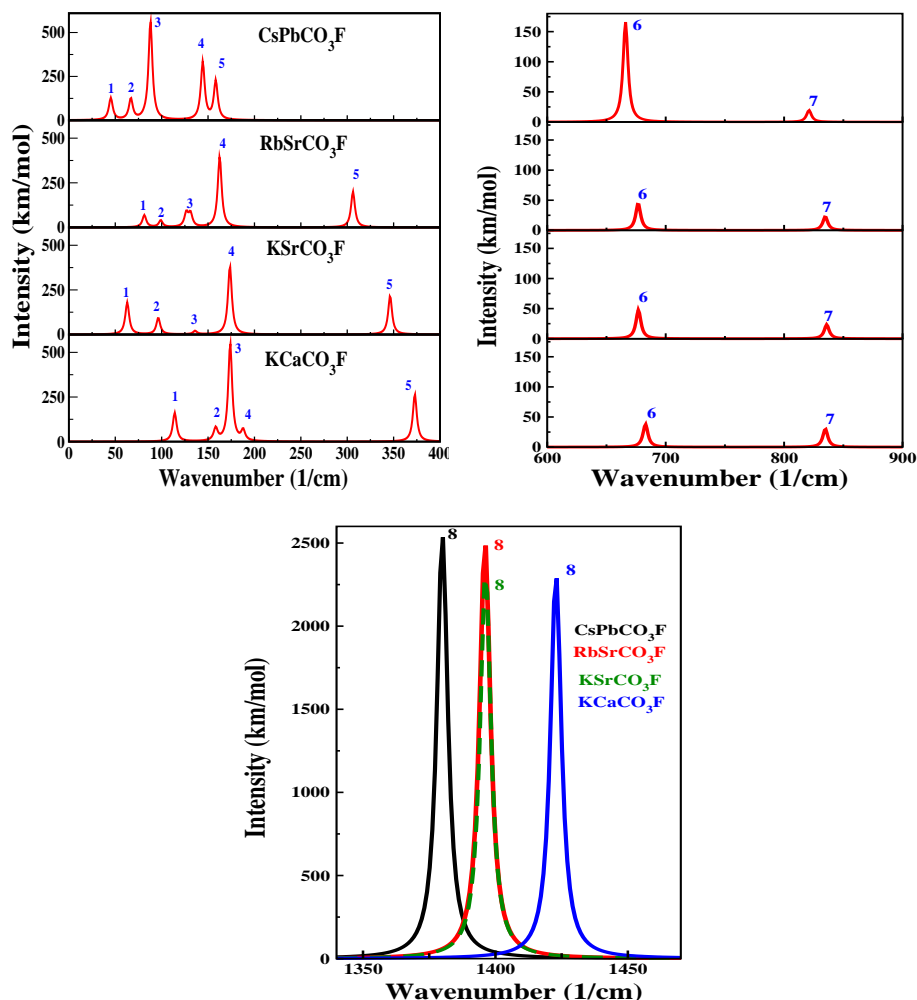


Figure 4.2: Calculated zone centre vibrational (IR) spectra in Far-IR, mid-IR, near IR regions of CsPbCO₃F and ABCO₃F (where A = K, Rb ; B = Ca, Sr) (from left to right) at theoretical equilibrium structure.

the use of the material for industrial applications. Information about the thermal conductivity of an NLO material is very useful in determining its ability to transfer heat into the air thereby affecting the quality of the output beam [38, 48]. So, we made an attempt to calculate the thermodynamic properties of the present novel carbonate fluoride materials. Here we apply the quasi-harmonic Debye model [50], in which Gibb's free energy (G) of the system takes the following form $G(V,P,T) = E(V) + PV - TS$ where $E(V)$ is the total energy, V is the volume

Table 4.10: The calculated zone centre high frequency vibrational modes (in cm^{-1}) of CsPbCO₃F and ABCO₃F (where A = K, Rb ; B = Ca, Sr) and their assignments [Here I= IR active mode, R= Raman active mode]. Experimentally reported frequencies are given in parenthesis [1]

Mode	CsPbCO ₃ F	RbSrCO ₃ F	KSrCO ₃ F	KCaCO ₃ F	Symmetry
M21-M20	1379.70(1407)	1396.05	1396.68	1422.84	E (I+R)
M19	1038.39(1049)	1034.91	1032.89	1053.59	A ₁ (R)
M18	821.06(843)	834.74	835.83	834.78	A ₂ (I)
M17-M16	665.89(689)	676.78	676.94	682.94	E (I+R)

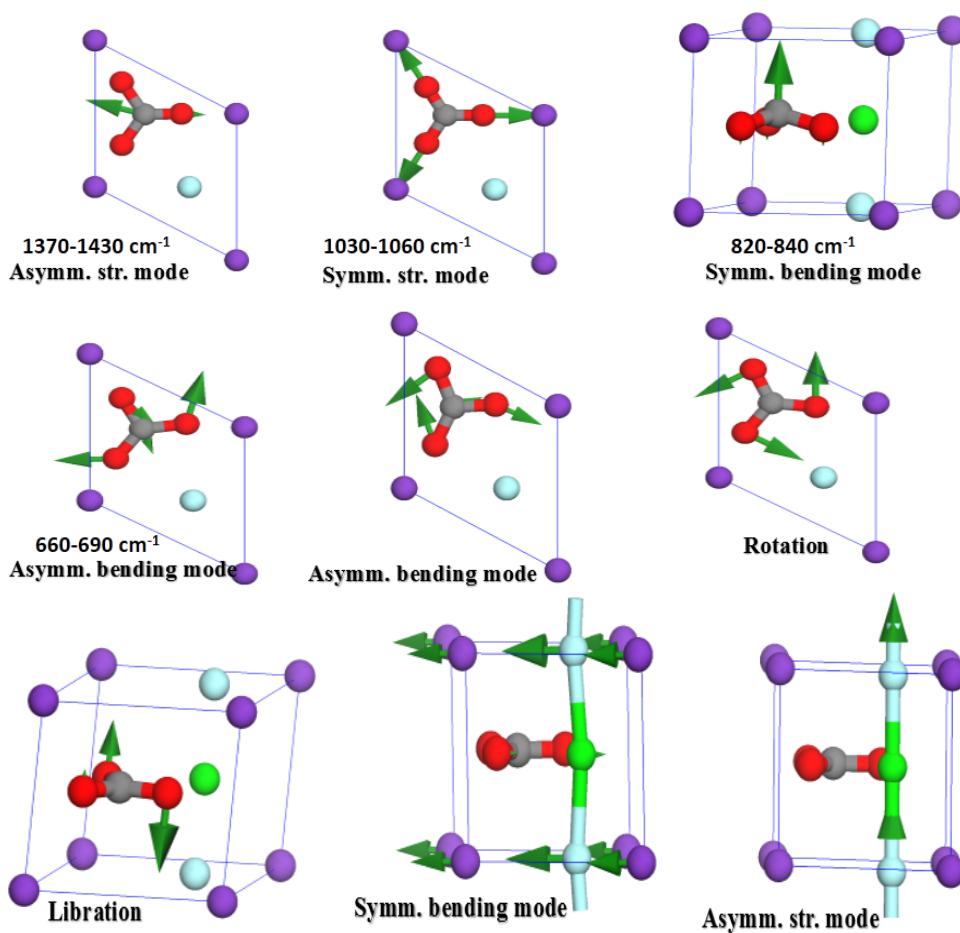


Figure 4.3: Snapshots of different vibrational mode animations of carbonate fluorides materials.

and S is the entropy of the system. Since the electronic structure calculations

Table 4.11: The calculated zone centre low frequency vibrational modes of CsPbCO_3F and ABCO_3F (where $A = \text{K, Rb}$; $B = \text{Ca, Sr}$) and their mode assignments [Here Trans. = Translation, Asymm. = Asymmetric, str. = Stretching]

Compound	Mode	PBE	Symmetry	Assignment of modes
KCaCO_3F	M15	372.86	$A_2^{\parallel}(\text{I})$	Asymm. str. mode of Ca-F
	M14	187.82	$A_2^{\parallel}(\text{I})$	Trans. of (CO_3) , Trans. of (Ca-F)
	M13-M12	173.86	$E^{\perp}(\text{I+R})$	Symm. bending of (Ca-F), Trans. of (CO_3) ,
	M11	158.41	$A_2^{\parallel}(\text{I})$	Trans. of (K, CO_3)
	M10-M09	157.27	$E^{\perp}(\text{I+R})$	Trans. of (CO_3, K) , Symm. bending of (Ca-F)
	M08-M07	150.67	$E^{\parallel}(\text{R})$	Libration of (CO_3)
	M06-M05	114.07	$E^{\perp}(\text{I+R})$	Symm. bending of (Ca-F), Trans. of (K)
	M04	98.12	$A_2^{\perp}(\text{silent})$	Rotation of CO_3
KSrCO_3F	M15	346.32	$A_2^{\parallel}(\text{I})$	Asymm. str. mode of Sr-F
	M14	175.77	$A_2^{\perp}(\text{Silent})$	Rotation of CO_3
	M13-M12	173.09	$E^{\perp}(\text{I+R})$	Trans. of (CO_3) , symmetric bending of (Sr-F)
	M11	136.06	$A_2^{\parallel}(\text{I})$	Rot. mode of CO_3 group
	M10-M09	115.33	$E^{\perp}(\text{I+R})$	Trans. of (CO_3, K) , symmetric bending of (Sr-F)
	M08-M07	112.37	$E^{\parallel}(\text{R})$	Libration of (CO_3)
	M06	96.15	$A_2^{\parallel}(\text{I})$	Trans. of (CO_3, K)
	M05-M04	62.63	$E^{\perp}(\text{I+R})$	Trans. of (F), Symm. bending of (Sr-F)
RbSrCO_3F	M15	306.20	$A_2^{\parallel}(\text{I})$	Asymm. str. mode of Sr-F
	M14-M13	162.54	$E^{\perp}(\text{I+R})$	Trans. of CO_3 group, Symm. bending of (Sr-F)
	M12	161.71	$A_2^{\perp}(\text{silent})$	Rotation of CO_3
	M11	131.09	$A_2^{\parallel}(\text{I})$	Trans. of CO_3 group, Asymm. str. of (Sr-F)
	M10-M09	126.58	$E^{\perp}(\text{I+R})$	Symm. bending of (Sr-F)
	M08-M07	118.91	$E^{\parallel}(\text{R})$	Libration of (CO_3)
	M06	99.00	$A_2^{\parallel}(\text{I})$	Trans. of (CO_3, Rb)
	M05-M04	81.32	$E^{\perp}(\text{I+R})$	Trans. of (CO_3, Rb) , Symm. Bending of (Sr-F)
CsPbCO_3F	M15-M14	177.53	$E^{\parallel}(\text{R})$	Libration mode of CO_3
	M13	158.38	$A_2^{\parallel}(\text{I})$	Trans. mode of (CO_3, Cs) + Asymm. str. (Pb-F)
	M12	145.61	$A_2^{\parallel}(\text{I})$	Asymm. str. of (Pb-F)
	M11	106.75	$A_2^{\perp}(\text{Silent})$	Rot. mode of CO_3
	M10-M09	87.26	$E^{\perp}(\text{I+R})$	Trans. of (CO_3, Cs) + Symm. bending of Pb-F
	M08	81.16	$A_2^{\parallel}(\text{I})$	Trans. of (CO_3, Cs) , Asymm. str. (Pb-F)
	M07-M06	65.77	$E^{\perp}(\text{I+R})$	Trans. of Cs, Symm. bending of (Pb-F)
	M05-M04	43.10	$E^{\perp}(\text{I+R})$	Symm. bending of (Pb-F), Trans. of CO_3

are performed in the static approximation, i.e., at $T=0^\circ\text{K}$ and neglecting zero-point vibrational effects, the corresponding Gibb's free energy in this case becomes $G_{stat}(V,P) = E(V) + PV$ which is the enthalpy H of the system. According to quasi-harmonic Debye model the non-equilibrium Gibb's free energy function is given by $G(V,P,T) = E(V) + PV + A_{vib}(\Theta(V), T)$. Where $\Theta(V)$ is the Debye temperature, PV indicates the constant hydrostatic pressure condition and A_{vib}

is vibrational Helmholtz free energy[50]. The heat capacity (C_v), entropy (S_v) and vibrational internal energy (U_{vib}) are calculated using the following relations:

$$C_v = 3nk [4D(\Theta / T) - (3 (\Theta / T) / (e^{(\Theta/T)} - 1))]$$

$$S_v = nk [4D(\Theta / T) - (3 \ln (1 - e^{(\Theta/T)}))]$$

$$U_{vib} = nkT [(9 / 8)(\Theta / T) + (3 D (\Theta / T))]$$

The Debye temperature is the highest temperature that can be achieved due to a single normal mode of a solid. Its magnitude varies from material to material based on the lattice vibrations. It is a fundamental parameter which correlates with many physical properties of solids, such as entropy, specific heat, thermal expansion and thermal conductivity. Since the Debye temperature shows strong temperature dependence, we have calculated this dependence up to the temperature range of 1000 K as shown in Fig 4.4. Entropy is a measure of uncertainty in the energy associated with the random arrangement, thermal motion of the atoms. As the temperature increases the vibrational contribution to the entropy increases and in turn entropy increases. For the presently studied crystals (see Fig 4.4), the plots indicate a slight change in entropy which could be due to the change in atomic arrangements (Wyckoff positions) and with atomic masses. It is observed that CsPb shows higher entropy whereas KCa shows lower entropy response. In case of KSr, RbSr entropy is almost constant. It is well known that, as the temperature rises the contribution of phonons become more and more important and one can calculate the free energy $F = U - TS$, where U is the vibrational internal energy which contains the static energy, phonon contribution and S is the entropy which is completely due to phonon's and it is shown in Fig 4.4. The calculated free energy of all the studied crystals decreases with the increase in temperature. This behaviour is due to the fact that both vibrational internal energy U and entropy S increases with temperature and this leads to decrease in the free energy. The studied systems are found to be thermodynamically stable below 1000 K. We have calculated the coefficient of thermal expansion using the relation. $\alpha = (\gamma C_v) / (B V)$ Where B , V , C_v are the isothermal bulk modulus,

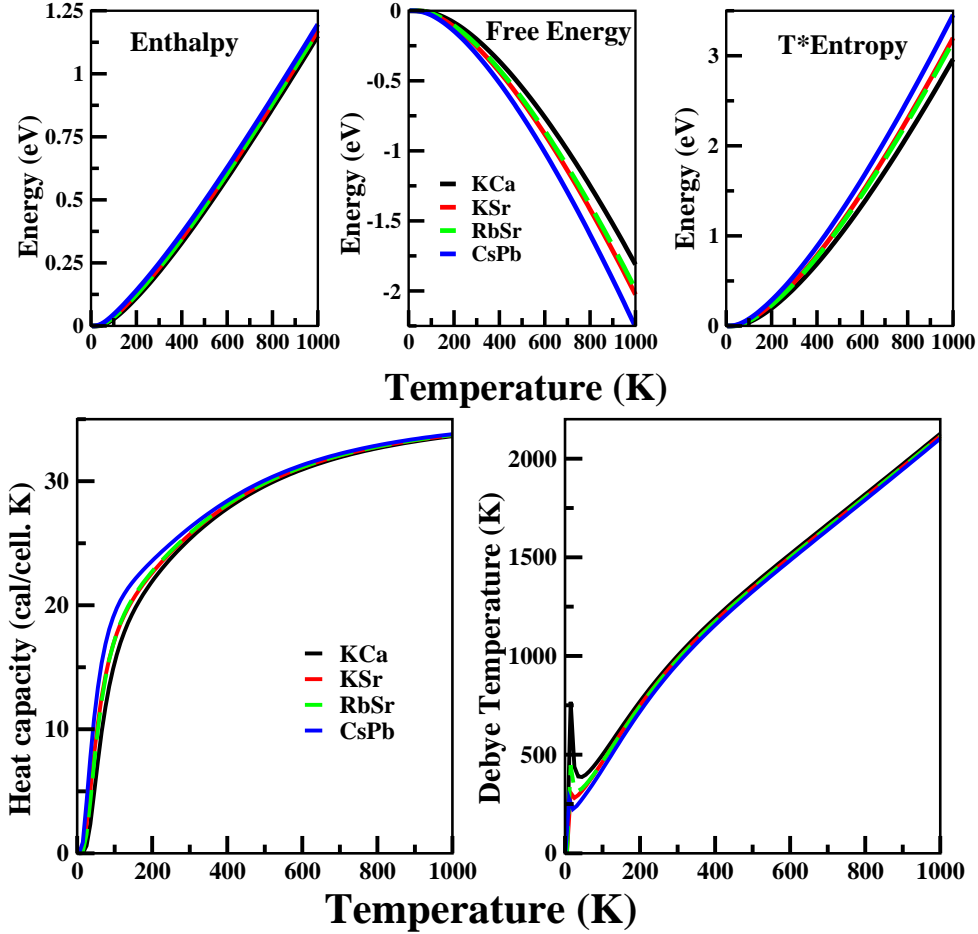


Figure 4.4: Calculated thermodynamic properties enthalpy (H), free energy (F), entropy (S_V), heat capacity (C_V) and Debye temperature $\Theta(V)$ of carbonates at theoretical equilibrium structure up to 1000K temperature.

unit formula volume and specific heat at constant volume respectively and γ is the Gruneisen parameter calculated on the basis of a rigid ion model [51].

The thermal expansion coefficient is proportional to the specific heat and both the properties exhibit the same temperature dependence. The specific heat and thermal expansion coefficient increase as T^3 at low temperatures and gradually approach a linear increase at high temperatures, and then the increasing trend becomes gentler. Specific heat and thermal expansion reach a constant value at high temperature as shown in Fig 4.4, 4.5. It is to be noted from the results that the

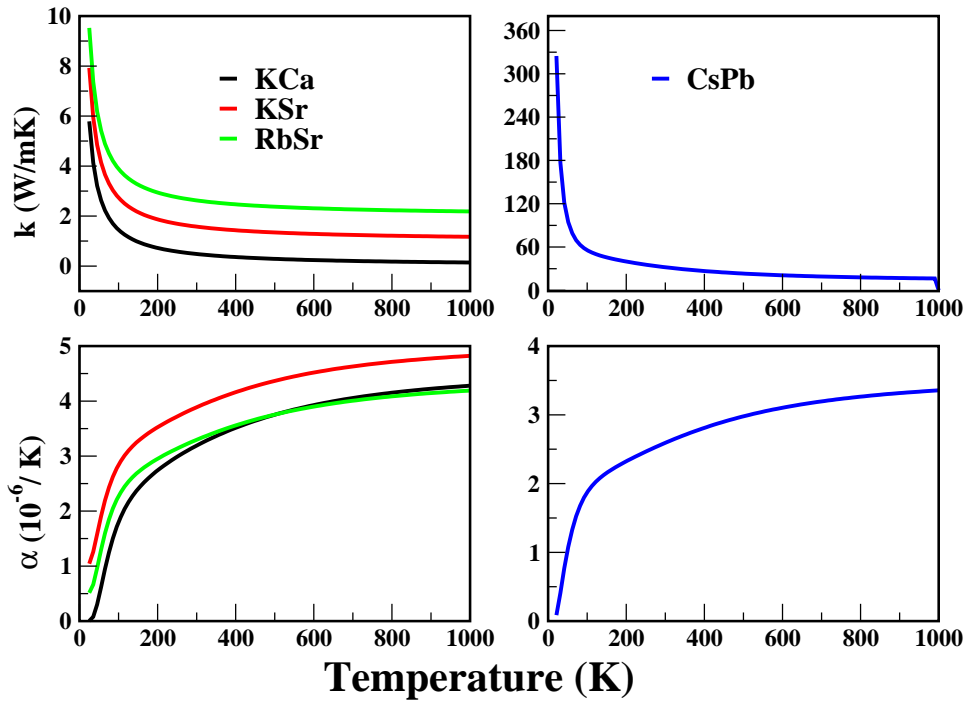


Figure 4.5: Calculated thermal conductivity (k) and thermal expansion (α) coefficients of carbonates at theoretical equilibrium structure. The k , α curves of KSr and RbSr are shifted upward by 1W/mK and $0.5(10^{-6}/\text{K})$ from the preceding curve for clarity.

lead carbonate material has least thermal expansion coefficient $2.577 \cdot 10^{-6}/\text{K}$ than $\alpha\text{-SiO}_2$, LiNbO_3 , CaCO_3 (calcite), ABCO_3F ($A=\text{K, Rb}$; $B=\text{Ca, Sr}$) carbonates as shown in Table 4.12. In comparison with other studied carbonate fluoride crystals, it is observed that the α value decreases with increase of atomic number. This could be due to the strengthened atomic bonds in CsPb material.

Thermal conductivity (k) plays a critical role in controlling the performance and stability of materials and is one of the fundamental and important physical parameters of materials. It is an important parameter in the design of high-power nonlinear optical (NLO) devices such as frequency doublers and optical parametric oscillators (OPO's). On a more fundamental level, the study of the underlying physics of the heat-conduction process has provided a deep and detailed under-

Table 4.12: The calculated thermal conductivities k (W/m K) and thermal expansion coefficients α ($10^{-6}/K$) of carbonate fluorides at room temperature along with other hexagonal NLO materials data

Present		
Material	k	α
CsPbCO ₃ F	32.430	2.577
RbSrCO ₃ F	2.634	2.786
KSrCO ₃ F	1.584	2.877
KCaCO ₃ F	0.488	3.178
Previous[38]		
Ba ₃ B ₆ O ₁₂	4.0, 36.0	1.2, 1.6
α -SiO ₂	12.38,6.88	6.2,10.4
LiNbO ₃	15.4,5.3	5.4, 5.3
CaCO ₃	-3.7, 25.1	4.5,5.4

standing of the nature of lattice vibrations in solids [52]. The thermal conductivity for the present nonlinear optical crystals is calculated using phonon relaxation time method [53]. An important postulate is that; if the material is pure then the term accounting for strong defect scattering will be negligible compared to the term for phonon-phonon scattering so that thermal conductivity

$$k = (K_B^2 / 2 \pi^2 \hbar \nu_s) (\Theta_D / C T)$$

Here ν_s is the mean sound velocity and it can be calculated using following longitudinal(ν_l), transverse wave velocity(ν_t) relations [29]:

$$\nu_l = [(B + (4/3)G)/\rho]^{0.5};$$

$$\nu_t = [G/\rho]^{0.5};$$

$$\text{mean velocity } \nu_s = \nu_m^{-3} = (1/3)(\nu_l^{-3} + 2\nu_t^{-3});$$

The thermal conductivity of the NLO materials were calculated following the work of Callaway and Baeyer [53]. Thermal conductivity results as a function of temperature for CsPb and other carbonate materials is graphically represented in Fig 4.5. It is clear from the plots that, increase in conductivity is rapid initially and become constant at higher temperatures. This effect is more in lead carbonate fluoride than other studied crystals which give a hint about the possible longest

phonon mean free path than in other crystals [38]. Thermal conductivity decreases with temperature due to the fact that the molecular vibrational densities increase with temperature. The obtained 'K' values for KCa, KSr, RbSr and CsPb crystals at room temperatures are 0.0048 W/cm K, 0.0158 W/cm K, 0.0263 W/cm K, 0.032 W/cm K. These values are consistent with the experimental results for other NLO materials [38, 48]. All the obtained values along with known values of hexagonal NLO materials are tabulated in Table 4.12 for better comparison. Importantly, the predicted thermal conductivity of lead material at room temperature is 0.032 W/cm K which is greater than the earlier reported thermal conductivity values for Ba₃B₆O₁₂ which is 0.016 W/cm K [48] and other hexagonal NLO materials [38]. Moreover, it shows the largest 'K' value among all the studied carbonates. This information tells us that CsPb has better durability than BBO and other carbonate materials. Moreover it is well known that, the nonlinear media must have sufficiently high thermal conductivities to get better average output power of the devices. Present thermal conductivity results clearly infer that the lead based carbonate could be the best suited NLO material thereby overtaking the other carbonates and borates. We could not compare our results due to lack of experimental and theoretical data as our work is the first of a kind which calculates these properties of carbonate fluoride crystals. These results could provide necessary input for the design of high-power optical frequency converters in the near future.

4.4 Conclusions

In conclusion, we have studied the effect van der Waals (vdW) interactions on the structural properties of CsPbCO₃F by means of density functional theory. The calculated structural properties using a semi-empirical dispersion correction scheme (PW91 + OBS) to treat the van der Waals interactions are found to be in good agreement with the experimental values which indirectly suggests the im-

portant role of van der Waals forces in this crystal. In addition, we have also calculated the zone centre vibrational frequencies of CsPbCO_3F and ABCO_3F ($A = \text{K, Rb}$; $B = \text{Ca, Sr}$) with a density functional perturbation theory (DFPT) approach and the obtained high frequency modes are in reasonable agreement with the available experimental data. All mode assignments were performed and at least one silent mode was observed in the case of all the studied crystals. This mode arises due to a rotation of CO_3 group and is found to be active only in the hyper-Raman region from group theory analysis. The variations in vibrational mode intensities and optical activity of the studied crystals are broadly analyzed from the obtained Born Effective Charge (BEC) tensor values. We have also calculated the thermodynamic properties such as enthalpy, free energy, entropy, heat capacity, Debye temperature, thermal conductivity and thermal expansion. The room temperature values of heat capacity, thermal expansion and thermal conductivity for all studied NLO materials are different, their overall temperature dependence is very similar. This indicates that all the compounds are characterized by rather similar lattice dynamical and thermal properties. We believe this work sheds light on the (NLO) material CsPbCO_3F as it could be a promising NLO material in near future.

References

- [1] G. Zou, N. Ye, L. Huang and X. Lin, *J. Am. Chem. Soc.*, **133**, 20001 (2011).
- [2] E. Narsimha Rao, S. Appalakondaiah, N. Yedukondalu and G. Vaitheeswaran, *J. Solid State Chem.*, **212**, 171 (2014).
- [3] L. Kang, Z. Lin, J. Qin and C. Chen, *Sci. Rep.*, **3**, 1366 (2013).
- [4] T. T. Tran, P. S. Halasyamani and J. M. Rondinelli, *Inorg. Chem.*, **53**, 6241 (2014).
- [5] D. Khokhlov, *Lead chalcogenides physics and applications*, Volume 18, Taylor & Francis, London (2003).
- [6] J. D. Grice, V. Maisonneuve and M. Leblanc, *Chem. Rev.*, **107**, 114 (2007).
- [7] L. Kang, S. Luo, H. Huang, N. Ye, Z. Lin, J. Qin and C. Chen, *The J. Phys. Chem. C*, **117**, 25684 (2013).
- [8] G. Zou, L. Huang, N. Ye, C. Lin, W. Cheng and H. Huang, *J. Am. Chem. Soc.*, **135**, 18560 (2013).
- [9] W. Voigt, *Ann. Phys. (Leipzig)*, **38**, 573 (1889).
- [10] A. Reuss, *J. Appl. Math. Mech.*, **9**, 49 (1929).
- [11] R. Hill, *Proc. Royal Soc. Lond.*, **A 65**, 350 (1952).
- [12] M. C. Payne, M. P. Teter, D. C. Allan, T. A. Arias and J. D. Joannopoulos, *Rev. Mod. Phys.*, **64**, 1045 (1992).
- [13] M. D. Segall, P. J. D. Lindan, M. J. Probert, C. J. Pickard, P. J. Hasnip, S. J. Clark and M. C. Payne, *J. Phys.:Condens. Matter*, **14**, 2717 (2002).
- [14] D. M. Ceperley and B. J. Alder, *Phys. Rev. Lett.*, **45**, 566 (1980).

-
- [15] J. P. Perdew and A. Zunger, Phys. Rev. B, **23**, 5048 (1981).
- [16] J. P. Perdew and Y. Wang, Phys. Rev. B, **45**, 13244 (1992).
- [17] J. P. Perdew, K. Burke and M. Ernzerhof, Phys. Rev. Lett., **77**, 3865 (1996).
- [18] D. Vanderbilt, Phys. Rev. B, **41**, 7892 (1990).
- [19] T. H. Fischer and J. Almlof, J Phys. Chem., **96**, 9768 (1992).
- [20] F. Ortman, F. Bechstedt and W. G. Schmidt, Phys. Rev. B, **73**, 205101 (2006).
- [21] D. R. Hamann, M. Schl'uter and C. Chiang, Phys. Rev. Lett., **43**, 1494 (1979).
- [22] S. Baroni, S. de Gironcoli, A. Dal Corso and P. Giannozzi, Rev. Mod. Phys., **73**, 515 (2001).
- [23] V. Milman, K. Refson, S. J. Clark, C. J. Pickard, J. R. Yates, S. -P. Gao, P. J. Hasnip, M. I. J. Probert, A. Perlov and M. D. Segall, THEOCHEM, **954**, 22 (2010).
- [24] X. Gonze, Phys. Rev. B, **55**, 10337 (1997).
- [25] E. B. Wilson, J. C. Decius and P. C. Cross, *Molecular Vibrations: the theory of infrared and Raman vibrational spectra*, McGraw-Hill, New York, (1955).
- [26] H. J. Monkhorst and J. D. Pack, Phys. Rev. B, **13**, 5188 (1976).
- [27] S. Grimme, J. Comput. Chem., **27**, 1787 (2006).
- [28] S. Appalakondaiah, G. Vaitheeswaran, S. Lebègue, N. E. Christensen and A. Svane, Phys. Rev. B, **86**, 035105 (2012).
- [29] H. M. Ledbetter, J. Phys. Chem. Ref. Data, **6**, 1181 (1977).

- [30] S. F. Pugh, *Philos. Mag.*, **45**, 823 (1954).
- [31] V. Kanchana, G. Vaitheeswaran, A. Svane and A. Delin, *J. Phys.: Condens. Matter*, **18**, 9615 (2006).
- [32] I. R. Shein and A. L. Ivanovskii, *J. Phys.: Condens. Matter*, **20**, 415218 (2008).
- [33] J. Haines, J. M. Léger and G. Bocquillon, *Ann. Rev. Mater. Res.*, **31**, 1 (2001).
- [34] A. M. Liquori, E. Giglio and L. Mazzarella, *Il Nuovo Cimento B*, **55**, 476 (1971-1996).
- [35] E. S. Fisher; L. C. R. Alfred, *Trans. TMS-AIME*, **242**, 1575 (1968).
- [36] A. Bouhemadou, *Braz. J. Phys.*, **40**, 52 (2010).
- [37] M. Born and K. Huang, *Dynamical Theory of Crystal Lattices*, Oxford University Press, Oxford, Canada, (1998).
- [38] M. Bass, C. DeCusatis, J. Enoch, V. Lakshminarayanan, G. Li, C. MacDonald, V. Mahajan and E.V. Stryland, *Handbook of Optics, 3rd ed., vol. 4*, MGH, Florida, (2009).
- [39] W. Zhong, R. D. King-Smith and D. Vanderbilt, *Phys. Rev. Lett.*, **72**, 3618 (1994).
- [40] P. Ghosez, X. Gonze, P. Lambin and J. P. Michenaud, *Phys. Rev. B*, **51**, 6765 (1995).
- [41] A. Roy, S. Mukherjee, R. Gupta, S. Auluck, R. Prasad and A. Garg, *J. Phys.: Condens. Matter*, **23**, 325902 (2011).
- [42] M. Posternak, R. Resta and A. Baldereschi, *Phys. Rev. B*, **50**, 8911 (1994).

- [43] S. Yip, *Handbook Of Materials Modeling*, Springer, The Netherlands, 195-214 (2005).
- [44] P. Ravindran, R. Vidya, A. Kjekshus, H. Fjellvag and O. Eriksson, *Phys. Rev. B*, **74**, 224412 (2006).
- [45] E. Kroumova, M. I. Aroyo, J. M. Perez-Mato, A. Kirov, C. Capillas, S. Ivantchev and H. Wondratschek, *Phase Transitions*, **76**, 155 (2003).
- [46] J. F. Lin, J. Liu, C. Jacobs and V. B. Prakapenka, *Am. Mineral.*, **97**, 583 (2012).
- [47] N. Buzgar and A. I. Apopei, *Analele Stiintifice Ale Universitatii, Al. I. Cuza Iasi Geologie*, **55**, 97 (2009).
- [48] J. Donald Beasley, *Appl. opt.*, **33**, 1000 (1994).
- [49] H. Wu, H. Yu, Z. Yang, J. Han, K. Wu and S. Pan, *J Materiomics*, **1**, 221 (2015).
- [50] M. A. Blanco, E. Francisco and V. Lua \tilde{A} \pm a, *Comput. Phys. Commun*, **158**, 57 (2004).
- [51] A. Parveen and N. K. Gaur, *Thermochim. Acta*, **566**, 203 (2013).
- [52] D.T. Morelli and G.A. Slack, *High Thermal Conductivity Materials*, ed. S.L. Shinde and J.S. Goela, Springer, New York, ch. 2, pp. 37-68 (2006).
- [53] J. Callaway and H. C. von Baeyer, *Phys. Rev.*, **120**, 1149 (1960).

Role of spin-orbit interaction on optical response of CsPbCO_3F

In this chapter, we explore the effect of spin-orbit interaction (SOI) on the electronic and optical properties of CsPbCO_3F using full potential linear augmented plane wave method. It is well known that nonlinear optical properties are very sensitive to the energy gap [1–6]. Therefore, to obtain accurate results, the calculations are done with TB-mBJ exchange-correlation potential. After the inclusion of SOI, the calculated TB-mBJ band gap of 5.58 eV reduces to 4.45 eV in agreement with the experimental value. This is due to the splitting of Pb p-states. Importantly, the occurrence of band gap along H-A direction (indirect) transforms to H-H (direct) high symmetry points/ direction in the first Brillouin zone. We noticed a large anisotropy in the calculated complex dielectric function, absorption and refractive index spectra. The calculated static birefringence of 0.1049 and 0.1057 (with SOI) is found to be higher than the other carbonate fluorides. From the Born effective charge (BEC) analysis, we notice that Cs atom shows a negative contribution to birefringence whereas Pb, C, F atoms show a positive contribution. Overall, our results are in agreement with experiments and it is obvious from the present study that CsPbCO_3F is a direct band gap, large second harmonic generation and good phase matchable NLO crystal in the ultraviolet region.

5.1 Introduction

From the electronic properties point of view, a better UV-NLO crystal for practical applications is expected to have larger nonlinear coefficients ($> d_{36}$ of KDP), wide band gap (> 6.2 eV) and moderate birefringence (0.07) with larger laser damage threshold value (> 5 GW/cm²) [8]. The materials with P-O [12](KH₂PO₄), I-O [11] (LiIO₃), Nb-O [9] (LiNbO₃), B-O [10] (β -BaB₂O₄, LiB₃O₅, CsB₃O₅, KBe₂BO₃F₂, Sr₂Be₂BO₇, CsLiB₆O₁₀) bonds are extensively studied for solving the purpose [7]. But these materials possess their own drawbacks for generating a coherent light such as narrow band width, improved beam quality, tunability and relative ease of handling [7].

For the past five years experimental and theoretical investigations [13–23, 25–28, 45] suggest that novel carbonate fluorides (C-O) are promising polycrystalline NLO crystals for the generation of coherent light in UV and deep-UV regions. Since 2011, the synthesis of noncentrosymmetric carbonate fluoride materials got accelerated to meet the scientific and industrial needs. During last five years, a few tens of carbonates (centrosymmetric and noncentrosymmetric) are synthesized and their nonlinear optical responses to the applied external electric field (1064 nm) are reported in the literature. The novel CO₃F based NLO crystals reported till date are ABCO₃F (A=K, Rb, Cs; B=Ca, Sr, Ba) [13], CsPbCO₃F [14, 15], RbPbCO₃F [15], ATCO₃F (A=K, Rb; B=Zn, Cd) [16], RbMgCO₃F [17], K₂Pb₃(CO₃)₃F₂ [18], KCdCO₃F [18], Ca₂Na₃(CO₃)₃F [19], MBeCO₃F [20], MAlCO₃F₂ (M=Li, Na, K, Rb, Cs) [20], KPb₂(CO₃)₂F [21], K_{2.70}Pb_{5.15}(CO₃)₅F₃ [21], Cs₃Pb₂(CO₃)₃I [22], KBa₂(CO₃)₂F [22], RbBa₂(CO₃)₂F [22], CsSrCO₃F [23], Na₄Cd₃(CO₃)₄(OH)₂ [25], ACdCO₃F (A = K and Rb) [26]. Some carbonate crystals without fluorine have also been reported such as Na₄La₂(CO₃)₅ [27], CsNa₅Ca₅(CO₃)₈ [27], Pb₇O(OH)₃(CO₃)₃(BO₃) [45]. Among all these reported carbonate fluorides, powder lead carbonate fluoride is found to show the largest SHG intensity ($13.6 \times d_{36}$ (0.39 pm/V) of KDP, $4 \times$ KSrCO₃F) [14]. All other

crystals show 1-5 times increase in the SHG coefficients with respect to d_{36} of KDP crystal.

It is also important to notice from the literature that researchers are trying to use alkaline and alkaline-earth metal ions to eliminate the negative influence of d-d, f-f electronic transitions to the band gap [20] of carbonate fluorides. In addition, fluorine atoms large electro-negativity and its presence in carbonate fluorides is found to be useful to produce a wide band gap, layered topology [20]. The absorption spectra studies and powder SHG measurements of carbonate fluorides also reveal that, these materials possess wide band gaps above 6.0 eV, absorption edge (below 200 nm). These peculiar properties confirm the importance of carbonates in nonlinear optics for UV light generation. In the process of innovation, CsPbCO₃F is a recently synthesized optically active noncentrosymmetric crystal. Even though it possesses a smaller band gap (4.1 eV) than other carbonate crystals, it has the largest SHG coefficient (13.4 times of KH₂PO₄) among the carbonates. In addition, it is transparent over near-UV to middle-IR region [14]. By knowing the uniqueness of this NLO crystal, we have reported a detailed analysis of the structural, mechanical, vibrational and thermodynamic properties in our previous work [28]. Our analysis revealed the soft (bulk modulus (B) = 41 GPa) and ductile (B/ Shear modulus(G) is > 1.75) nature of CsPbCO₃F with a high thermal conductivity (32.430 W m⁻¹ K⁻¹) [28]. We further noticed the necessity to explore electronic and optical properties of CsPbCO₃F in detail. It is important to synthesize this crystal in larger size (few centimeters) and to alter the band gap, reported preliminary experimental data is not sufficient alone. In the present work, we have focused on the qualitative analysis of electronic, linear and nonlinear optical properties of this novel material. Even though there are few theoretical reports on electronic band structure calculations in the literature, to the best of our knowledge the role of SOI (due to the presence of Pb & Cs) on various optoelectronic properties has not been studied. In general for second-row transition metals and heavier elements, the role SOI is not negligible [29].

Hence in this chapter, we report the electronic, linear optical properties and birefringence of CsPbCO₃F by taking SOI into account. The experimental crystal structure of CsPbCO₃F is shown in Fig 5.1 along with the iso-structural compounds RbSrCO₃F, KCaCO₃F, KSrCO₃F for comparison. Computational techniques utilized for the present calculations are presented in section 5.2. In results and discussions (section 5.3), we discuss the effect of SOI on the electronic band structure, density of states and on the linear optical properties such as real and imaginary parts of the complex dielectric function, absorption spectra, refractive index and birefringence. Finally, the conclusions are given in section 5.4.

5.2 Calculation methods

For the present computational study, we have considered the experimental crystal parameters [14] as reported by Zou et al. CsPbCO₃F crystallizes in P $\bar{6}$ m2 (hexagonal) noncentrosymmetric space group, with Z = 1 formula unit per unit cell having volume(v) of 128.44 Å³. The Wyckoff positions of atoms with occupancy 1 are as follows: Cs (0 0 0), C (0.3333 0.6667 0.5), F (0.6667 0.3333 0), Pb (0.6667 0.3333 0.5), O (0.1961 0.392 0.5). We have used the full-potential linearized augmented plane wave (FP-LAPW) and local orbitals method through density functional theory approach [30]. Here, the Kohn-Sham equations are solved by expanding the wave functions in spherical harmonics form inside the atom spheres. Planewave expansion is used in the interstitial regions of atoms inside the unit cell. We have used lmax = 10 for angular momentum expansion and $K_{max} \times R_{MT} = 7$ as a plane wave cut-off with 1000 k points to achieve the self-consistency. Here R_{MT} is the average muffin-tin (MT) radius and K_{max} is the wave function cut-off. The muffin-tin (MT) radii for different atoms are taken as 2.5 atomic units (a.u.) for Pb, 2.0 a.u. for Cs, 1.2 a.u. for O, 1.8 a.u. for F and 1.1 a.u. for C atom. The energy between successive iterations is converged to 0.0001 Ry and forces are minimized to 1 mRy/bohr. The Monkhorst and Pack (MP) technique is used for Brillouin

zone integrations. We have used Perdew-Burke-Ernzerhof (PBE [36], PBEsol [37]) and Tran-Blaha modified Becke-Johnson approach (TB-mBJ) [31] as an exchange-correlation functional to extract the electronic band structures. A dense k-mesh with 1500 k-points was used in the first Brillouin zone to calculate the linear optical properties. To treat the interactions of heavier elements like Pb and Cs one needs to consider the SOI during the calculations [32]. Therefore, we have performed electronic band structures, optical property calculations with and without SOI. In WIEN2k, spin-orbit (SO) effects are included via second variational procedure to calculate the eigenvalues, eigenvectors [33]. We have used the second variation energy cut off as 10.0 Ry. The optical properties are calculated using the optics package in WIEN2k.

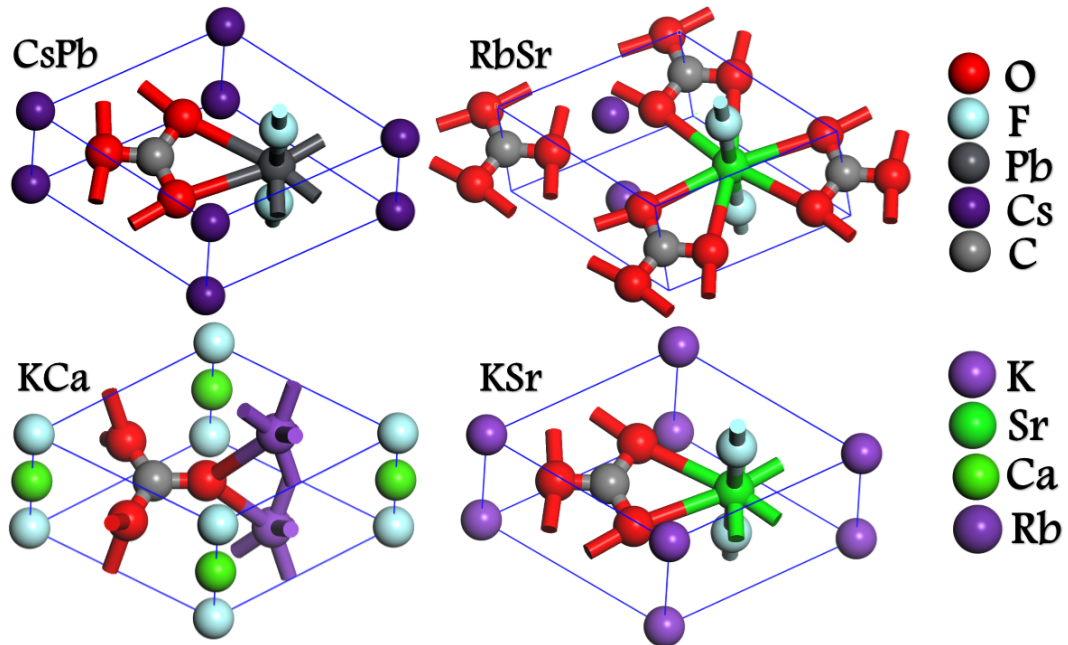


Figure 5.1: Experimental crystal structures of CsPbCO₃F, RbSrCO₃F, KCaCO₃F, KSrCO₃F.

5.3 Results and discussion

5.3.1 Electronic band structure and density of states (DOS)

It is very important to understand the bonding, optical transparency region of an NLO material correctly by means of predicting the exact energy band gap. Since CsPbCO₃F is a recently synthesized carbonate fluoride crystal, there are very few reports available in the literature for the electronic properties which explain the fundamental structure-property co-relationship. The CsPbCO₃F is a layered, phase matchable hexagonal crystal with lattice parameters $a=5.3888$ Å and $c=5.1071$ Å [14]. For the first time, Zou's group reported the experimental band gap of CsPbCO₃F from UV-vis diffuse reflectance spectra as 4.15 eV. They have also reported a theoretical band gap (using PBE functional) of 3.35 eV using the CASTEP [14]. This deviation was obtained due to the fact that GGA normally underestimates the band gap by around 50%. Later, Thao Tran's group also reported the band gap of CsPbCO₃F crystal as 3.31 eV by using PBEsol functional as implemented in total energy code VASP [8]. Even though there are differences in the CsPbCO₃F crystal structures reported by Zou and Thao Tran, it possesses similar band gap difference when compared with the experimental value. More recently Qun Jing et al., reported the theoretical optical band gap as 3.43 eV, 4.0 eV by using PBE and modified Becke-Johnson (mBJ) methods as implemented in FP-LAPW [34]. In this work, optical properties are calculated with PBE functional after adding the scissors correction. Moreover, the mBJ optical band gap was obtained by adjusting the c -parameter as 1.2, which is a relatively expensive calculation compared to the default TB-mBJ functional. Overall, all the theoretically reported values so far are obtained without considering the effect of SOI. Our calculations try to address this issue.

We have considered the experimental crystal structure reported by Zou et al and minimized total energies and forces. Initially, we performed the electronic band gap calculations with PBE [36], PBEsol [37] and TB-mBJ [31] functional

Table 5.1: Calculated energy band gaps of CsPbCO₃F without and with inclusion of SOI at experimental volume. Results are compared with previously reported data.

Functional	Present		Previous
	Without	With	Without
PBE	3.59	3.03	3.35[14], 3.43[34]
PBEsol	3.48	2.94	3.31[15]
TB-mBJ	5.58	4.45	4.0[34]
Experiment	-	-	4.15[14], 4.1[15]

using FP-LAPW method. Due to the presence of heavier elements like Pb and Cs, we have incorporated the SOI [35].

The obtained band gap values along with previously reported theoretical and experimental results are presented in Table 5.1. The results obtained without inclusion of spin-orbit effects with PBE (3.59 eV), PBEsol (3.48 eV) are good in agreement with the previously reported values [14, 15, 31]. The improved band gap is obtained with default TB-mBJ functional (5.58 eV). However, all these values deviate from the experimental value ~ 4.1 eV. Whereas, after SOI is taken into consideration, we found considerable reduction in the band gap. The gap values are 3.03 eV (PBE), 2.94 eV (PBEsol), and 4.45 eV (default mBJ). It is clear from the calculations that, TB-mBJ functional with inclusion of SOI, gives a band gap value that is in good agreement with the experimental data (4.15 eV [14], 4.1 eV [15]). It is clear from Table 5.1 that, the differences in the predicted band gaps before and after inclusion of spin-orbit effects are as follows: with PBE, PBEsol: ~ 0.5 eV; with TB-mBJ: ~ 1.0 eV. This indicates that treating SOI with mBJ functional is more efficient than other functionals in the present case. This change can be attributed to the limitations of PBE & PBEsol and improved performance of the TB-mBJ functionals [38].

We have calculated the band structure along symmetry directions in the first Brillouin zone with/without SOI and are shown in Fig 5.2. Results show a considerable splitting in the energy levels both in the valence band (in -5 eV to -10 eV;

-15 eV to -17.5 eV regions) and in the conduction band (in 5 eV to 10 eV region). These regions are shown in Fig 5.2 separately. The 1 eV downshift of energy bands in bottom of conduction band towards the Fermi level are seen clearly. Importantly, after inclusion of SOI, the band gap which occurs in the H-A direction is transformed to the H high symmetry point i.e. indirect to direct band gap. It is well known that indirect band gap materials are inefficient in emitting light.

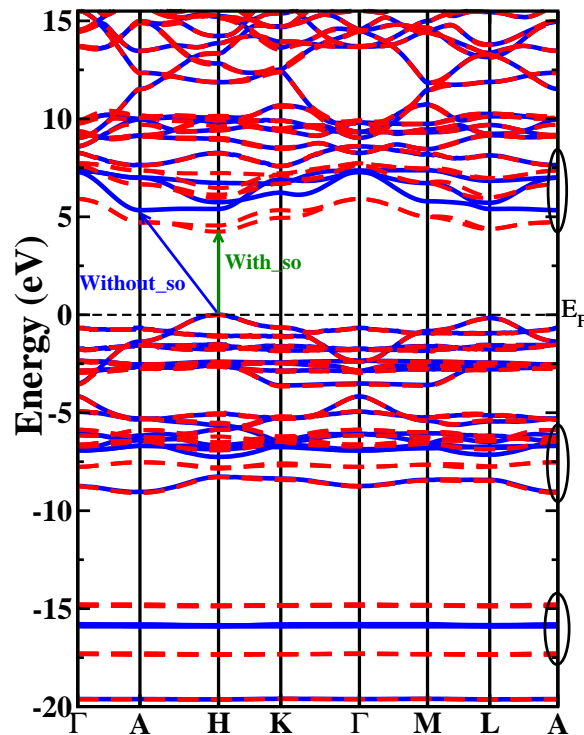


Figure 5.2: Calculated electronic band structure with and without spin-orbit interaction effects of CsPbCO₃F at experimental crystal structure volume.

In order to understand the individual atomic contribution to the splitting of energy levels, we have calculated the total and partial density of states (DOS) with/without SOI at TB-mBJ level. Results are shown in Fig 5.4. It is clear from the plots that, top of the valence band is dominated by Pb-s, F-p and O-p states before and after inclusion of SOI. The F-s, F-p states are dominated in the bottom of the conduction band before inclusion of SO effects, while F-p, F-s states are

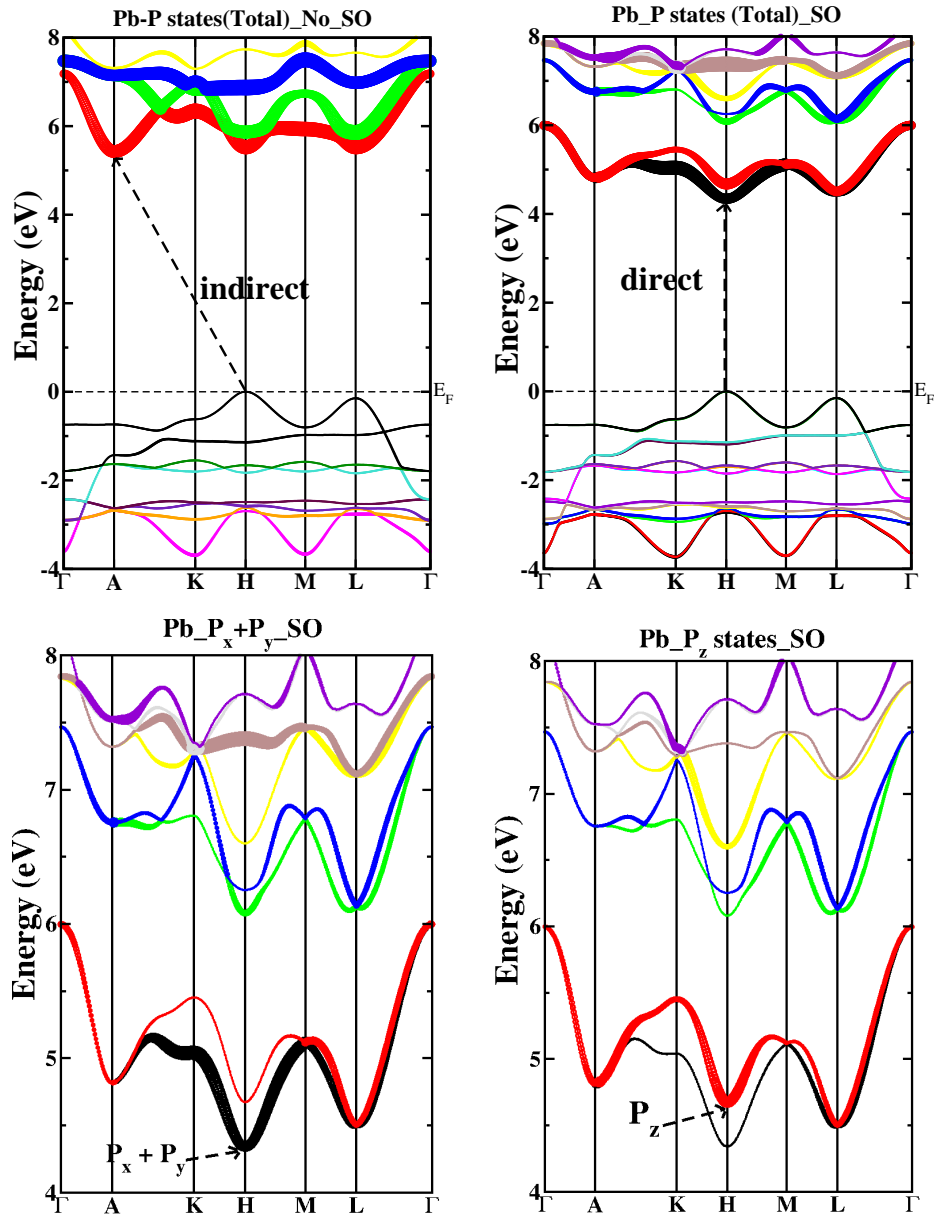


Figure 5.3: Calculated partial electronic band structure with and without spin-orbit interaction effects of CsPbCO₃F at experimental crystal structure volume.

dominated in bottom of the conduction band with SOI. It is also found from the Fig 5.4. that, the p-states corresponding to lead atom are shifted downwards by

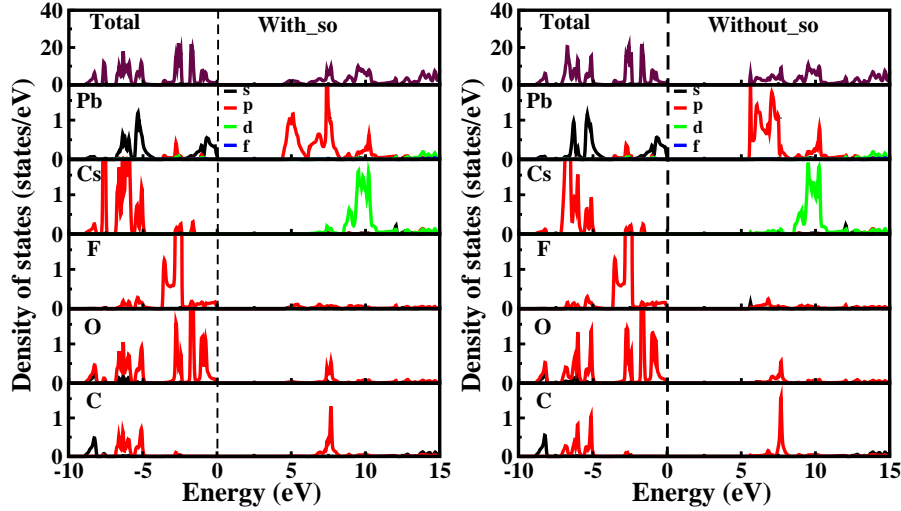


Figure 5.4: Calculated DOS with and without spin-orbit interaction effects of CsPbCO_3F at experimental crystal structure volume.

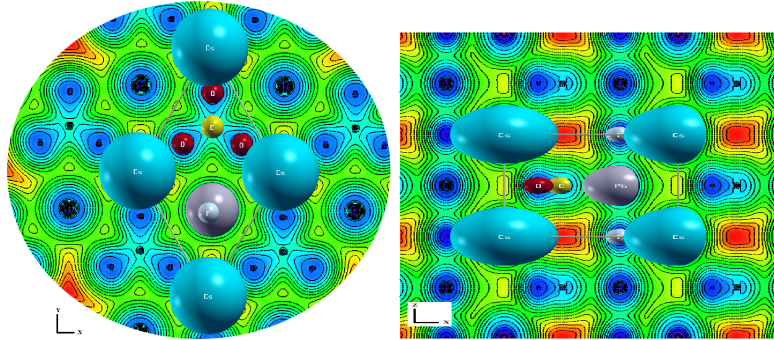


Figure 5.5: Charge density difference plots of CsPbCO_3F along $[1\ 1\ 0]$ and $[1\ 0\ 1]$ planes from left to right.

1 eV to the bottom of the conduction band whereas no changes were observed in the top of valence band near the Fermi level. We have also noticed from the partial DOS (PDOS) plots that, there exist a strong covalency between carbon and oxygen atoms in CO_3 group. Ionic bonding is also observed between Pb & F, Cs; between Pb & CO_3 group. The same is observed from charge density plots plotted in xy and yz planes shown in Fig 5.5. The charge sharing between carbon and oxygen atom's; Pb and F are found to form a dumbbell shape. The charge

around Cs atom is spread in spherical shape which confirms the ionic bonding. For further understanding about lead atomic orbital contribution to the band structure around Fermi level, we have performed the fat-band analysis. Since the effect of Pb-p states is more crucial in this compound, we have plotted the Pb-total, p($p_x + p_y$, p_z) orbitals contributions in Fig 5.3. Here upper part Fig 5.3 shows the clear contribution and splitting of lead p-total states before and after inclusion of SOI. In order to know about the details of the two downward shifted fat bands in the conduction band (see Fig 5.3), we have plotted the partial Pb-p states contribution separately. The lower part of Fig 5.3 shows the $p_x + p_y$ states, p_z states contribution to the energy band structure. It is clear from these figures that, the bottom of the conduction band is occupied by $p_x + p_y$ states but not from p_z states. The indirect to direct band gap transition is arising due to $p_x + p_y$ states alone and it can be observed only after the spin-orbit effects taken in to account.

5.3.2 Linear optical properties and birefringence

Till now there are no detailed experimental or theoretical reports available in the literature on linear optical properties of CsPbCO₃F. In this section, we report calculations of the linear optical properties with/without SOI along with TB-mBJ. As the studied compound crystallizes in hexagonal crystal structure, there are two possible non-zero components of the dielectric tensor along [100] and [001] directions.

The calculated complex dielectric function (real and imaginary parts) of lead carbonate with/without SO effect are shown in Fig 5.6. The $\epsilon_1(\omega)$ is shown in Fig 5.6(a, b, c) and $\epsilon_2(\omega)$ is plotted in Fig 5.6(d, e, f). Here, Fig 5.6(b, e) shows the $\epsilon_1(\omega)$, $\epsilon_2(\omega)$ before SO effects and Fig 5.6(c, f) shows the results after SO inclusion. For better visualization, we have zoomed and plotted the real and imaginary parts of complex the dielectric function on top of other in Fig 5.6(a, d). It can be seen from the plots that, CsPbCO₃F possesses a large anisotropy in dielectric constants along [1 0 0] and [0 0 1] directions. Further observations on the spreading of

dielectric spectra with respect to energy (eV) lead to following important conclusions. Firstly, the spectra obtained before SO effects inclusion infers that: (1) the high intensity peaks of ϵ_{xx} are occurring at energies (eV) 6, 6.5, 9.2, 7.9, 8.5, 11.11, 12.0, 13.5 respectively. A dip is observed at 9.5 eV with a magnitude of -1.47 for ϵ_{xx} . (2) For ϵ_{zz} high intensity peaks are occurring at energies (eV) 5.6, 8.2, 6.5, 11, 11.7, 10.0, 9.5, 12.5 respectively. (3) Overall, up to 7.25 eV ϵ_{xx} is dominant; from 7.25 to 8.25 eV ϵ_{zz} is dominant; from 8.25 to 9.25 eV ϵ_{xx} is dominant, after that ϵ_{zz} shows dominant nature. Secondly, the spectra after SO effects inclusion shows: (1) ϵ_{xx} are occurring at energies (eV) about 5.0, 5.7, 7.2, 9.0, 8.1, 11.6, 11.1, 10.5. The dip of ϵ_{xx} is occurring at 9.5 eV with magnitude -1.3. (2) ϵ_{zz} high intensity peaks are occurring at energies (eV) about 4.9, 5.9, 7.5, 6.3, 8.7, 11, 10.5, 11.7, 12.5. (3) Up to 9 eV ϵ_{xx} is dominant and after that ϵ_{zz} is dominant. In conclusion, after SOI is taken into account, the ϵ_{xx} component is showing significantly higher value than ϵ_{zz} in the lower energy regions, whereas the mixed behaviour of ϵ_{xx} , ϵ_{zz} was observed without SOI inclusion. Thus, these differences in findings of dielectric constants confirm the crucial role of SO effects in the optical properties of CsPbCO₃F. For further analysis of possible optical transitions, the maximum intensity peaks in imaginary part of dielectric function plot (see Fig 5.6(e, f)) are labelled as A, B, C, D along X-direction and P, Q, R, S along Z-direction respectively. The positions of these peaks along two crystallographic directions [1 0 0], [0 0 1] are tabulated in Table 5.2. From this table it is clear that, after inclusion of SOI, all the peaks show a considerable red shift. Similarly, other linear optical properties such as absorption spectra ($\alpha(\omega)$) and refractive indices ($n(\omega)$) spectra are calculated and shown in Fig 5.7. The corresponding static values of dielectric constants, absorption coefficients, ordinary (n_0) and extraordinary (n_e) refractive indices, birefringence ($n_e - n_0$) values are shown in Table 5.3. Our results show that all the linear optical spectra were red shifted with a slight intensity variations.

For a deeper level of understanding of the optical response of CsPbCO₃F, we have analyzed the possible optical transitions from the valence band to the con-

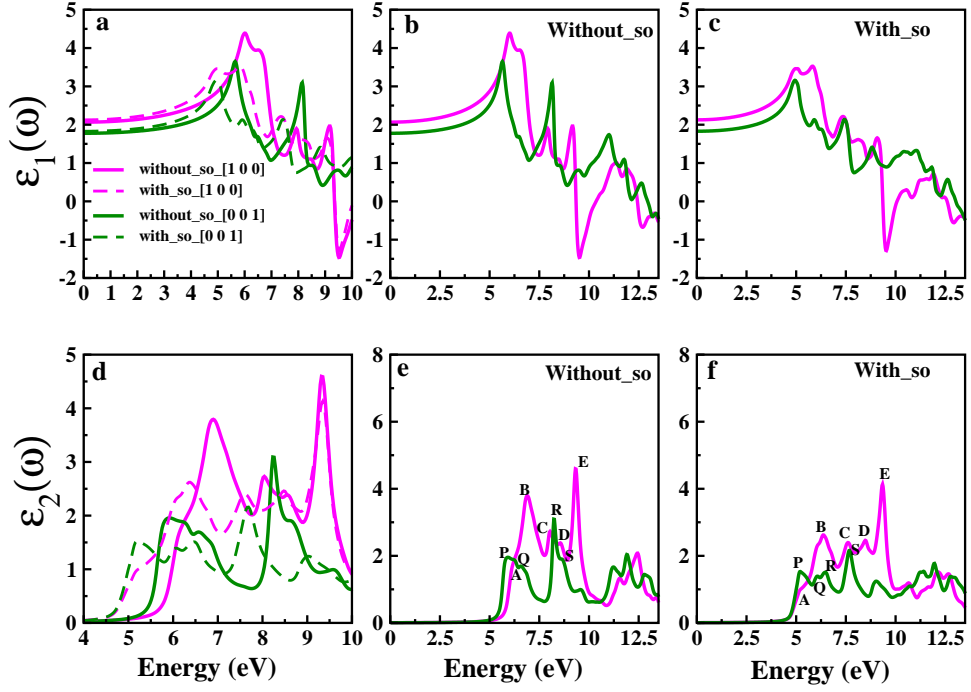


Figure 5.6: Calculated real and imaginary parts of complex dielectric function with and without SOI effects of CsPbCO₃F at experimental crystal structure volume.

Table 5.2: The optical transitions of CsPbCO₃F before and after inclusion of spin-orbit interactions observed from imaginary part of dielectric function and TB-mBJ band structure

Direction	[1 0 0]				[0 0 1]			
Peak	A	B	C	D	P	Q	R	S
before-so	6.3	6.9	8.0	8.5	5.9	6.6	8.2	8.6
after-so	5.2	6.4	7.6	8.5	5.2	6.0	6.5	7.7

Table 5.3: Linear optical properties such as absorption coefficient ($\times 10^4 \text{ cm}^{-1}$), refractive indices and birefringence of KCaCO₃F, KSrCO₃F and RbSrCO₃F

	$\epsilon_1^{[100]}(\omega)$	$\epsilon_1^{[001]}(\omega)$	$\alpha^{[100]}(\omega)$	$\alpha^{[001]}(\omega)$	n_o	n_e	$\Delta n (n_e - n_o)$
before-so	2.12	1.82	73.16	40.8	1.43759	1.33270	0.10489
after-so	2.06	1.77	50.81	25.03	1.45832	1.35263	0.10569

duction band states by utilizing PDOS information (see Fig 5.4). It is clear from the PDOS plots that, the Pb(s), O(s), F(p) states are dominated in the VBM (-1

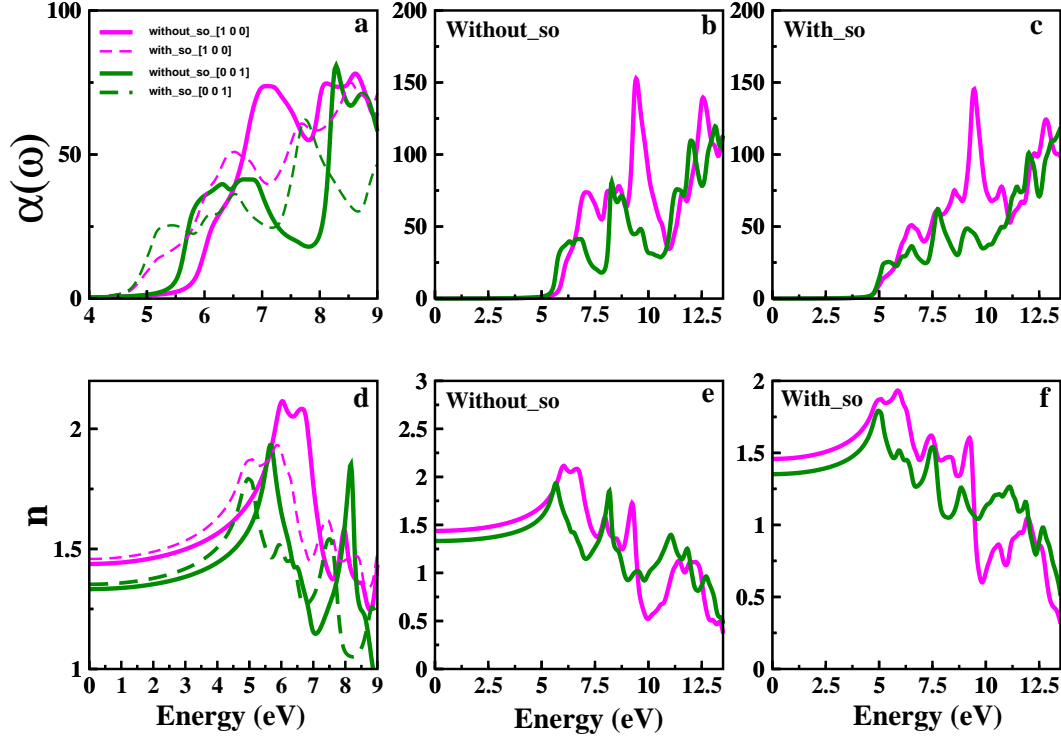


Figure 5.7: Calculated refractive index and absorption spectra with and without spin-orbit interaction effects of CsPbCO_3F at experimental crystal structure volume.

eV to Fermi level) and these states are unaffected with inclusion of SOI. In the deep valence band below -2 eV, spreading in the DOS peaks of Pb(p), Cs(d), F(p), O(p), C(p) states clearly seen, whereas in conduction band minimum, before including spin-orbit effects the Pb(p), Cs(d,p), F(s,p), C(p,s), O(s,p) states are dominant. After the inclusion of SOI, a clear difference in the dispersion of DOS in the Pb(p), F(p,s), O(p), C(s, p), Cs(d,p) states is observed. It is also noticed that all the states are red shifted in bottom of conduction band by approximately 1 eV as follows: O(1.15 eV), Pb(1.14 eV), Cs(1.02 eV), F(0.91 eV), C(0.79 eV). Hence these observed differences in the PDOS will lead to changes in the optical properties. Based on the selection rules, we have explained the possible optical transitions (from valence band to conduction band) for the high intensity peaks in [1 0 0] crystallographic direction. The results before and after inclusion of SOI

are tabulated in Table 5.4. Because of the changes in DOS spreading, the optical transitions also showed considerable variations in results. Especially in case of absorption peak's A–B, the Pb(s) to C(p) states transition is possible before inclusion of SOI effects, but later this transition could not come into picture. This clearly shows the role of SOI in explaining the optical transitions of the lead carbonate NLO material in UV region. Our further optical transition analysis of other high intensity absorption peaks are given in Table 5.4. Similar kind of effects can possibly occur in [0 0 1] crystallographic direction also.

Table 5.4: The optical transitions of CsPbCO₃F derived from top of valence band to conduction band observed from imaginary part of dielectric function along [1 0 0]

Before-so	Peaks	Transitions
	A	Pb(s) to F(p)/O(p)/C(p)/Cs(p); O(P) to F(s)/Cs(d)/Cs(s)/Pb(s); F(P) to O(s)/Cs(d)/Cs(s)/Pb(s);
	B	Pb(s) to F(p)/C(p)/O(p)/Cs(p); O(P) to Cs(d)/F(s)/Cs(s)/Pb(d); F(P) to Cs(d)/O(s)/Cs(s)/Pb(d);
	C	Pb(s) to O(p)/C(p)/F(p)/Cs(p); O(P) to F(s)/Cs(s)/Pb(d)/Cs(d); F(P) to Cs(d)/Pb(d)/Cs(s);
	D	Pb(s) to O(p)/C(p)/F(p)/Cs(p); O(P) to Cs(d)/Cs(s)/F(s)/O(s)/Pb(s); F(P) to Cs(d)/Cs(s)/O(s)/Pb(d);
After-so	Peaks	Transitions
	A	Pb(s) to F(p)/O(p)/Cs(p); O(P) to F(s)/Pb(s)/Cs(d); F(P) to O(s)/Pb(s)/Cs(d);
	B	Pb(s) to F(p)/O(p)/Cs(p); O(P) to F(s)/Cs(d); F(P) to O(s)/Cs(d);
	C	Pb(s) to F(p)/C(p)/O(p)/Cs(p); O(P) to Cs(d)/Cs(s)/Pb(d); F(P) to Cs(d)/Cs(s)/Pb(d);
	D	Pb(s) to F(p)/C(p)/O(p)/Cs(p); O(P) to Cs(d)/F(s)/Cs(s)/Pb(d); F(P) to Cs(d)/O(s)/Cs(s)/Pb(d);

The values of ordinary and extraordinary refractive indices show an increment of 0.0246 in magnitude after inclusion of SOI. Further, the birefringence values at static, 1064 nm (1.165 eV), 532 nm (2.33 eV) are tabulated in Table 5.5 for future reference. The results of all the studied crystals shows a linear increment in birefringence values starting from static \rightarrow 1064 nm \rightarrow 532 nm. Overall, it is clear from the results that CsPbCO₃F possesses the largest birefringence at TB-mBJ level among all the studied carbonate fluoride crystals. There are slight differences between birefringence values reported by Qun Jing [34] et al at GGA-PBE level using CASTEP and our calculated results of CsPbCO₃F. The reason for this deviation comes from the accuracy of TB-mBJ functional in predicting the exact band gap with inclusion of SOI in the present case. Besides this expected discrepancy in the results, both works end up in proposing lead carbonate as a

unique material among the reported carbonate NLO materials family till date. In order to explore the reasons behind the changes in the birefringence (Δn) values of CsPbCO_3F , we have calculated the Δn from 300 nm to 1200 nm and this is shown in Fig 5.8. We find that birefringence of CsPbCO_3F is higher than other iso-structural carbonate compounds. To explore more about the birefringence, we have calculated the change in the Born effective charge values along two crystallographic directions [39]. The results reveal that the Cs and Rb are negatively contributing to the birefringence, where Pb, C, and F shows positive contribution. Perhaps one can clearly see the role of SOI on Δn of lead carbonate fluoride also from Fig 5.8. The reduction in the refractive indices(see Fig 5.7(b)) along $[1\ 0\ 0]$, $[0\ 0\ 1]$ directions and birefringence values after inclusion of SO effects can be attributed to differences in the photo induced inter-band transitions.

Table 5.5: The birefringence of CsPbCO_3F before and after inclusion of spin-orbit interactions obtained from imaginary part of dielectric function at TB-mBJ level. For comparison, birefringence of ABCO_3F (A=K, Rb; B=Ca, Sr) also calculated using our previous work[39]

@	before	after	RbSr	KSr	KCa
Static	0.1048	0.1056	0.0887	0.0921	0.0966
1064 nm	0.1063	0.1073	0.0901	0.0934	0.0981
532 nm	0.1108	0.1123	0.0942	0.0976	0.1028

Table 5.6: The change in Born Effective charges (Δq) along x and z directions of different metal atoms of CsPbCO_3F , ABCO_3F (A=K, Rb; B=Ca, Sr)[28]

Atom	Δq						
Cs	-0.28	Rb	-0.2	K	-0.11	K	-0.15
Pb	0.46	Sr	0.1	Sr	0.07	Ca	0.11
C	2.82	C	2.91	C	2.76	C	2.72
F	2.03	F	0.78	F	0.9	F	0.79

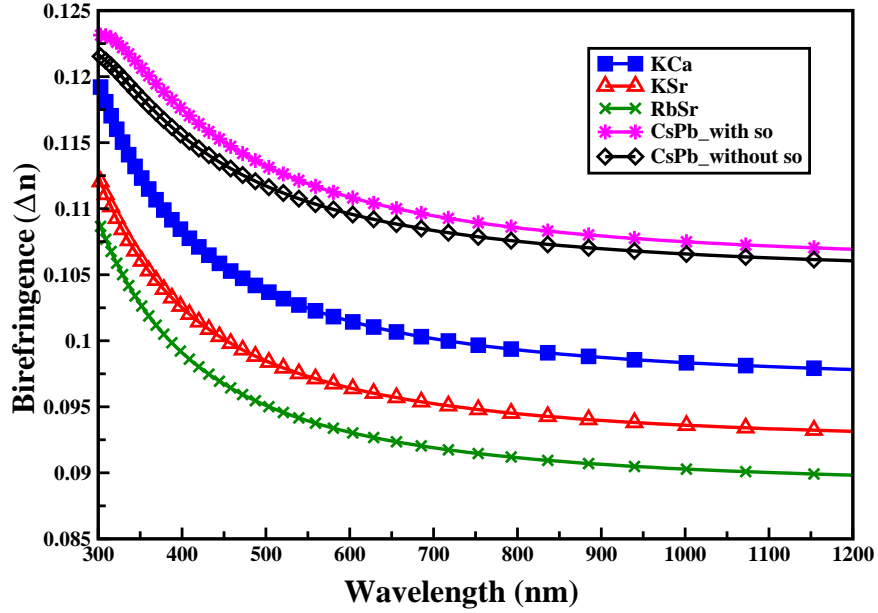


Figure 5.8: Calculated Birefringence of CsPbCO₃F with spin-orbit interaction effects, ABCO₃F (A = K, Rb; B = Ca, Sr) at experimental crystal structure volume.

5.4 Conclusions

The effect of SOI on the optoelectronic, linear optical properties and birefringence of CsPbCO₃F are thoroughly investigated by means of density functional theory. The electronic band gaps calculated with inclusion of SOI effects at TB-mBJ level of accuracy are good in agreement with the experimental reported results. The band gap results without SO effects are in good agreement with the previously reported works. The electronic band structure analysis reveals that CsPbCO₃F is direct band gap NLO material but not an indirect one as is the case when SOI is neglected. The band gap is occurring at H high symmetry point in the first Brillouin zone. The analysis of individual atomic contribution to the band structure reveals the fact that, band gap reduction of 1.1 eV of CsPbCO₃F is mainly occurring due to the Pb atom p-states splitting near the Fermi level. More splitting of energy levels are observed in valence and conduction bands because of SOI effects. Similar shifts are observed in the calculated PDOS plots

also. Our further analysis of the charge density plots along $[1\ 1\ 0]$, $[1\ 0\ 1]$ planes reveals the mixed ionic, covalent nature of bonding present in CsPbCO_3F . Our further calculations on the linear optical properties (absorption spectrum, real and imaginary parts of dielectric function, ordinary and extraordinary refractive indices, birefringence) also show considerable differences in the results obtained before and after SO inclusions into the calculations. Our further observations about optical transitions associated in this material show important changes with respect to SO effects. These differences alone decides importance of SO effects for understanding the optical response of CsPbCO_3F . CsPbCO_3F is a best phase matching material in deep-UV region with a highest static birefringence value 0.1049 among all the other reported carbonate fluorides. Moreover, the present Born effective charge analysis suggest that, Cs and Rb atoms show negative contribution to the birefringence; whereas Pb, C, F atoms positively contributes to the birefringence. We strongly believe that our present study about optoelectronic, linear optical properties are very crucial in understanding the structure-property correlation of carbonate fluorides family. We hope our present results will ignite many experimental researchers to look into the uniqueness of CsPbCO_3F crystal and to invent many more efficient crystals in the carbonate fluorides family.

References

- [1] S. N. Rashkeev, W. R. L. Lambrecht and B. Segall, *Phys. Rev. B*, **57**, 3905 (1998).
- [2] J. L. P. Hughes and J. E. Sipe, *Phys. Rev. B*, **53**, 10751 (1996).
- [3] V. I. Gavrilenko, *Phys. status solidi A*, **188**, 1267 (2001).
- [4] C. Ambrosch-Draxl and J. O. Sofo, *Comput. Phys. Commun.*, **175**, 1 (2006).
- [5] D. E. Aspnes, *Phys. Rev. B*, **6**, 4648 (1972).
- [6] R. C. Eckardt, H. Masuda, Y. X. Fan and R. L. Byer, *IEEE J. Quant. Electron.*, **26**, 922 (1990).
- [7] R. Arun Kumar, *J. Chem.*, **2013**, 154862 (2012).
- [8] T.T. Tran, H. Yu, J.M. Rondinelli, K.R. Poeppelmeier and P.S. Halasyamani, *Chem. Mater.*, **28**, 5238 (2016).
- [9] M. Ouwerkerk, *Adv. Mater.*, **3**, 399 (1991).
- [10] C.T. Chen, L. Bai, Z.Z. Wang and R.K. Li, *J. Cryst. Growth*, **292**, 169 (2006).
- [11] C.-L. Hu and J.-G. Mao, *Coord. Chem. Rev.*, **288**, 1 (2015).
- [12] P. Shan, T. Sun, H. Chen, H. Liu, S. Chen, X. Liu, Y. Kong and J. Xu, *Sci. Rep.*, **6**, 25201 (2016).
- [13] G. Zou, N. Ye, L. Huang and X. Lin, *JACS*, **133**, 20001 (2011).
- [14] G. Zou, L. Huang, N. Ye, C. Lin, W. Cheng and H. Huang, *JACS*, **135**, 18560 (2013).
- [15] T.T. Tran, P.S. Halasyamani and J.M. Rondinelli, *Inorg. Chem.*, **53**, 6241 (2014).

- [16] G.Yang, G.Peng, N.Ye, J.wang, M.Luo, T.Yan and Y.Zhou, *Chem. Mater.*, **27**, 7520 (2015).
- [17] T.T.Tran, J.He, J.M. Rondinelli and P.S. Halasyamani, *JACS*, **137**, 10504 (2015).
- [18] Y. Lin, C.-L.Hu and J.-G.Mao, *Inorg. Chem.*, **54**, 10407 (2015).
- [19] M.Luo, Y.Song, C.Lin, N.Ye, W.Cheng and X.Long, *Chem. Mater.*, **28**, 2301 (2016).
- [20] L. Kang, S.Luo, H.Huang, N.Ye, Z.Lin, J.Qin and C. Chen, *J. Phys. Chem. C*, **117**, 25684 (2013).
- [21] T.T. Tran and P.S.Halasyamani, *Inorg. Chem.*, **52**, 2466 (2013).
- [22] L. Liu, Y.Yang, X.Dong, B. Zhang, Y. Wang, Z.Yang and S.Pan, *Chemistry - A European Journal*, **22**, 2944 (2016).
- [23] Q.Li, G. Zou, C.Lin and N.Ye, *New J. Chem.*, **40**, 2243 (2016).
- [24] M. Abudourehman, L.Wang, X.Zhang, H.Yu, Z.Yang, C.Lei, J.Han and S.Pan, *Inorg. Chem.*, **54**, 4138 (2015).
- [25] J. Chen, M. Luo and N. Ye, *Z. Anorg. Allg. Chem.*, **641**, 460 (2015).
- [26] G.Zou, G.Nam, H.G.Kim, H.Jo, T.-S.You and K.M. Ok, *RSC Adv.*, **5**, 84754 (2015).
- [27] M. Luo, G.Wang, C.Lin, N.Ye, Y.Zhou and W.Cheng, *Inorg. Chem.*, **53**, 8098 (2014).
- [28] E.Narsimha Rao, G.Vaitheeswaran, A.H.Reshak and S.Auluck, *RSC Adv.*, **6**, 99885 (2016).

- [29] M.J. Verstraete, M.Torrent, F.Jollet, G.Zérah and X.Gonze, *Phys. Rev. B*, **78**, 045119 (2008).
- [30] P. Blaha, K.Schwarz, G.K.H.Madsen, D.Kvasnicka and J. Luitz, WIEN2K, An Augmented Plane Wave + Local Orbitals Program for Calculating Crystal Properties Karlheinz Schwarz, Techn. Universit'at Wien, Austria, 2001. ISBN 3-9501031-1-2.
- [31] F.Tran and P.Blaha, *Phys. Rev. Lett.*, **102**, 226401 (2009).
- [32] A. Bala, T. Nautiyal and S. Auluck, *J. Appl. Phys.*, **104**, 014302 (2008).
- [33] J.Kunes, P.Novk, R.Schmid, P.Blaha and K.Schwarz, *Phys. Rev. B*, **64**, 153102 (2001).
- [34] Q. Jing, G.Yang, J.Hou, M. Sun and H.Cao, *J. Solid State Chem.*, **244**, 69 (2016).
- [35] A. Manchon, H. C.Koo, J.Nitta, S. M. Frolov and R. A. Duine, *Nat. Mater.*, **14**, 871 (2015).
- [36] J. P. Perdew, K.Burke and M.Ernzerhof, *Phys. Rev. Lett.*, **77**, 3865 (1996).
- [37] J.P.Perdew, A.Ruzsinszky, G.b.I. Csonka, O.A.Vydrov, G.E.Scuseria, L.A.Constantin, X.Zhou and K. Burke, *Phys. Rev. Lett.*, **102**, 039902 (2009).
- [38] S.Kumar, P.Suman and S.Auluck, *Adv. Opt. Mater. (AOM)*, **2**, 10 (2014).
- [39] E.Narsimha Rao, S.Appalakondaiah, N.Yedukondalu and G.Vaitheeswaran, *J. Solid State Chem.*, **212**, 171 (2014).
- [40] L. Zheshuai, X. Jiang, L. Kang, P.Gong, S.Luo and L. Ming-Hsien, *J. Phys. D: Appl. Phys.*, **47**, 253001 (2014).
- [41] M. Luo, C. Lin, G. Zou, N. Ye and W. Cheng, *Cryst. Eng. Comm.*, **16**, 4414 (2014).

-
- [42] L. Kang, Z.Lin, J.Qin and C.Chen, *Sci. Rep.*, **3**, 1366 (2013).
- [43] X. Jiang, L. Kang, S.Luo, P. Gong, M.-H.Lee and Z. Lin, *Int. J. Mod. Phys. B*, **28**, 1430018 (2014).
- [44] N.Ye,Q.Chen, B.Wu and C.Chen, *J. Appl. Phys.*, **84**, 555 (1998).
- [45] M. Abudoureheman, L. Wang, X. Zhang, H.Yu, Z. Yang, C.Lei, J.Han and S.Pan, *Inorg. Chem.*, **54**, 4138 (2015).
- [46] S. Sharma, J. K. Dewhurst and C. Ambrosch-Draxl, *Phys. Rev. B*, **67**, 165332 (2003).

Structure-property correlation studies of Potassium 4,4'-Bis (dinitromethyl)-3,3'-azofurazanate (K_2 BDAF)

In this chapter, we turned our attention onto two organic noncentrosymmetric HEM's and broadly explained their structure-property correlations. We have explored the role of crystal structure, chemical composition in predicting the structural, dynamical, electronic and optical properties of newly synthesized two noncentrosymmetric primary explosives namely Potassium 1,1'-Dinitramino-5,5'-bis-tetrazolate (K_2 DNABT), Potassium 4,4'-Bis (dinitromethyl) -3,3'-azofurazanate (K_2 BDAF) using density functional theory simulations. The calculated structural and mechanical properties suggest that, K_2 BDAF and K_2 DNABT are mechanically stable and possess lower bulk modulus values K_2 BDAF (18.91 GPa) < K_2 DNABT (22.4 GPa) than toxic lead azide $Pb(N_3)_2$ (26 GPa). The born effective charge (BEC), vibrational, thermodynamic and phonon dispersion studies reveal that, both the crystals are dynamically stable and K_2 BDAF is found to be more stable, more polarizable and easily detectable than K_2 DNABT. The TB-mBJ electronic band structure study reveals that, K_2 BDAF is an indirect band gap material along R \rightarrow V high symmetry points with a gap of 2.37 eV < K_2 DNABT (3.57 eV, direct). The density of states and charge density plots describes that, both the crystals possess mixed covalent and ionic bonding nature and these results

are consistent with BEC analysis. The Nitrogen, Oxygen and Carbon - p states are found to be dominant near the Fermi level in the valence band. From the optical properties study, it is found that the studied explosive materials have the lowest dielectric constant than well known organic 4-N,N-dimethylamino-4'-N-methyl-stilbazolium tosylate(DAST) nonlinear optical crystal. i.e. $K_2\text{DNABT}$ (2.68) < $K_2\text{BDAF}$ (2.91) < DAST (5.2) and show similar birefringence ($K_2\text{BDAF}$ - at static: 0.32; at 532nm: 0.58), ($K_2\text{DNABT}$ - at static: 0.25; at 532nm: 0.27) as DAST (0.39, 0.55, 0.64) and DSTMS (0.45, 0.63) NLO crystals. For both the studied explosives, the absorption is found to be strong in [010] direction and follows a relation $\alpha(K_2\text{BDAF}) < \alpha(K_2\text{DNABT})$. The difference in BEC analysis reveals that, from $K_2\text{DNABT}$ to $K_2\text{BDAF}$, the positive contribution of atoms to total birefringence is increased as follows: K1 (0.095), O1 (0.692), O2 (0.779), N1 (1.410), N2 (0.923), N3 (0.274), N4 (0.742), N5 (0.845). The negative contribution from C1 is increased by -1.295. Overall, our results are in agreement with experimentally reported sensitivity trend and reasons for the sensitivity differences of $K_2\text{DNABT}$ and $K_2\text{BDAF}$ are explored.

6.1 Introduction

As mentioned in the introduction chapter, due to the unique optical responses, noncentrosymmetric materials [1] got a wide variety of applications in physics, chemistry, material science and medical technology. The discovery of new NCS materials with desirable properties like high nonlinear coefficients, broad phase matching angle, high laser damage threshold value, suitable birefringence, good mechanical, thermal stabilities and ease of crystal growth etc continue to drive enormous research in the domain of nonlinear optics [2–5]. Till now few hundreds of organic, inorganic and semi-organic NLO crystals are synthesized to reach the scientific and industrial needs. In previous chapters, we have explored the structure-property correlations of recent inorganic NLO crystals and we pro-

posed $CsPbCO_3F$ as interesting NLO material. Till now various new class of inorganic NCS materials are discovered by changing the anionic groups like $[BO_3]^{3-}$ [7], $[CO_3]^{3-}$ [8], $[NO_3]^-$ [9], $[IO_3]^-$ [10] which have similar planar triangle structured anionic groups. Among these groups, studies on carbonate fluorides got much attention since last five years due to their high nonlinear responses than well known borate materials. The highest nonlinear coefficient till date was found for $CsPbCO_3F$ crystal ($13.6 \times KDP$) [11] in carbonate family. Similarly, very few $[NO_3]^-$ based crystals are also reported in the literature with a nonlinear coefficients of $5 \times KDP$ [9]. The synthesis of these crystals are slowed down because of their easily dissolvable nature in water and are relatively less explored. Interestingly, many $[IO_3]^-$ based crystals are found to show good NLO coefficients of the order of $> 10 \times KDP$ [10]. Combination of the above mentioned anionic groups with nonlinear coefficients as $5 \times KDP$ [12–14] are also coming up in the literature.

We have investigated the structure-property correlation of noncentrosymmetric K_2BDAF , K_2DNABT through density functional theory calculations in order to understand the origin of mechanical, thermal stability and optical sensitivity mechanisms. We report an in-depth study of structural, mechanical, vibrational properties, phonon dispersion studies, born effective charge analysis, electronic band structure and complex dielectric function, absorption, refractive index, birefringence of these primary explosives which are not well understood/unexplored till today in the literature. We have illustrated the importance of noncentrosymmetric nature of these explosive materials and explained the detection limit, sensitivity differences within a wide spectral frequency range. The present study provides an excellent initiative to this new broad and unexplored area of research on optical response of noncentrosymmetric high energy materials (primary and secondary). We hope these kinds of studies will bridge the gap between the search of stable explosive and high optical quality NLO materials than conventional borates, carbonates, nitrates, iodate NLO materials in near future. The rest of

the chapter is organised as follows: The computational methods employed for the present calculations are mentioned in section 6.2. In section 6.3 we explored structure- mechanical, vibrational, dynamical, bonding, electronic, linear optical property correlations in a detailed manner. In section 6.4, we have given the final conclusions of the present study. Our work could be a starting point in this area of research and we strongly believe that our work on high energy materials will ignite many experimental and theoretical studies in the domain of nonlinear optics and defence related applications.

6.2 Calculation methods

In the present study, for calculating the structural, elastic, vibrational and dynamical stability related properties we have employed the density functional theory calculations through Cambridge Series of Total Energy (CASTEP) program [27, 28]. We have taken the experimental crystal structure of $C_6K_2N_{10}O_{10}$ reported by Shiev et.al in 2017 [21] as input for our calculations. Initially, we have optimized the crystal structure to the convergence thresholds of 5.0×10^{-6} (eV/atom) for energy change, 0.01 eV/Å for maximum force, 0.02 GPa for maximum stress and 5.0×10^{-4} Å for the maximum displacement. We have used Broyden-Fletcher-Goldfarb-Shanno (BFGS) minimization algorithm to perform the cell optimization [29]. We have used the plane wave basis set with 500 eV energy cut-off, 5.0×10^{-7} (eV/atom) SCF threshold with 7x4x3 Monkhorst-Pack [30] k-grid (42 irreducible k-points) in the reciprocal space. The ultra-soft pseudopotential [31] are used to treat the electron-ion interactions for calculating structural and single crystal elastic constant properties. For treating electron-electron interactions, we have used different exchange-correlation functionals like Local-density approximation (LDA)[32–34], Generalized gradient approximation (GGA) through Perdew-Burke-ErnZerhof (PBE)[35], Perdew-Wang 91 (PW91)[34] functionals. To account the dispersion correction effects, the Ortmann-Bechstedt-Schmidt

(OBS)[36] correction for GGA-PW91 and Grimme (G06) scheme for GGA-PBE is used. Within the framework of density functional perturbation theory (DFPT) [38], norm-conserving pseudopotential[37] with 830 eV cut-off energy are utilised for calculating zone centre vibrational properties like infrared (IR) spectra, Born Effective charges (BEC) [40] on each constituent atom and Phonon dispersion curves in the first Brillouin zone. The valence electrons of each atom are considered as follows: C (2s² 2p²), N(2s² 2p³), O (2s² 2p⁴), K (3s² 3p⁶ 4s¹). We have explained the intensity differences of the vibrational spectra by using the relation $I_i = [\sum_{j,k} F^l_{ij} A_{j,k}]^2$; $A_{ij} = \partial E / \partial q_i \partial \mu_i$ [39]. Here, A is BEC tensor, E is total energy, F^l is eigenvector, q_i is cartesian coordinate and μ_i is dipole moment. In addition, we have also calculated the important thermodynamic properties like enthalpy, free energy, entropy, lattice heat capacity and Debye temperature to explain the phase stability within the quasi-harmonic Debye model [41]. Further, the full-potential linearized augmented plane wave (FP-LAPW) and local orbitals method [42] is used for studying the electronic structure and optical response. The self-consistency is achieved by using angular momentum expansion $l_{max} = 10$, plane wave cut-off $K_{max} \times R_{MT} = 7$ with 11x7x5 Monkhorst-Pack k-grid [30]. The muffin-tin (MT) radii 1.17 for Carbon, 2.5 for Potassium, 1.19 for Oxygen and 1.13 for Nitrogen are used in the calculations. The energy tolerance 0.0001 Ry and force tolerance 1 mRy/bohr are used. Various exchange-correlation functionals like LDA [34], PBE [35], PBEsol [46], Tran-Blaha modified Becke-Johnson approach (TB-mBJ) [45, 47] and new parameterization of TB-mBJ are used to calculate the accurate electronic band gaps. A denser 14x9x7 K-mesh with 1000 k-points is used in the reciprocal space to calculate the various optical properties.

6.3 Results and discussion

6.3.1 Crystal structure and mechanical stability

Detonation mechanism of an explosive can be understood by knowing the (mechanical thermal and electrical) energy transfer mechanism from the lattice to the molecule and from one part of the solid to other part [48]. To understand the detonation initiation mechanism of newly synthesized green primary explosives K_2BDAF and K_2DNABT , as a first step, we have optimized the experimental crystal structure to capture the influence of lattice packing and intermolecular interactions. The Potassium 4,4'-Bis (dinitromethyl)-3,3'-azofurazanate ($C_6N_{10}O_{10}K_2 - K_2BDAF$) [21] is a newly synthesized green primary explosive which consists of two dinitromethyl groups, azofurazan moiety. It crystalizes in space group $P\bar{1}$ (No.2, point group C_i^1), Triclinic unit cell with $Z=1$ formula unit with lattice vectors $a = 4.9299\text{\AA}$, $b = 7.5171\text{\AA}$, $c = 9.7804\text{\AA}$. The lattice angles are found to be $\alpha = 83.070\text{\AA}$, $\beta = 84.112\text{\AA}$, $\gamma = 85.658\text{\AA}$, with Volume = 357.16\AA^3 . All the constituent atoms in the unit cell are situated at $(2i)$ Wyckoff position with multiplicity 2. The experimental crystal structure of K_2BDAF (see Fig 6.1, 6.2, 6.3) consists of two $C_3N_5O_5K$ units connected along N_5-N_5 bond. This complete molecule is arranged as layers along Z-axis in the unit cell and the adjacent intermolecular distances along Y-axis are found to be 2.843\AA through K-O bond as shown in Fig 6.1, 6.2, 6.3. Similarly, its iso-structural compound $K_2C_2N_{12}O_4$ (K_2DNABT) [20] is also found to crystallize in $P\bar{1}$ symmetry, triclinic structure with $Z=1$. All the atoms are sitting at $2i$ Wyckoff position in the unit cell. From K_2BDAF to K_2DNABT , a slight increment in the lattice parameters and lattice angles are mainly observed due to change in the number of Carbon (-4), Nitrogen (+2), Oxygen (-6) atoms in the unit cell. To understand the role of excess number of atoms on the structural stability via intermolecular interactions, we have optimized the experimental K_2BDAF crystal structure by using different exchange-correlation functionals LDA, GGA (by applying PBE, PW91) which

are implemented in CASTEP. The obtained lattice parameters (a, b, c), lattice angles (α , β , γ) and volume (V) along with experimental data are tabulated in Table 6.1. From these calculated results, we found that, the volume of the unit cell is underestimated by 8.2% with LDA, and overestimated by 15.7%, 15.2% with PBE and PW91. Moreover, these deviations are found to be more in K₂DNABT case, which is obvious due to excess interactions. In addition, the observed large deviations in lattice vectors ‘a’ (-2.9%, 11.8%, 11.0%), ‘c’ (-3.6%, 3.2%, 3.5%) of K₂BDAF with LDA, PBE, PW91 (see Table 6.1) clearly indicates the poor description of intermolecular, interlayer interactions along x and z-directions (see Fig 6.1, 6.2, 6.3). Therefore, in order to get correct lattice vectors and volume, we optimized the system by including the weak van der Waals (vdW) interactions through PBE+G06 and PW91+OBS dispersion correction methods. The results show considerable improvement in the prediction of interactions between the constituent atoms. The calculated unit cell volume with G06 (2.8%) and OBS (4.7%) dispersion corrected methods are found to be relatively in good agreement with experimental data. The poor prediction of atomic interactions with different functionals in K₂BDAF than K₂DNABT can be attributed to the more atomic interactions due to excess number of C, N, O atoms in the unit cell. Hence, we have used the G06 optimized crystal structure as an input for our further calculation purposes.

Table 6.1: Calculated ground state lattice vectors (a, b and c, in Å), volume (V, in Å³), density (ρ in gr/cc) of K₂BDAF, using LDA, PBE, PW91 and dispersion corrected PBE (PBE+G06), PW91 (PW91+OBS) along with experimental data [21]. The percentage of deviations in lattice parameters are given in parenthesis.

Symmetry	Compound	Parameter	LDA	PBE	G06	PW91	OBS	Experiment
P-1 (Z=1)	C ₆ N ₁₀ O ₁₀ K ₂	a	4.786(-2.9%)	5.514(11.8%)	5.056(2.5%)	5.472(11.0%)	5.080(3.0%)	4.929
		b	7.328(-2.5%)	7.567(0.6%)	7.537(0.2%)	7.578(0.8%)	7.566(0.6%)	7.517
		c	9.428(-3.6%)	10.096(3.2%)	9.777(-0.03%)	10.121(3.5%)	9.894(1.1%)	9.780
		V	327.540(-8.2%)	413.519(15.7%)	367.414(2.8%)	411.469(15.2%)	374.184(4.7%)	357.164
		α	83.919	81.103	83.169	81.027	82.128	83.070
		β	85.777	83.455	84.254	83.129	84.006	84.112
		γ	86.649	87.913	85.779	87.400	86.229	85.658
		ρ	2.2830(9.0%)	1.8083(13.6%)	2.0352(-2.8%)	1.8173(-13.2%)	1.9984(-4.5%)	2.0936

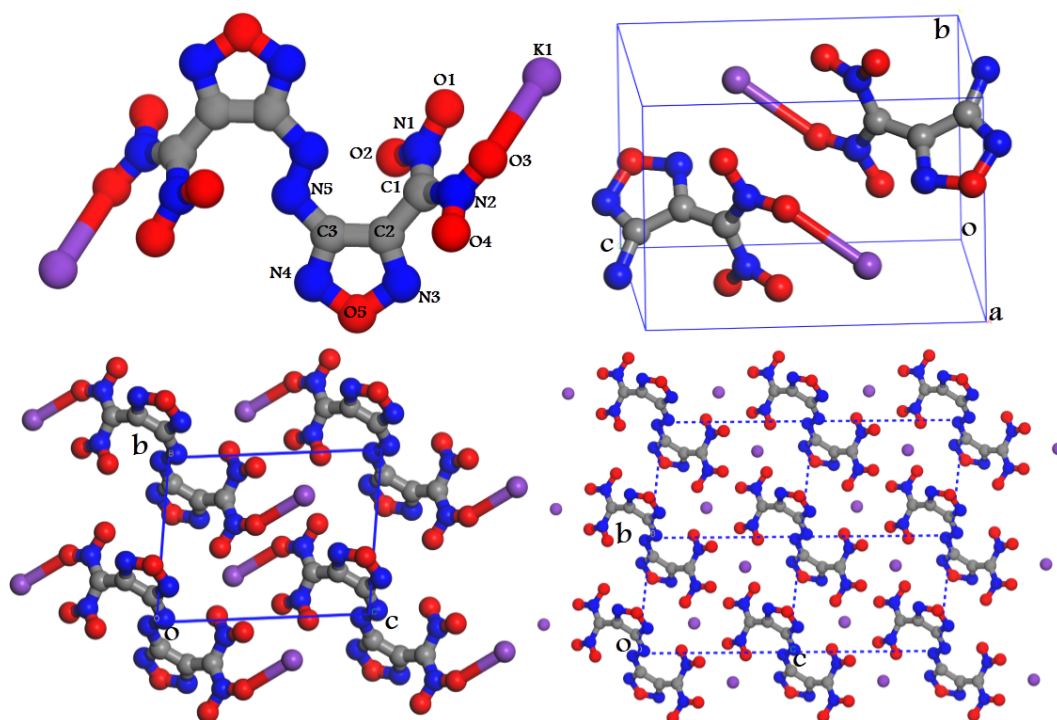


Figure 6.1: Experimental crystal structure of Potassium 4,4'-Bis (dinitromethyl)-3,3'-azofurazanate ($C_6N_{10}O_{10}K_2$).

To understand the strength of lattice interactions, stress response and mechanical stability of the explosives of present interest, initially we have calculated the single crystal elastic constants and bulk modulus (B) values. It is well known that, for triclinic crystal structure, the elastic tensor consists of 21 independent elastic constants, i.e (1) C_{11} , C_{22} , C_{33} which will map applied longitudinal strains into longitudinal stress in the parallel direction, (2) C_{12} , C_{13} , C_{23} will map longitudinal strains into longitudinal stress in the orthogonal direction, (3) C_{14} , C_{15} , C_{16} , C_{23} , C_{24} , C_{25} , C_{26} , C_{34} , C_{35} , C_{36} will map applied longitudinal strains into shear stresses, (4) C_{44} , C_{55} , C_{66} , C_{45} , C_{46} and C_{56} will map shear strains into shear stresses [49]. We have calculated the magnitude of all these constants for K_2BDAF , K_2DNABT using G06 optimised crystal geometries. The obtained results along with bulk modulus values are tabulated in Table 6.2. Since there is an ambiguity

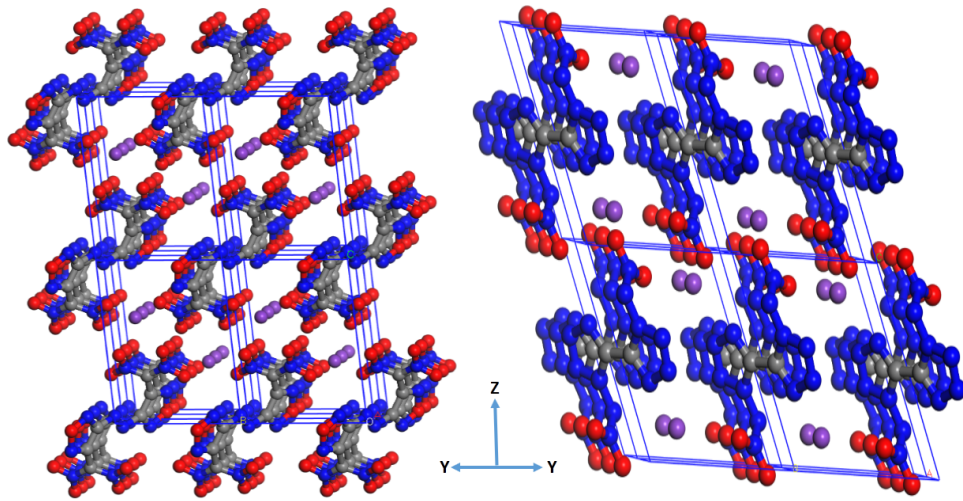


Figure 6.2: Experimental crystal structure of K_2 BDAF and K_2 DNABT (left to right) in y-z plane.

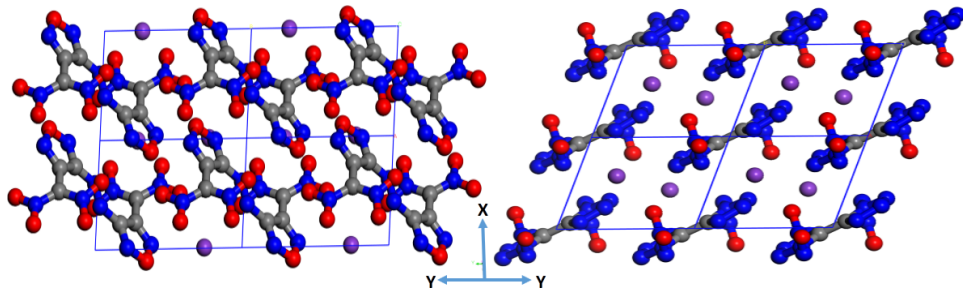


Figure 6.3: Experimental crystal structure of K_2 BDAF and K_2 DNABT (left to right) in x-y plane.

about the correct mechanical stability criteria for triclinic systems and unavailability of experimental data, we have verified the mechanical stability by following Flix Mouhat [50] criteria. We found from elastic constant results (calculated for the G06 optimized structures) that, all the diagonal elements are positive in magnitude which in turn confirms that the studied materials are mechanically stable. Whereas, few off-diagonal elastic constants are showing negative magnitude. These values simply inform that, for the applied strain, the stress component in the resultant direction is tensile rather than compressive. The negative elas-

tic components (see Table 6.2) of K_2BDAF (8) and K_2DNABT (9) informs that, due to large tensile stresses K_2DNABT may become relatively less stable than K_2BDAF . The comparison of parallel longitudinal stress components are showing the following relations: (1) K_2BDAF : $C_{22} > C_{33} > C_{11}$ (more stiffer along y direction); (2) K_2DNABT : $C_{33} > C_{22} > C_{11}$ (more stiffer along z direction). Whereas the orthogonal longitudinal stress components show the relation $C_{12} > C_{13} > C_{23}$ for both the crystals. Overall, the magnitude of C_{22} , C_{11} are found to be more for K_2DNABT and C_{33} , C_{12} , C_{13} , C_{23} are higher for K_2BDAF . This can be attributed to the stronger interatomic interactions in x, y directions and weaker interactions along z-axis of K_2DNABT than K_2BDAF . Therefore based on the elastic constants magnitude we can conclude that, K_2DNABT will show lowest detonation sensitivity along y, x directions (hard to compress) and it is highly sensitive along z direction. Whereas, K_2BDAF will show low detonation sensitivity along y direction and high sensitivity along x direction. Interestingly both materials show similar sensitivity along z direction. The calculated single crystal bulk modulus and compressibility values K_2BDAF (G06: 20.22 GPa, 0.0494 (1/GPa)) and K_2DNABT (21.01 GPa, 0.0475 (1/GPa)) also confirmed the same. However, K_2BDAF is found to be soft material than toxic primary explosive $Pb(N_3)_2$ (26 GPa [52], 41 GPa [53]) and harder than highly sensitive organic primary explosive C_3N_{12} (12.6 GPa) [51]. From the obtained single crystal Young's modulus (E) values using G06 along X, Y, Z directions, we find K_2DNABT (20.0 GPa, 28.09 GPa, 32.85 GPa) $>$ K_2BDAF (17.31 GPa, 30.84 GPa, 24.71 GPa). This indicates that, K_2BDAF is stiffer in $\langle 010 \rangle$ direction and softer in $\langle 100 \rangle$ direction. Whereas, K_2DNABT is found to be stiffer in $\langle 001 \rangle$ and softer in $\langle 100 \rangle$ direction. In contrast, along $\langle 010 \rangle$ direction K_2BDAF exhibits more strength than K_2DNABT and this can be attributed to the presence of extra nitrate group along y-direction (see Fig 6.1, 6.2, 6.3).

Since the shear deformations play a crucial role in understanding the initiation of detonation via friction sensitivity in explosives [54], we focused on cal-

Table 6.2: Calculated single crystal elastic constants C_{ij} and bulk modulus values for K₂BDAF, K₂DNABT using PBE + G06 theoretical equilibrium volume's.

Elastic constant	C_{11}	C_{22}	C_{33}	C_{44}	C_{55}	C_{66}	C_{12}	C_{13}	C_{14}	C_{15}	C_{16}
K ₂ BDAF	30.52	53.55	38.80	13.85	17.21	18.34	22.84	15.26	-4.15	-1.50	0.38
K ₂ DNABT	31.93	37.53	47.77	11.26	12.47	14.04	14.87	18.05	-0.66	-1.40	-0.69
Elastic constant	C_{23}	C_{24}	C_{25}	C_{26}	C_{34}	C_{35}	C_{36}	C_{45}	C_{46}	C_{56}	B
K ₂ BDAF	10.54	-5.76	7.70	-7.07	-7.51	-8.08	5.64	-1.63	0.55	-8.79	20.22
K ₂ DNABT	7.38	-4.75	-3.29	4.44	-2.18	5.71	-0.16	3.45	-5.42	-1.92	21.01

culating the polycrystalline elastic constants like bulk modulus, shear modulus (G), Poisson's ratio (σ), Young's modulus (E), using Voigt, Reuss, Hill approximations [55–57] and verified the mechanical strength of the studied materials in bulk form. It is clear from the results (shown in Table 6.3) that, all the polycrystalline constants except Poisson's ratio σ are found to be higher for K₂BDAF than K₂DNABT. The $B_H > G_H$ values of K₂BDAF ($22.34 > 12.62$) $>$ K₂DNABT ($21.49 > 11.21$) suggest's that, both crystals are more resistant to the hydrostatic compression (volume change) than the uniaxial compression (shape change). Consequently, K₂BDAF is found to show more resistant against the hydrostatic, uniaxial compression than K₂DNABT. The increment of G_H value by $\sim 12\%$ of K₂BDAF over K₂DNABT suggests the increased resistance to shear/highly insensitive to friction. These observations are in good agreement with experimental friction sensitivity (FS) trend K₂BDAF (FS = 20 N) $>$ K₂DNABT (FS = 1 N) [20, 21]. It is known that, according to the Pugh's criteria [58], based on the B/G ratio threshold value (1.75) one can predict whether the given material possesses ductility or brittle nature. For the present materials the obtained B_H / G_H values 1.76, 1.91 (see Table 6.3) which are greater than 1.75 suggests that, both the studied crystals are ductile in nature and ductility is increased from K₂BDAF to K₂DNABT by $\sim 8\%$. Similarly, to explore the response of the studied materials to the applied uniaxial tensions, shear strains we have calculated the polycrystalline Young's modulus and Poisson's ratio's (0.26, 0.27) using the relations $E = (9GB)/(G+3B)$; $\sigma = (E/2G)-1$ [59]. The difference in E values (see Table 6.3) of

studied explosives indicate that, K₂BDAF is more resistant to the applied uniaxial strains. Further, it is known that the Poisson's ratio = 0.1 for covalent materials and it is equal to 0.25 for ionic materials [60]. This strategy in the present study tells that, the studied materials possess mixed covalent-ionic nature. Moreover, when $\sigma = 0.5$ there will not be any change in the volume of the material to the applied strain. This criterion confirms that, a large volume change upon the applied elastic strain occurs in both the studied crystals in polycrystalline form. These observed difference in the σ values (K₂BDAF: 0.26 < K₂DNABT: 0.27) along with the crystal densities (2.09, 2.17) are well correlated to the experimentally observed detonation velocities trend (K₂BDAF: 8138 m/s < K₂DNABT: 8330 m/s). Moreover, the observed bond strengths from relatively higher σ value and larger elastic constants (see Table 6.2) of K₂DNABT are good in agreement with the experimentally observed detonation pressure trend (K₂BDAF: 30.1 GPa < K₂DNABT: 31.7 GPa). Further, we have also calculated the micro hardness (H) ($H = (1-2\sigma)E / 6(1+\sigma)$) [57] value of the two explosives to know their response to the applied small forces. From the obtained results, it is found that K₂DNABT (H = 0.64) can be considered as a relatively low-hardness material than K₂BDAF (H = 0.79). Hence, the calculated Young's modulus and micro hardness values collectively represent the experimentally observed large sensitivity to impact of K₂DNABT (1 Joule) than K₂BDAF (2 Joule) [20, 21]. Additionally, the universal anisotropy index of the present materials is also evaluated by Ranganathan and Ostoja-Starzewski method [61]. It is known that, when the obtained universal anisotropy factor is 1, then material is supposed to be fully isotropic otherwise it will be anisotropic in nature. From our calculations, the anisotropy factor of K₂DNABT (1.56) and K₂BDAF (2.33) are found to deviate largely from '1' which in turn explain's that, both the explosives possess large anisotropy and the degree of anisotropy is found to be approximately double for K₂BDAF than that of K₂DNABT. Overall, the calculated mechanical properties collectively indicate that K₂BDAF is more resistant to the impact, friction than K₂DNABT and con-

clusion drawn in this section are in consistent with experimental results trend.

Further, we compared the results with other well known explosives and non-linear optical materials to find the applications of present studied compounds in the respective fields. Interestingly, K₂BDAF and K₂DNABT showing high hardness values than other well known explosive materials RDX (H = 0.241 GPa, E = 18.4 GPa, σ = 0.11), PETN (H = 0.179 GPa, E = 13.7 GPa, σ = 0.11) and β -HMX (H = 0.403 GPa, E = 31 GPa, σ = 0.06) [62]. In NLO applications point of view, the present studied materials possesses similar hardness values as well known KDP crystal (H \sim 1.4 GPa) [65] and higher than DAST (H \sim 0.31 GPa, The Young's modulus = 13.8 GPa) crystal [63]. As we know, when a high power laser is incident on a material for various optical purposes, its mechanical stiffness is an important criterion to explain durability (damage threshold) of that material. Hence, from our results we can conclude that K₂DNABT, K₂BDAF are mechanically stable (durable) materials as like RDX, PETN, KDP, DAST crystals.

Table 6.3: The calculated polycrystalline elastic constants (bulk (B_X), shear moduli (G_X , B_H/G_H ratio) using the Voigt, Reuss, Hill approximations (X=V,R,H) and the Poisson's ratio σ , Young's modulus (E), micro hardness (H)). All values are calculated at the G06 equilibrium volumes

Compound	B_V	B_R	B_H	G_V	G_R	G_H	B_H/G_H	σ	E	H
K ₂ BDAF	24.46	20.22	22.34	14.82	10.41	12.62	1.76	0.262	31.86	0.792
K ₂ DNABT	21.98	21.01	21.49	12.68	9.73	11.21	1.91	0.277	28.65	0.649

6.3.2 Born effective charges and vibrational properties

Born effective charge is a result of the coupling between the electrostatic fields and lattice displacements. In order to explore more about the ionic, covalent bonding nature and to get insight knowledge about the polarization mechanism, we have calculated the BEC tensor and the infrared vibrational spectra of K₂BDAF and K₂DNABT using DFPT method [64]. The resultant BEC values of each in-

dividual atom of K_2BDAF are tabulated in Table 6.4 and results of K_2DNABT are shown in Table 6.5. In both cases, the sum of all BEC values are resulting in zero value (acoustic sum rule $\sum_k Z_{k,ii}^* = 0$), which indicates the good convergence of our calculations within 0.0001 accuracy [67]. The tabulated results in Table 6.4 & Table 6.5 indicates that, the effective charges on all the atoms O, C, K, N show large deviations from their corresponding ionic charges -2, +4, +1, -3 respectively. Because of the same symmetry, the effective charge tensors are following the below criteria in both the studied crystals: $Z_{11}^* \neq Z_{22}^* \neq Z_{33}^*$ and $Z_{xy}^* \neq Z_{yz}^* \neq Z_{zx}^*$ (here x, y, z varies from 1,2,3). Overall, the magnitude of BEC's clearly indicates that, the bonding between the constituent atoms in both the studied materials are covalent in nature. We have shown the percentage of deviation in effective charges on each atom from its ionic charge values along xx, yy, zz directions in right side of Table 6.4 and Table 6.5. The order of BEC's deviations (or the strength of polarizability) of different atoms are showing the relation: $N > C > O > K$ in both the crystals. However, the strength of deviations for the studied crystals shows the relation: $K_2BDAF_{(N>C>O>K)} > K_2DNABT_{(N>C>O>K)}$ which clearly enlighten that, K_2BDAF is more polarizable and optically active material than K_2DNABT . Therefore, we further examined the direction dependent polarizability strength of K_2BDAF along xx, yy, zz directions and the conclusions are as follows: The atoms $K_1, O_1, O_3, N_1, N_2, N_5, C_1, C_2$ are showing large charge deviation along yy direction than in other two directions (see Table 6.4). Whereas, O_4, N_4, C_3 are showing more charge deviations along xx direction and O_2, O_5, N_3 atoms are showing much deviation along zz direction. It clearly indicates that, K_2BDAF is more polarizable in yy direction than in other two directions. Similarly, K_2DNABT is found to be more polarizable along zz direction due to Nitrogen atoms (see BEC deviation of N atoms in Table 6.5).

Since the ground state vibrational spectra give crucial information about the intermolecular interactions in the low energy window, as a next step we have calculated the zone centre vibrational frequencies of K_2BDAF (infrared spectra (see

Table 6.4: Calculated BEC's for all inequivalent atoms of K₂BDAF at the theoretical equilibrium volume (left side table). Actual ionic charges are O = -2, C = +4, K = +1, N = -3. Percentage of deviations of BEC's all inequivalent atoms are shown in (right side table) along xx, yy, zz directions.

	Z* ₁₁	Z* ₁₂	Z* ₁₃	Z* ₂₁	Z* ₂₂	Z* ₂₃	Z* ₃₁	Z* ₃₂	Z* ₃₃	Z* ₁₁	Z* ₂₂	Z* ₃₃
K1	1.29870	0.04996	-0.15948	-0.04989	1.50652	0.04181	-0.12822	-0.03644	1.35445	29	50	35
O1	-1.29902	0.37771	0.96900	0.18213	-0.67972	-0.25476	0.57425	-0.35637	-1.05226	35.04	66.01	47.38
O2	-0.92958	-0.59322	0.18327	-0.64936	-1.64940	-0.05993	0.20415	0.10609	-0.58289	53.52	17.53	70.85
O3	-1.10027	-0.69018	0.79630	-0.27560	-0.82543	0.27252	0.73222	0.73528	-1.37738	44.98	58.72	31.13
O4	-0.55652	0.13504	0.18705	0.00455	-1.89389	-0.28660	0.09903	-0.46678	-0.72576	72.17	5.30	63.71
O5	-0.87802	0.51954	-0.03354	0.68293	-0.57724	0.08957	-0.14214	0.28927	-0.32028	56.09	71.13	83.98
N1	1.62868	-0.05570	-1.20545	0.48038	2.45552	0.56069	-0.58262	0.77326	0.90483	154.28	181.85	130.16
N2	1.09769	1.02012	-0.84837	0.56175	3.05900	-0.21919	-0.85391	-0.43938	1.52817	136.58	201.96	150.93
N3	-0.13187	-0.13280	0.11792	0.14716	-0.16361	-0.17009	-0.22885	0.20126	-0.11367	95.60	94.54	96.21
N4	0.53166	-0.64776	0.23837	-0.62162	0.14725	0.08126	0.23898	-0.07158	-0.44951	117.72	104.90	85.01
N5	0.04198	-0.18656	0.14609	-0.24913	0.21677	-0.17045	0.16172	-0.21591	0.08782	11.39	107.22	102.92
C1	-0.19256	-0.27189	0.22897	-0.26271	-1.80668	-0.08582	0.09226	-0.09535	-0.29913	106.41	145.16	107.47
C2	0.55961	0.29993	-0.64536	0.01600	0.05117	0.10813	-0.38625	-0.27892	0.81479	86.00	98.72	79.63
C3	-0.07050	0.17580	0.02522	0.03341	0.15974	0.09286	0.21938	-0.14443	0.23082	101.76	96.00	94.22

Table 6.5: Calculated BEC's for all inequivalent atoms of K_2DNABT at the theoretical equilibrium volume (left side table). Actual ionic charges are $O = -2$, $C = +4$, $K = +1$, $N = -3$. Percentage of deviations of BEC's all inequivalent atoms are shown in (right side table) along xx , yy , zz directions.

	Z_{11}^*	Z_{12}^*	Z_{13}^*	Z_{21}^*	Z_{22}^*	Z_{23}^*	Z_{31}^*	Z_{32}^*	Z_{33}^*		Z_{11}^*	Z_{22}^*	Z_{33}^*
K1	1.33219	0.00799	-0.05639	0.00631	1.25100	0.09472	-0.05055	0.03604	1.30748	K1	33	25	30
O1	-1.66470	0.44917	-0.18347	0.33715	-0.46322	0.01770	0.31955	-0.08651	-0.78304	O1	-16	-76	-60
O2	-0.69545	0.06379	0.07317	0.07458	-0.46053	-0.25732	0.14083	0.04653	-2.30666	O2	-65	-76	15
N1	0.03418	0.12128	-0.14785	0.10252	0.17676	-0.09868	0.05860	-0.16808	0.31727	N1	-101	-105	-110
N2	-0.24047	-0.17928	0.20304	-0.18563	-0.49764	0.23518	0.05760	0.12992	0.10925	N2	-91	-83	-103
N3	-0.18251	0.04464	-0.12016	0.09846	-0.15490	0.01574	-0.14192	-0.00439	-0.47899	N3	-93	-94	-84
N4	-0.28684	-0.07431	0.22461	-0.12714	-0.36905	-0.04702	-0.04136	-0.08349	-0.51493	N4	-90	-87	-82
N5	-0.68149	0.07010	-0.70086	0.07736	-0.32336	-0.01659	-0.33284	0.11638	-1.03943	N5	-77	-89	-65
N6	2.04797	-0.63459	0.77261	-0.47208	0.29919	0.26538	-0.04105	-0.05249	3.05901	N6	-168	-109	-201
C1	0.33713	0.13123	-0.06470	0.08846	0.54176	-0.20910	0.03115	0.06608	0.33003	C1	-91	-86	-91

Fig 6.5)) and the results are tabulated in Table 6.6, 6.7, 6.8. Since the studied compound crystallizes in $P\bar{1}$ space group with $z=1$ formula unit (28 atoms), we have obtained 81 optical modes along with three acoustic modes. This is consistent with the group theory analysis distribution which is shown below:

$$\Gamma_{acoustic} = 3A_u ; \Gamma_{optic} = 39 A_u \oplus 42 A_g \text{ (here } A_u \text{ is IR active, } A_g \text{ is Raman active)}$$

All the obtained zone centre vibrational frequencies are found to be real, which indicates that the studied compound is dynamically stable at Brillouin zone centre. Since there are no other experimental and theoretical studies on vibrational properties to compare, we have taken enough care in doing calculations by minimising the forces on each atom. We have assigned all the vibrational modes for the corresponding frequencies and results are shown in Table 6.6, 6.7, 6.8. However, out of the 81 calculated optical modes we found that, 39 modes (A_u) are IR-active and 42 (A_g modes) are Raman active. From the modes assignment analysis, it was found that, all the higher frequency modes ($> 1000 \text{ cm}^{-1}$) arise mainly due to Asymm. bending and str. of ($C_2=N_3-O_5-N_4=C_3$) CNO ring about C_3-N_5 or C_2-C_1 bond. The detailed analysis is shown in Table 6.6. In mid frequency range (from 300 cm^{-1} to 1000 cm^{-1}), vibrations are mainly arising from Asymm. str., bending, breathing mode of CNO ring along with Asymm. str., bending, breathing of two NO_2 groups (i.e $O_1-N_1-O_2$, $O_3-N_2-O_4$) about C_1 atom. Whereas in the low frequency range ($< 300 \text{ cm}^{-1}$) vibrational modes arise due to the Asymm. str. $K_1 - O_4$ bond and lattice modes (translational, rotational, swinging, twisting of various atoms for different frequencies) (see Table 6.8, Fig 6.4). Few animations of different vibrational frequency modes of K₂BDAF are shown in Fig 6.4 for further reference.

In order to know their intensity differences for analysing the structure and polarization relation, we have calculated the IR-spectra of K₂BDAF material and plotted in Fig 6.5. The results are compared with its iso-structural crystal K₂DNABT results reported in "J.Chem. Phys. 143, 064508 (2015)". The top portion of Fig 6.5 (total IR-spectra) shows that, both the K₂BDAF and K₂DNABT explosives

have unique/different vibrational spectra. This is helpful in detecting these two explosives from one another. However, it is clear from Fig 6.5 that, the highest intensity peaks of K₂BDAF are located as follows:(1) 1223.95 cm⁻¹, (2) 1408.31 cm⁻¹, (3) 1431.28 cm⁻¹, (4) 1112.12 cm⁻¹, (5) 982.63 cm⁻¹, (6) 1495.00 cm⁻¹. These frequencies are mainly arising due to (1) Asymm. str. of N1-C1-N2; (2) Asymm. str. of (O1-N1-O2-C1-O3-N2-O4) and Asymm. str. of CNO ring; (3) Asymm. str. of (O1-N1-O2-C1-O3-N2-O4) and Asymm. str. of CNO ring; (4) Breathing mode of (O1-N1-O2, O3-N2-O4); (5) Asymm. str. of CNO ring; (6) Asymm. str. of CNO ring + C1 along C2-C1 direction. For simplicity, we made an intensity difference analysis for one selected peak of both the studied materials occurring at K₂BDAF(1223.5 cm⁻¹), K₂DNABT (1239.3 cm⁻¹) which is mainly occurring due to N1-C1-N2 vibration. The BEC deviations of these atoms are found to be 75% (N1), 115% (C1), 62% (N2) higher in K₂BDAF than K₂DNABT, which leads to higher intensity peak occurrence for K₂BDAF material. Similar analysis is valid for all other high intensity peaks also.

In terms of terahertz frequencies, K₂BDAF is having 12(IR)+14(R) modes in 0-9 THz (Far-IR) window, 8(IR)+8(R) modes in 9-19.5 THz (Far-IR) window, 9(IR)+9(R) modes in 19.5-30.0 THz (Low wavelength IR (LWIR)) region, 10(IR)+11(R) modes in 30-45 THz (Mid wavelength IR (MWT)) region. Whereas, K₂DNABT is having 9(IR)+11(R) modes in 0-9 THz window, 4(IR)+4(R) modes in 9-19.5 THz window, 7(IR)+7(R) modes in 19.5-30.0 THz, 7(IR)+8(R) modes in 30-45 THz range. The higher number of vibrational modes in each region with larger intensities as shown in the vibrational spectra of K₂BDAF over K₂DNABT clearly indicates that, K₂BDAF is optically very active and sensitive. This can be attributed to the presence of excess number of nitro groups and N-N bond between two CNO-rings with larger BEC's in K₂BDAF than in K₂DNABT. As we know explosives show very unique THz response in 0-20 THz region, we have compared the present results with other THz absorption peak positions of well known explosives like RDX (0.72, 1.26, 1.73 THz), PETN (1.73, 2.51, 2.01

THz), HMX(1.58, 1.91, 2.21, 2.57, 1.84 THz), TNT (1.44, 1.91, 1.7, 5.6, 8.2, 9.1, 9.9 THz), NH₄NO₃ (4, 7 THz) [68]. From these comparisons, we found that K₂BDAF is having more number of peaks within 0-10 THz energy window, which clearly indicates that, detection of K₂BDAF in THz region is more prominent than other explosive materials. We have also compared the THz response of K₂BDAF with well known noncentrosymmetric organic nonlinear optical material DAST which has similar composition (C₂₃H₂₆N₂O₃S). The absorption peaks of DAST are reported at 1.1, 3.1, 5.2, 7.1, 8.4, 11, 12.3 THz along a-axis; and at 1.1, 1.3, 1.6, 2.2, 3, 5.2, 7.2, 9.6, 11.7 THz along b-axis [69]. Thus this comparison describes that, the studied material K₂BDAF is having more THz response than unique DAST NLO material. Overall, from the vibrational properties analysis we can conclude that, K₂BDAF will show better THz spectroscopic response than K₂DNABT, other well known explosives and highly nonlinear DAST crystal. The results analysed in this section play a crucial role for conducting the future detection and synthesis experiments.

6.3.3 Phonon dispersion and thermodynamic properties

In order to know the dynamical stability of the present primary explosive systems in the entire Brillouin zone, we have calculated the complete phonon dispersion along $\Gamma \rightarrow F \rightarrow Q \rightarrow Z \rightarrow \Gamma$ high symmetry path using linear response method as implemented in CASTEP. Both the obtained phonon dispersions are plotted in 0-6 THz range and shown in Fig 6.6. The obtained results don't show any negative or imaginary frequencies at any point in the Brillouin zone, which in turn confirms that both the studied crystals are dynamically stable. It is found that, below 6 THz, K₂DNABT is having 16 optical phonon modes whereas K₂BDAF is having 22 optical phonon modes. This indicates that, K₂BDAF is more sensitive than K₂DNABT to the applied external field thus it is easily detectable material. Moreover, it is well known that the more number of soft modes ($< 100 \text{ cm}^{-1}$) can lead to more anharmonicity thus more thermal expansion. It is also important

Table 6.6: The calculated zone centre high frequency ($> 1000 \text{ cm}^{-1}$) vibrational modes of K_2BDAF and their mode assignments [Here Trans. = Translation, Asymm. = Asymmetric, str. = stretching]

Mode	Frequency	Symmetry	Assignment
M84	1499.40	$A_g(\text{R})$	Asymm. bending of CNO ring + C1 along C2-C1 direction;
M83	1495.00	$A_u(\text{I})$	Asymm. str. of C3 = N4 and C2-C1;
M82	1441.97	$A_g(\text{R})$	Asymm. bending of C2-C1-N1-N2; Asymm. str. of CNO ring;
M81	1431.28	$A_u(\text{I})$	Asymm. str. of (O1-N1-O2-C1-O3-N2-O4); Asymm. str. of CNO ring;
M80	1409.25	$A_g(\text{R})$	Asymm. bending of N2-C1-N1; Asymm. bending of C2-C3-N5;
M79	1408.31	$A_u(\text{I})$	Asymm. str. of (O1-N1-O2-C1-O3-N2-O4); Asymm. str. of CNO ring;
M78	1360.51	$A_g(\text{R})$	Asymm. bending of CNO ring only;
M77	1351.94	$A_g(\text{R})$	Asymm. bending of (O1-N1-O2-C1-O3-N2-O4);
M76	1344.43	$A_u(\text{I})$	Asymm. str. of (O1-N1-O2-C1-O3-N2-O4); Asymm. str. of CNO ring;
M75	1331.27	$A_g(\text{R})$	Asymm. bending of (O1-N1-O2-C1-O3-N2-O4);
M74	1329.08	$A_u(\text{I})$	Asymm. str. of (O1-N1-O2-C1-O3-N2-O4); Asymm. str. of CNO ring;
M73	1320.24	$A_u(\text{I})$	Asymm. str. of (O1-N1-O2-C1-O3-N2-O4); Asymm. str. of CNO ring;
M72	1316.93	$A_g(\text{R})$	Asymm. bending of (O1-N1-O2-C1-O3-N2-O4);
M71	1276.93	$A_u(\text{I})$	Asymm. str. of (O1-N1-O2-C1-O3-N2-O4); Asymm. bending of CNO ring;
M70	1265.32	$A_g(\text{R})$	Asymm. bending of N1-C1-N2 + C1; Asymm. bending of CNO ring;
M69	1250.40	$A_g(\text{R})$	Asymm. bending of N1-C1-N2;
M68	1223.95	$A_u(\text{I})$	Asymm. str. of N1-C1-N2;
M67	1118.57	$A_g(\text{R})$	Asymm. bending of (O1-N1-O2, O3-N2-O4);
M66	1112.12	$A_u(\text{I})$	Breathing mode of (O1-N1-O2, O3-N2-O4);
M65	1054.58	$A_u(\text{I})$	Asymm. str. of CNO ring and O3-N2-O4 + C1;
M64	1045.45	$A_g(\text{R})$	Asymm. bending of total molecule;

Table 6.7: The calculated zone centre mid frequency (from 300 cm⁻¹ to 1000 cm⁻¹) vibrational modes and assignments of K₂BDAF [Here Trans. = Translation, Asymm. = Asymmetric, str. = stretching]

Mode	Frequency	Symmetry	Assignment
M63	992.10	A _g (R)	Asymm. bending of CNO ring;
M62	982.63	A _u (I)	Asymm. str. of CNO ring;
M61	913.75	A _g (R)	Asymm. bending of CNO ring;
M60	909.06	A _u (I)	Asymm. str. of CNO ring;
M59	848.22	A _g (R)	Asymm. bending of CNO ring;
M58	830.18	A _u (I)	Asymm. str. of (N3-O5);
M57	827.96	A _g (R)	Asymm. bending of CNO ring at (N3-O5, N4-C3-N5) only;
M56	800.31	A _u (I)	Breathing mode of (CNO ring+ O1-N1-O2 + O3-N2-O4);
M55	796.53	A _g (R)	Asymm. bending of total molecule except K;
M54	761.14	A _u (I)	Asymm. str. + bending of total molecule; K1-O3 Asymm. str.;
M53	750.61	A _g (R)	Asymm. bending of total molecule except K;
M52	734.71	A _u (I)	Asymm. str. of O1-N1-O2-C1-N2-O3-O4; Asymm. str. of CNO ring;
M51	729.36	A _g (R)	Asymm. bending of O1-N1-O2-C1-N2-O3-O4 + C2-C1-C3;
M50	720.55	A _u (I)	Asymm. str. of (O1-N1-O2), (O3-N2-O4); Asymm. str. of C2-C3-N3-N4, K1-O3;
M49	713.55	A _u (I)	Asymm. str. of (O1-N1-O2), (O3-N2-O4); Asymm. str. of CNO ring along N5;
M48	713.42	A _g (R)	Asymm. bending of (O1-N1-O2), (O3-N2-O4);
M47	696.04	A _g (R)	Asymm. bending of total molecule except K;
M46	692.74	A _u (I)	Asymm. str. + bending of CNO ring along N5 and O1-N1-C1-O2;
M45	606.92	A _u (I)	Asymm. str. + bending of CNO-N5 ring only;
M44	606.41	A _g (R)	Asymm. bending of CNO-N5 ring only;
M43	587.74	A _u (I)	Asymm. bending of CNO-N5 ring only;
M42	489.05	A _u (I)	Asymm. str. + bending of CNO ring + O1-N1-O2-C1-N2-O4;
M41	469.26	A _g (R)	Asymm. bending of CNO ring + O1-N1-O2-C1-N2-O3-O4;
M40	455.27	A _u (I)	Asymm. bending of O1-N1-O2-C1-N2-O3-O4 only;
M39	448.08	A _g (R)	Asymm. bending of CNO ring + O1-N1-O2-C1-N2-O3-O4;
M38	445.09	A _g (R)	Asymm. bending of CNO ring + O1-N1-O2-C1-N2-O3-O4;
M37	429.49	A _g (R)	Asymm. bending of CNO ring + O1-N1-O2 about C2-C1-N1 bond;
M36	414.99	A _u (I)	Asymm. str. of O2-N1-C1-N2-O3-K4; Libration of C2-C3-N4-N5 bond in CNO ring
M35	402.78	A _u (I)	Asymm. str. of O2-N1-C1-N2-O3-K4; Asymm. str. of CNO ring
M34	382.03	A _g (R)	Asymm. bending of CNO ring at C2-C3-N5 + O1-N1-O2-C1-N2-O3-O4;
M33	359.10	A _u (I)	Asymm. str. O2-N1-C1-N2-O4 and CNO ring at C3-N5;
M32	330.33	A _g (R)	Asymm. bending of CNO ring + O1-N1-O2-C1-N2-O3-O4;
M31	310.67	A _g (R)	Asymm. bending of CNO ring; Rotation of O1-N1-O2; Asymm. bending of N1-C1-N2;
M30	307.03	A _u (I)	Asymm. Str. of CNO ring at C1-C2, C2-C3, N4-C3-N5; Asymm. Str. of C1-N1-O1;

Table 6.8: The calculated zone centre low frequency ($< 300 \text{ cm}^{-1}$) vibrational modes of K_2 BDAF and their mode assignments [Here Trans. = Translation, Asymm. = Asymmetric, str. = stretching]

Mode	Frequency	Symmetry	Assignment
M29	247.65	A_u (I)	Asymm. str. of O1-N1-O2-C1-N2-O3-O4 about C1-C2 bond; Asymm. str. of C1-C2 bond and CNO ring;
M28	244.67	A_g (R)	Asymm. bending of O1-N1-O2-C1-N2-O3-O4; Asymm. bending of CNO ring;
M27	217.06	A_g (R)	Asymm. bending of O1-N1-O2-C1-N2-O3-O4; Asymm. bending of CNO ring;
M26	205.19	A_g (R)	Asymm. bending of O1-N1-O2-C1-N2-O3-O4; Twisting of CNO ring about C2-C3;
M25	193.93	A_u (I)	Asymm. str. of CNO ring and O1-N1-C1;
M24	170.87	A_u (I)	Asymm. str. of K1-O3-N2-O4 bond; Asymm. str. of O1-N1-O2, N3-O5-N2;
M23	168.02	A_g (R)	Swinging of O5-N4 = C3-O5 about C2-C1; Asymm. bending of K1-O3-N2-O4;
M22	159.55	A_g (R)	Asymm. bending of O4-N2-O3;
M21	157.29	A_u (I)	Asymm. str. of K1-O3-N2-O4 bond and Asymm. str. (O1-N1-O2);
M20	148.35	A_g (R)	Asymm. bending of K1-O3-N2-O4 bond; Twisting of O1-N1-O2 along N1-C1 bond;
M19	139.67	A_u (I)	Asymm. str. of K1-O3; Asymm. str. of N2-C1-(O1-N1-O2); Swinging of CNO ring about C2-C3;
M18	137.66	A_g (R)	Asymm. bending of K1-O3-N2, CNO ring AT C1-N4-C2; Translation of (O1-N1-O2)-C1-(O3-N2-O4);
M17	131.53	A_g (R)	Twisting of (O1-N1-O2)-C1; Asymm. bending of (K1-O3-N2-O4) about N1-C1;
M16	130.59	A_u (I)	Twisting of (O3-N2-O4) along with K1-O3-N2 Asymm. str.; Swinging of N3-O5-N4 about C1-C2 axis;
M15	125.11	A_u (I)	Asymm. str. of K1-O3; Asymm. str. of (O1-N1-O2)-C1; Asymm. str. of CNO ring at C2-C3 bond;
M14	122.29	A_g (R)	Asymm. bending of (O1-N1-O2), (O3-N2-O4-K1) about C1-C2; Rotation of CNO-N5 ring along C3-N5 axis;
M13	113.61	A_u (I)	Asymm. str. of K1-O3-N2; Asymm. stretch of (O1-N1-O2) along C1; Rotation of N5 + CNO ring;
M12	110.84	A_g (R)	Asymm. bending of (O1-N1-O2)-C1-(O3-N2-O4); Asymm. str. of K1-O3;
M11	109.17	A_u (I)	Twisting of (O1-N1-O2); Twisting of (O3-N2-O4) + Asymm. str. of K1-O3; Twisting of CNO ring along C2-C3 bond;
M10	89.66	A_g (R)	Asymm. bending of (O1-N1-O2)-C1; Translation of (O3-N2-O4);
M09	82.99	A_u (I)	Asymm. str. of CNO ring at N3-O5-N4 bond; Asymm. str. of K1-O3 bond; Translation of (O1-N1-O2) + (O3-N2-O4);
M08	80.77	A_g (R)	Swinging of (O1-N1-O2) + (O3-N2-O4) along C1-C2 bond;
M07	64.99	A_u (I)	Rotation of total molecule;
M06	63.00	A_g (R)	Translation of total molecule except N5; Asymm. bending of (O1-N1-O2);
M05	53.32	A_u (I)	Rotation of (O1-N1-O2) + (O3-N2-O4) about C1-C2 bond axis; Translation of N5 + (C2 = N3-O5-N4 = C3) ring; Asymm. str. of K1-O3;
M04	52.30	A_g (R)	Swinging of (O1-N1-O2) + (O3-N2-O4) along C1-C2 bond; which involves Translation of (O3-N2-O4), Twisting of (O1-N1-O2);

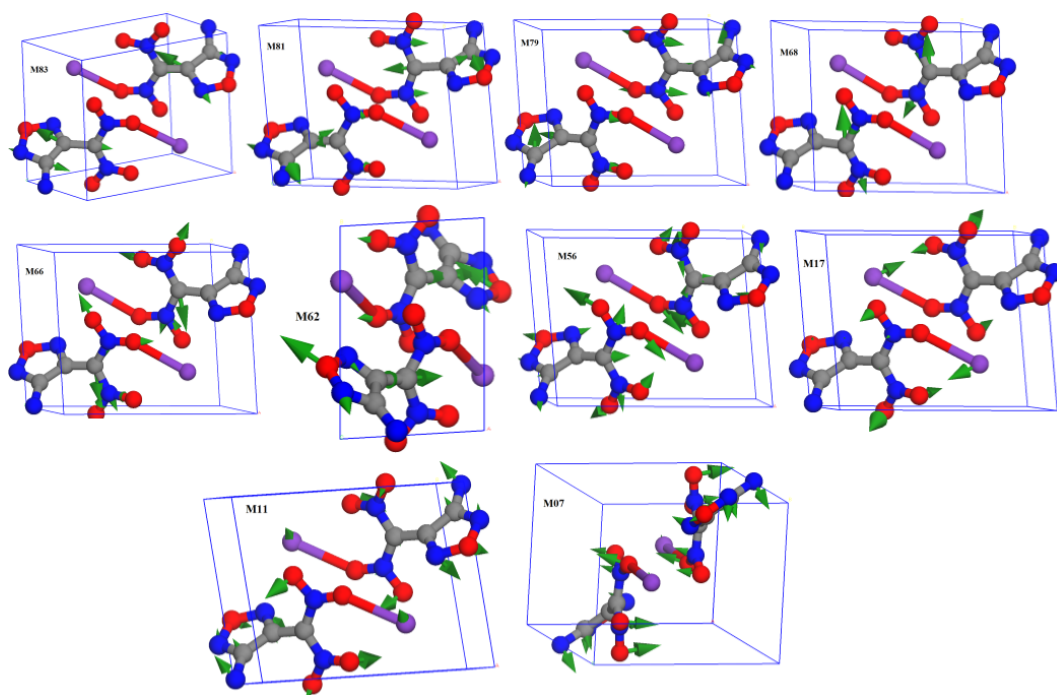


Figure 6.4: Snapshot images of few vibrational modes (M07, M11, M17, M56, M62, M66, M68, M79, M81, M83) of K_2BDAF .

to notice from the acoustic phonon modes that, the slopes of the acoustic modes in case of K_2DNABT is more when they are approaching to zero in the Brillouin zone high symmetry point. Which clearly indicates that, low thermal conductivity, higher elastic constants may exist in K_2DNABT than K_2BDAF . Overall, it is important to notice that, K_2DNABT could be less thermally stable primary explosive than K_2BDAF . Our analysis are in good agreement with the reported experimental decomposition temperature observations of K_2DNABT (473.15 K) and K_2BDAF (502.15 K). The total phonon density of states(PDOS) calculated on $5 \times 3 \times 3$ Monkhorst-Pack grid are plotted as shown in Fig 6.6 (top portion). It is clear from the plot that, in case of K_2BDAF , the PDOS are randomly distributed through out the energy window (0-47 THz) with a smaller gap between phonon branches than K_2DNABT and the intensity are found to be approximately similar. Which clearly indicates that phonon-phonon and electron-phonon couplings

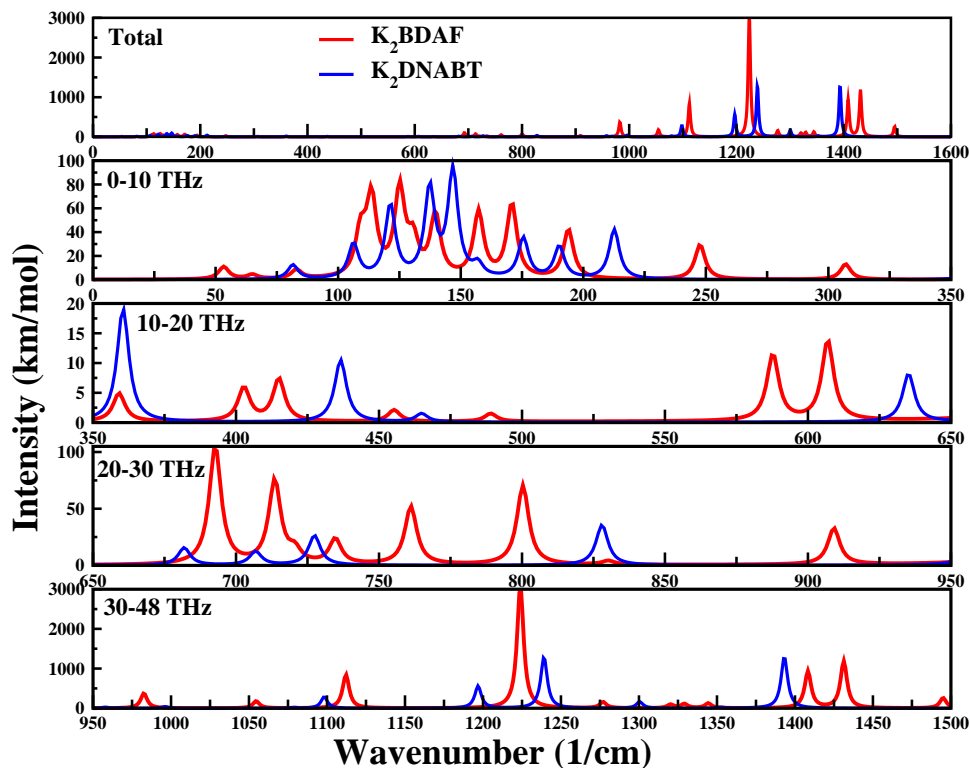


Figure 6.5: Calculated IR-spectra of K_2BDAF , K_2DNABT crystal structures optimized at G06 level. Here, IR-spectra of K_2DNABT is recalculated as reported in “J. Chem. Phys, 143, 064508, 2015” and plotted on top of K_2BDAF IR-spectra for analysis purpose.

will be more in K_2BDAF .

Further to know more details about the phase stability differences, we have calculated the thermodynamic properties like Enthalpy (H), Free energy (F), Entropy (S_v), Heat capacity (C_v) and Debye temperature ($\Theta(V)$) by using quasi-harmonic Debye model[41]. The obtained results are shown in Fig 6.7. It is clear from the plot that, K_2BDAF is showing higher enthalpy, lower free energy, high entropy, higher heat capacity and lower Debye temperature than K_2DNABT in 0 - 1000K temperature window. This can be attributed to more lower soft modes in K_2BDAF leads to greater entropy thereby reducing the free energy. The heat capacity curves for K_2BDAF shows higher values throughout the studied temper-

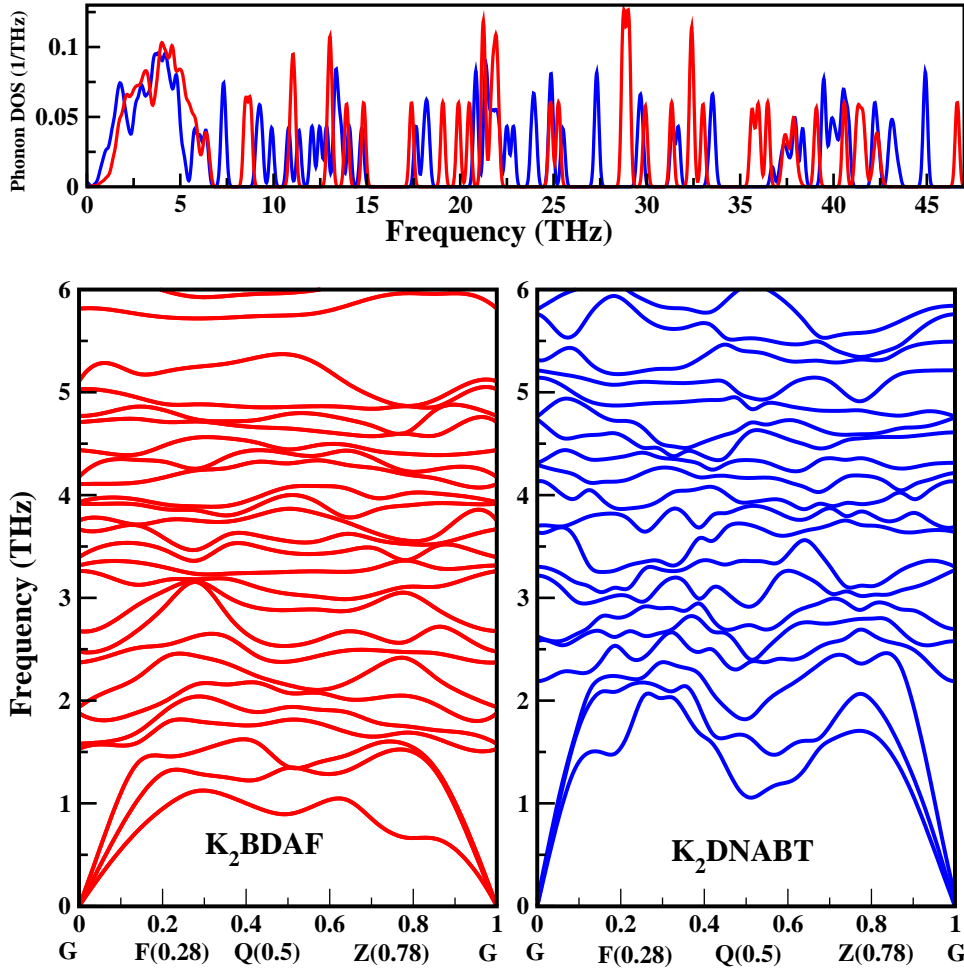


Figure 6.6: Calculated total phonon density of states (top) and phonon dispersion curves (bottom) of K_2BDAF (red in color), K_2DNABT (blue in color) crystals optimized at G06 level, along the brillouin zone path $G (0 0 0) \rightarrow F (0 0.5 0) \rightarrow Q (0 0.5 0.5) \rightarrow Z (0 0 0.5) \rightarrow G (0 0 0)$

atures, which clearly tell that K_2BDAF is more stable material than K_2DNABT . The Debye temperature plot shows more or less similar behaviour at high temperatures. Whereas in low temperatures dips are found at 25 K for K_2DNABT , at 15 K for K_2BDAF . The corresponding Debye temperatures are found to be 327.4 K and 258.9 K. Since there are no experimental or theoretical studies reported till date we could not compare our results. Overall, the Debye temperature

analysis brief that, the highest temperature due to a single normal vibration for K_2DNABT is 68.5 K higher than K_2BDAF . The lower heat capacity and higher Debye temperature values clearly tell that K_2DNABT is relatively less stable than K_2BDAF . Thus our results and analysis gives clear analogy for the differences in the experimentally obtained decomposition temperatures of K_2DNABT (491 K), K_2BDAF (502 K).

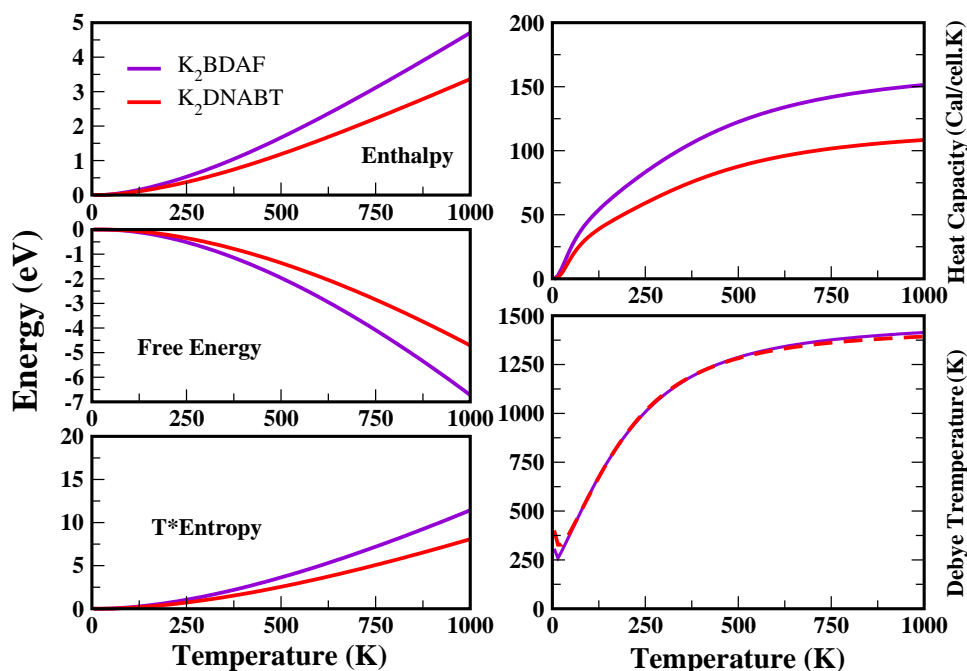


Figure 6.7: Calculated thermodynamic properties (Enthalpy (H), Entropy (S_V), Free energy (F), Heat capacity (C_V), $\Theta(V)$ Debye temperature) of K_2BDAF , K_2DNABT up to 1000K temperature at G06 level.

6.3.4 Electronic band structure and density of states

It is known that bond dissociation energy of NO_2 group calculated from the isolated molecule along with single crystal band gap value explains the trend of impact sensitivity [70]. Therefore, accurate prediction of electronic band of energetic materials plays a crucial role in understanding their photo decomposition process. Many impact sensitivity versus electronic band gap correlation studies

of explosives are reported in the literature with a conclusion that, lower band gap materials are highly sensitive to impact [70, 71]. In view of these important correlations, we have calculated the electronic band structure of K₂BDAF using different exchange-correlation functionals (LDA, GGA(PBE, PBEsol), default TB-mBJ, new parameterized TB-mBJ) to predict the accurate band gap using full-potential linearized augmented plane wave (FP-LAPW) method [42]. The obtained band gap values are shown in Table 6.9. It is clear from results that, band gap values with LDA, PBE and PBEsol are showing < 2 eV magnitude, whereas the present TB-mBJ (default and new parameterized) and previously reported TB-mBJ results (2.08 eV obtained with PAW method in VASP [43]) shows band gap value > 2 eV. It is well known that, normally DFT-LDA, DFT-GGA underestimate the band gap values due to their locality, energy independence with electron addition or removal and incorrect long wavelength limit. Whereas, new TB-mBJ potential is known to predict accurate band gaps with similar accuracy as expensive HSE or GW functionals with less computational cost [66]. Hence, it is evident from the present study that, the band of K₂BDAF lies around 3 eV. We have compared the obtained band gap results with the other iso-structural primary explosives like triclinic-K₂DNABT (PBE(2.87),TB-mBJ (3.57)) [72]; orthorhombic azides like α -Pb(N₃)₂ (2.42 eV), Cu(N₃)₂ (2.41 eV), α -Hg(N₃)₂ (2.41 eV) at GGA(PW91) level[19] and with novel organic nonlinear optical crystals like monoclinic-DAST (experiment \rightarrow 2.33, DFT-D2 \rightarrow 1.47), monoclinic-DSMS (experiment \rightarrow 2.33, DFT-D2 \rightarrow 1.55) [73]. The results reveal that, the present obtained TB-mBJ band gap results are found to occur within the experimental values range of K₂BDAF iso-structural compounds.

The observed PBE, TB-mBJ band gap value differences (~ 1.2 eV) between K₂BDAF and K₂DNABT in turn tell that, K₂BDAF is relatively more sensitive to the light. This conclusion is contradicting with the experimental impact sensitivity observations. To address this issue, we have calculated the TB-mBJ electronic band structure in the first Brillouin zone along high symmetry path $\Gamma (0, 0, 0) \rightarrow$

Z (0, 0, 0.5) \rightarrow Y (0, 0.5, 0) \rightarrow X (0.5, 0, 0) \rightarrow V (0.5, 0.5, 0) \rightarrow U (0.5, 0, 0.5) \rightarrow T (0, 0.5, 0.5) \rightarrow R (0.5, 0.5, 0.5) \rightarrow Γ (0, 0, 0) and the plot is shown in Fig 6.8(b). It is clear from the obtained electronic band structure that, band gap is found to occur along R to V high symmetry direction (indirect band gap). Whereas, in case of K₂DNABT the band gap occurrence was direct (along B). Which informs that, it is easy to excite electrons from valence band to conduction band in K₂DNABT, whereas in K₂BDAF one needs to input sufficient momentum transfer to excite the electrons. Thus, K₂DNABT is becoming sensitive than K₂BDAF. Moreover, as both the studied explosives crystallize in noncentrosymmetric space group, their recombination output in terms of direct and indirect band gap will show strong impact on the optical stability of the explosive. Since K₂DNABT possess direct band gap, the conversion efficiency will be more due to radiative transitions, whereas the possible non radiative electron-hole recombination in indirect band gap crystal K₂BDAF consequently reduces the lifetime of the material in radiation environment. But, from the phonon dispersion thermal conductivity guess, K₂BDAF should be more stable by transferring the generated heat to the surroundings efficiently than K₂DNABT. Since this conclusion is also contradicting with the impact sensitivity analysis and we addressed this issue in terms of linear optical properties in the next section.

Further, in order to analyse the electrons excitation and bonding mechanism, we have calculated the total and partial density of states (PDOS) of each element. The resultant spectra are shown in Fig 6.8(a). It is clear from the DOS plots that, hybridization of DOS of all the atom with other atoms are found to be very strong. Which confirms that, the present studied compound is more covalent in nature and strong ionic nature is observed via K1-O3 bond. The same result is also confirmed from charge density plots as shown in Fig 6.8(c). We observed that, there is considerable charge sharing between all the atoms, and was little less for K1-O3 bond, which clearly indicates the presence of ionic nature in the studied compound. This analysis is consistent with the BEC analysis as discussed

in previous section. It can be seen from Fig 6.8(a) that, in top of the valence band near the Fermi level C1-p states > O1,O2,O3,O4,O5-p states > N1,N2,N3,N5 -p states are more dominating. Whereas, C2-p, O5-p, N4-p, K1-p show lowest contribution near the Fermi level. Therefore, C, O, N p-electrons will easily get transfer from valence band to conduction band and participate in the optical response.

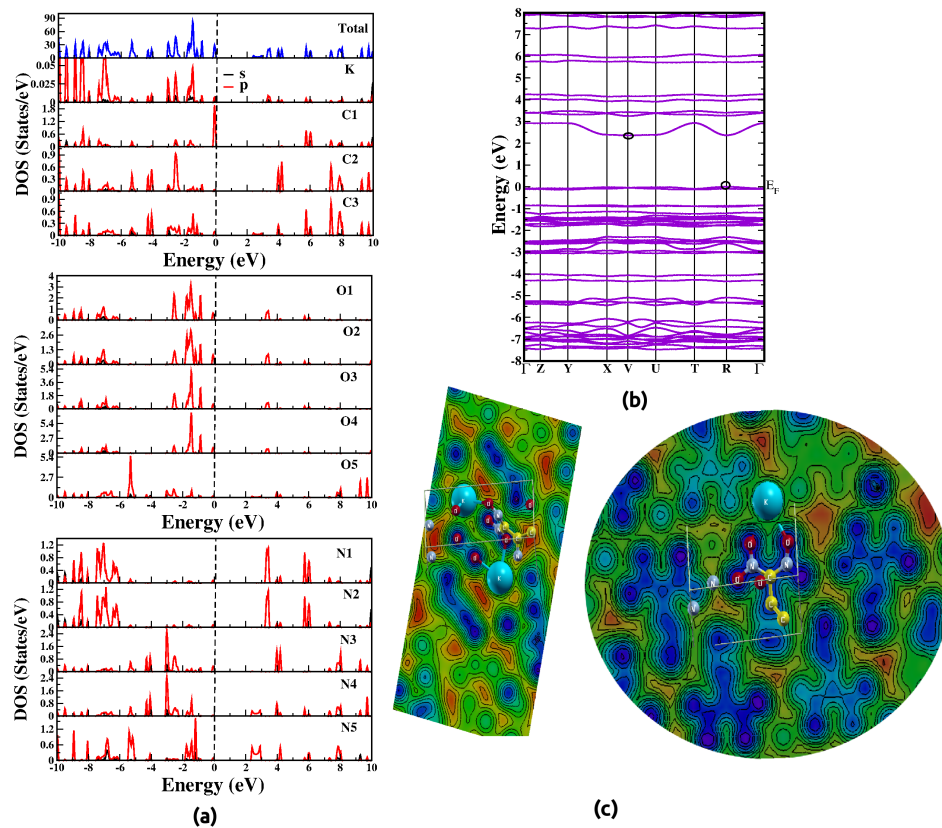


Figure 6.8: Calculated (a) partial density of states (DOS), (b) electronic band structure, (c) electron charge density maps of K_2BDAF crystal structure optimized at TB-mBJ level.

Table 6.9: Calculated energy band gaps of K₂BDAF at experimental crystal structure volume.

Functional	LDA	PBE	PBEsol	TB-mBJ	Parameter fixed-TB-mBJ
Band gap (eV)	1.515	1.573	1.544	2.374	3.030

6.3.5 Linear optical properties and birefringence

As a further step we have calculated the linear optical properties of K₂BDAF and K₂DNABT at TB-mBJ level of accuracy using FP-LAPW. The calculated plots of complex dielectric function (ϵ), absorption spectra (α), refractive index (n) spectra with respect to the photon energy are shown in Fig 6.9. For both the studied explosives, the curves of real part of dielectric function ($\epsilon_1(\omega)$) present in all directions namely ϵ_{xx} , ϵ_{yy} , ϵ_{zz} (see Fig 6.9) and shows large optical anisotropies with respect to photon energy, especially in the low energy region. For the studied crystals, the static dielectric constant values along different directions shows the following trend: (1)K₂BDAF: zz (high) > xx (mid) > yy (low); (2)K₂DNABT: yy (high) > xx (mid) > zz (low). In addition, from K₂BDAF to K₂DNABT the anisotropies decreased along z direction, whereas along x and y directions increased. However, the magnitude of ϵ in all three directions remains positive from 0-12 eV range in case of K₂DNABT. In case of K₂BDAF, ϵ_{xx} (around 3.8 eV), ϵ_{yy} (around 4.1 eV) becomes negative, becomes positive again after 5.5 eV. Whereas, ϵ_{xx} of K₂BDAF remains as positive in the entire energy window (0-12 eV). In low energy (0-4 eV) region, the fluctuations in the real part of dielectric function are more for K₂BDAF than K₂DNABT. As the photon energy increases, these fluctuations become almost zero for K₂BDAF, whereas for K₂DNABT fluctuations remain positive. Importantly, for K₂BDAF: all three components ϵ_{xx} , ϵ_{yy} , ϵ_{zz} values approaches their lowest values (~ 1) at 6 eV and remains almost same with further increase in photon energy. But, in case of K₂DNABT, these values are more fluctuating and ended up to ~ 2 even at high energies. We further calculated the imaginary part of dielectric function ($\epsilon_2(\omega)$) for both the crystals

Table 6.10: Linear optical properties such as absorption coefficient ($\times 10^4 \text{ cm}^{-1}$), refractive indices and birefringence of K₂BDAF and K₂DNABT

$\epsilon_i^{[100]}(\omega)$	$\epsilon_i^{[010]}(\omega)$	$\epsilon_i^{[001]}(\omega)$	$\alpha^{[100]}(\omega)$	$\alpha^{[010]}(\omega)$	$\alpha^{[001]}(\omega)$	n_x	n_y	n_z	$\Delta n (n_x - n_y)$	@	Δn	Δn
2.59	2.91	1.91	6.8	95.98	3.54	1.61200	1.70757	1.3821	0.32544	Static	0.32544	0.25553
1.95	1.91	2.68	38.25	85.75	15.60	1.39692	1.38268	1.63821	0.25553	1064 nm	0.36519	0.25964
										532 nm	0.58501	0.27194

which represent the absorption of the material using Kramers-Kronig relations as implemented in WIEN2K [42] and the results are shown in Fig 6.9. The static values of $\epsilon_1(\omega)$, $\alpha(\omega)$, $n(\omega)$ in xx, yy, zz directions and Δn value at static, 1064 nm, 532 nm are tabulated in Table 6.10 for further reference. The results show that, from K₂DNABT to K₂BDAF (1) the real part of dielectric constant reduced along zz-direction and increased along xx, yy directions. (2) Absorption coefficient decreased in xx, zz directions and increased in yy direction. (3) Birefringence increased at static, 1064 nm and 532 nm.

It is clear from the $\epsilon_2(\omega)$ spectra of K₂BDAF, K₂DNABT explosives that, the basic absorption is starting at 3.0 eV, 3.57 eV which are consistent with the obtained and reported band gap values. Similar to complex $\epsilon(\omega)$, the absorption and refractive index spectra also show a considerable anisotropy in all the crystallographic directions for both the crystals. The absorption spectra of K₂BDAF in the low energy region shows the first high intensity absorption peak at 3.0 eV in yy direction, at 3.5 eV in zz direction, at 4.2 eV in xx direction. The magnitude of absorption of K₂BDAF is found to decrease in the following order: (1) up to 7eV: yy \rightarrow zz \rightarrow xx, (2) up to 10eV: xx \rightarrow yy \rightarrow zz, (3) after 10eV: zz \rightarrow yy \rightarrow xx. The absorption spectra of K₂DNABT in the low energy region shows the first absorption peak at 4.0 eV in zz direction, at 4.5 eV in yy direction, at 4.3 eV in xx direction. The magnitude of absorption of K₂DNABT is found to decrease in the following order: (1) up to 5eV: yy \rightarrow xx \rightarrow zz, (2) up to 11eV: zz \rightarrow xx \rightarrow yy, (3) after 12eV: zz \rightarrow yy \rightarrow xx. Overall, from K₂DNABT to K₂BDAF the optical absorption anisotropy increased. The highest absorption peaks lies at 3.5 eV along yy direction for K₂BDAF, and for K₂DNABT it lies around 6 eV along zz

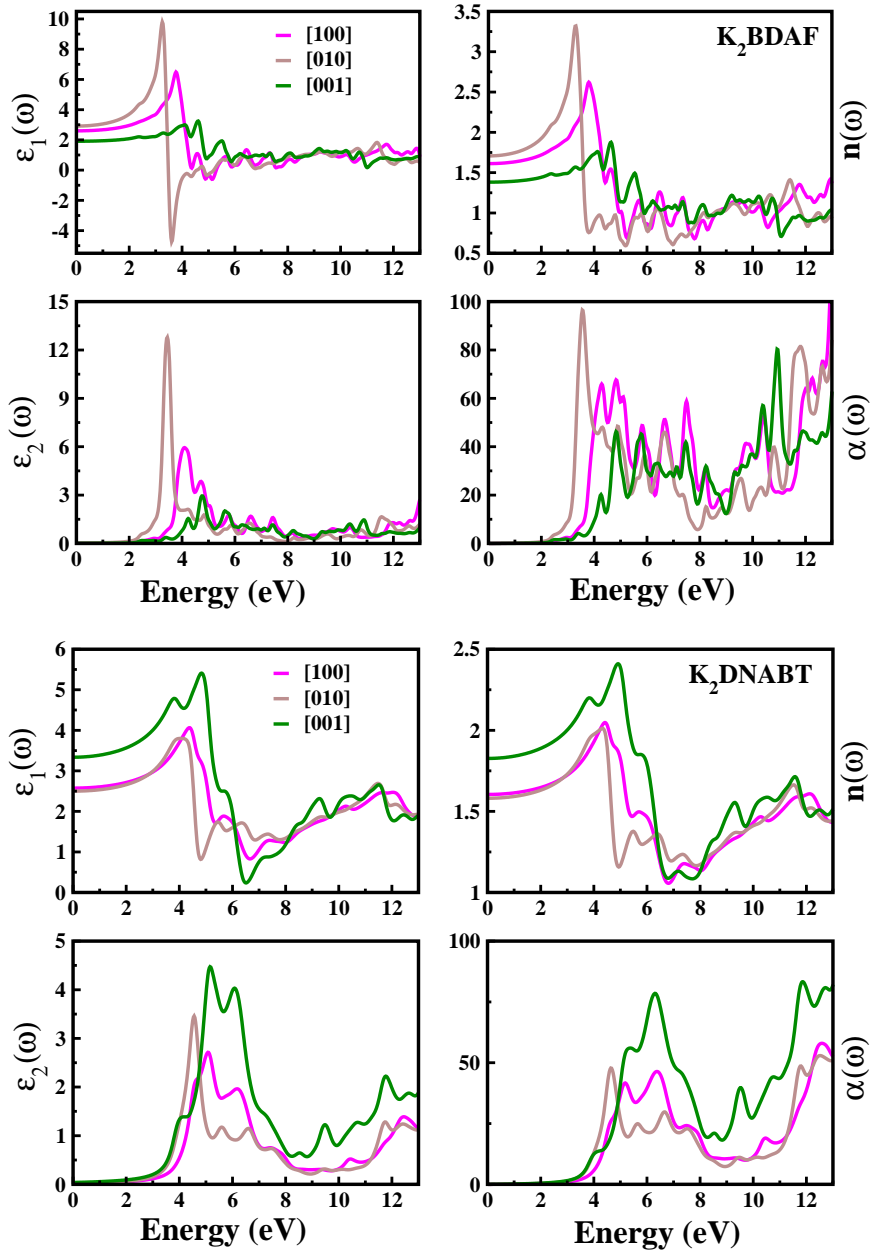


Figure 6.9: Calculated linear optical properties (real and imaginary parts of complex dielectric function; refractive index and absorption spectra) of K_2BDAF crystal structure at TB-mBJ level.

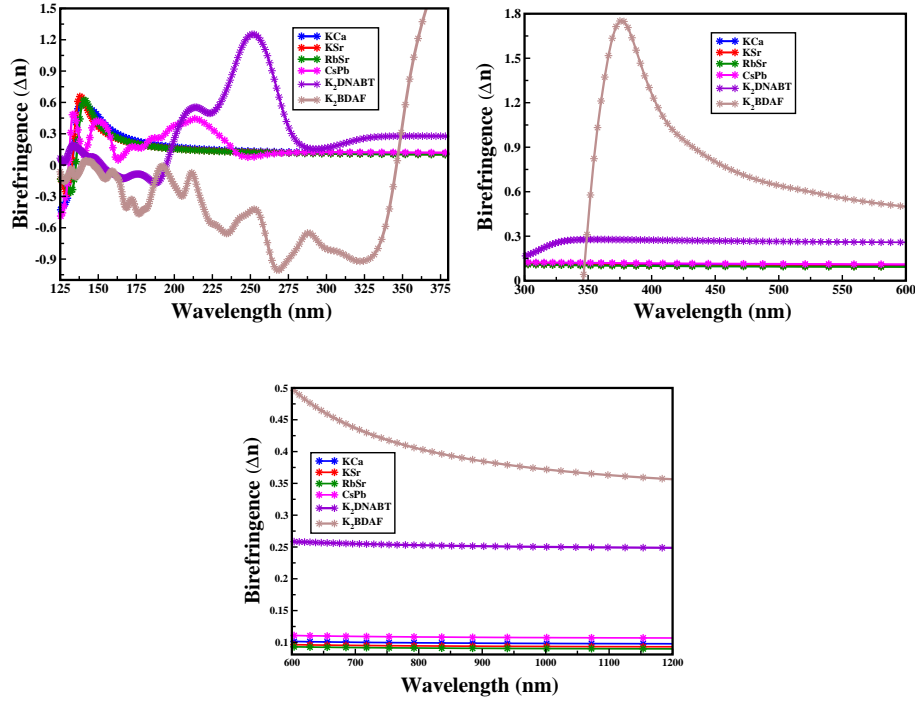


Figure 6.10: Calculated Birefringence of K₂BDAF and K₂DNABT at experimental crystal structure volume. Results are compared with KCaCO₃F, KSrCO₃F, RbSrCO₃F and CsPbCO₃F (with and without spin-orbit effects)[44].

direction. Similar anisotropic behaviour is also observed in the refractive index spectra and this is increased from K₂DNABT to K₂BDAF. The static values of refractive index (see Table 6.10) show the following trend (1) for K₂BDAF: $n_y > n_x > n_z$ (2) for K₂DNABT : $n_z > n_x > n_y$.

As a further step, we have calculated the birefringence of K₂BDAF with respect to wavelength and compared the results with recent novel SHG carbonate

Table 6.11: The change in Born Effective charges along y-z (for K₂BDAF), z-y (for K₂DNABT) directions of different atoms.

Atom	K1	O1	O2	O3	O4	O5	N1	N2	N3	N4	N5	-	C1	C2	C3
Δq_{y-z}	0.15207	0.37254	-1.06651	0.55195	-1.16813	-0.25696	1.55069	1.53083	-0.04994	0.59676	0.12895	-	-1.50755	-0.76362	-0.07108
Atom	K1	O1	O2	-	-	-	N1	N2	N3	N4	N5	N6	C1	-	-
Δq_{z-y}	0.05648	-0.31982	-1.84613	-	-	-	0.14051	0.60689	-0.32409	-0.14588	-0.71607	2.75982	-0.21173	-	-

fluoride materials. Since K_2BDAF crystallize in triclinic crystal structure, therefore it is supposed to be a biaxial nonlinear crystal with two birefringence values. We have taken the maximum Δn ($n_{max} - n_{min}$) value among the two obtained birefringence values with respect to the wavelength. The calculated maximum birefringence value plots for K_2DNABT and K_2BDAF in different wavelength regions (125 nm - 375 nm; 300 nm - 600 nm; 600 nm - 1200 nm) are shown in Fig 6.10. It is clear from the plots that, the birefringence of K_2BDAF is found to be much higher than K_2DNABT in 1200 nm - 350 nm wavelength window and becomes negative after 350 nm. Whereas, the Δn of K_2DNABT becomes negative around 190 nm. Because of the increase in the low wavelength limit of Δn from K_2BDAF (350 nm) to K_2DNABT (190 nm), it will become difficult to achieve phase matching condition to have good conversion efficiency in K_2BDAF after 350 nm. As we know, if the material is less transparent to the generated second harmonic wavelength, then this newly generated wavelength may heat up the system and ends up in damaging the crystal. In this point of view, the high absorption coefficient, high refractive index and low birefringence (see Fig 6.10) of K_2DNABT at 532 nm (2.3 eV) (see Table 6.10) leads to produce difficulties in achieving the phase matching condition. Moreover, due to low birefringence value of K_2DNABT over K_2BDAF with respect to any incident wavelength, K_2DNABT will become more sensitive to light than K_2BDAF . We further compared our results with recently reported promising nonlinear optical materials like DAST, DSTMS. Importantly, we noticed that, K_2BDAF is having almost similar birefringence value when compared to DAST (0.39, 0.55, 0.64) [73] and DSTMS (0.45, 0.63) [73]. With increased curiosity and to have a different comparison, we have calculated the birefringence (Δn) values for $KCaCO_3F$, $KSrCO_3F$, $RbSrCO_3F$, $CsPbCO_3F$ crystals using our previously reported results [74] and resultant spectra are shown along with K_2DNABT and K_2BDAF in Fig 6.10. It is clear from the plots that, the birefringence of K_2BDAF and K_2DNABT is much higher than all the carbonate fluoride nonlinear crystals (KCa (0.09), KSr (0.09),

RbSr (0.08), CsPb (0.10)). Hence, from all the above observations it is clear that the studied primary explosives are showing excellent birefringence than many well known promising NLO materials. Especially at 375 nm K₂BDAF crystal is showing the birefringence value 1.8 which is equal to the $\Delta n(at375nm)$ of DAST, $\Delta n(at375nm)$ of DSTMS and 3 times that of DAST- $\Delta n(0)$ and DSTMS- $\Delta n(0)$. In order to know the contributions of different atoms to the huge birefringence value [75], we have calculated the BEC differences of all the constituent atoms i.e. (1) K1, O1-O5, N1-N5, C1-C3 atoms for K₂BDAF (along y-z direction) and (2) K1, O1, O2, N1-N6, C1 atoms for K₂DNABT (along z-y direction). The results for both the studied crystals are tabulated in Table 6.11. It is clear from the results that, in case of K₂BDAF the positive contribution to the birefringence is obtained from K1, O1, O3, N1, N2, N4, N5 atoms. Whereas the O2, O4, O5, N3, C1, C2, C3 are showing negative contribution to the birefringence. In case of K₂DNABT, K1, N1, N2, N6 are showing positive contribution and O1, O2, N3, N4, N5, C1 are showing negative contribution to the total birefringence. It is also important to observe that, the positive contribution from K1 (0.095), O1 (0.692), O2 (0.779), N1 (1.410), N2 (0.923), N3 (0.274), N4 (0.742), N5 (0.845) atoms increased and negative contribution from C1 is increased by 1.295. In conclusion, from K₂DNABT to K₂BDAF the positive contribution to the birefringence from the terminal NO₂ nitro groups and K-O bond is increased, whereas due to carbon atom a slight negative contribution is observed from the tetrazole ring structure.

6.4 Conclusions

The knowledge about vibrational, electronic and optical properties of a noncentrosymmetric explosive materials plays a crucial role in exploring the phase transition mechanism, stand-off detection of HEM residues on the surfaces and interfaces. In the present study, we have explored the role of crystal structure, chemical composition in predicting the structural, mechanical (single and polycrystalline

properties), dynamical (vibrational IR-spectra analysis, born effective charges, phonon dispersion spectra, thermodynamic properties), electronic and linear optical properties of newly synthesized two noncentrosymmetric primary explosives Potassium 4,4'-Bis (dinitromethyl)-3,3'-azofurazanate (K_2 BDAF), Potassium 1,1'-Dinitramino-5,5'-bistetrazolate (K_2 DNABT) using density functional theory simulations. We correlated all our results with experimentally reported impact, friction sensitivity parameters and successfully explained the reasons behind the high sensitivity of K_2 DNABT. All the calculated properties clearly suggest that, K_2 BDAF is found to be more stable, more polarizable and easily detectable than K_2 DNABT. The calculated optical properties (low dielectric constant, high birefringence value) suggest that, these studied organic explosive materials are showing better features for NLO applications as well known organic DAST and DSTMS crystals. We explained the reasons for this kind of optical response for the studied explosive materials. Overall, our results are good in agreement with experimentally reported sensitivity trends. Studies on the nonlinear optical $\chi_{ijk}^{(2)}(-2\omega;\omega,\omega)$ dispersion of both explosive single crystals and comparison of these properties with well known NLO materials are most important to explain the surface and interface detection studies and the same will be reported in near future.

References

- [1] P. S. Halasyamani and K. R. Poeppelmeier, *Chem. Mater.*, **10**, 2753 (1998).
- [2] P. A. Franken, A. E. Hill, C. W. Peters and G. Weinreich, *Phys. Rev. Lett.*, **7**, 118 (1961).
- [3] L. Kang, Z. Lin, J. Qin and C. Chen, *Sci. Rep.*, **3**, 1366 (2013).
- [4] P. C. Ray, *Chem. Rev.*, **110**, 5332 (2010).
- [5] Y. Wang and S. Pan, *Coord. Chem. Rev.*, **323**, 15 (2016).
- [6] S. Suresh, A. Ramanand, D. Jayaraman and P. Mani, *Rev. Adv. Mater. Sci.*, **30**, 175 (2012).
- [7] C. Chen, T. Sasaki, R. Li, Y. Wu, Z. Lin, Y. Mori, Z. Hu, J. Wang, S. Uda, M. Yoshimura and Y. Kaneda, *Nonlinear Optical Borate Crystals. 2012* Wiley-VCH Verlag Co. KGaA, Boschstr. 12, 69469 Weinheim, Germany. ISBN: 978-3-527-41009-5.
- [8] T. Thao Tran, J. Young, J. M. Rondinelli and P. Shiv Halasyamani, *J. Am. Chem. Soc.*, **139**, 1285 (2017).
- [9] Y. Song, M. Luo, C. Lin and N. Ye, *Chem. Mater.*, **29**, 896 (2017).
- [10] C.-L. Hu and J.-G. Mao, *Coord. Chem. Rev.*, **288**, 288, 1 (2015).
- [11] G. Zou, L. Huang, N. Ye, C. Lin, W. Cheng and H. Huang, *J. Am. Chem. Soc.*, **135**, 18560 (2013).
- [12] M. Abudourehman, L. Wang, X. Zhang, H. Yu, Z. Yang, C. Lei, J. Han and S. Pan, *Inorg. Chem.*, **54**, 4138 (2015).
- [13] T. -Y. Chang, B. -P. Yang, C. -L. Hu, D. Yan and J. -G. Mao, *Crys. Growth Des.*, **17**, 4984 (2017).

- [14] F.Kong, C. -L. Hu, M. -L. Liang and J. -G. Mao, *Inorg. Chem.*, **55**, 55, 948 (2016).
- [15] S.Marder, J.Perry and W.Schaefer, *Science*, **245**, 626 (1989).
- [16] M.Jazbinsek, L.Mutter and P.Gunter, *IEEE J. Sel. Top. Quantum Electron.*, **14**, 1298 (2008).
- [17] B.Ruiz, Z.Yang, V.Gramlich, M.Jazbinsek, P.Gunter, *J. Mater. Chem.*, **16**, 2839 (2006).
- [18] K.Oyler, *Green Primary Explosives. Green Energetic Materials*, John Wiley & Sons, Ltd, 103-132 (2014).
- [19] W.Zhu and H.Xiao, *J. Phys. Chem. B*, **110**, 18196 (2006).
- [20] D.Fischer, Thomas M. Klapötke and J.Stierstorfer, *Angew. Chem. Int. Ed.*, **53**, 8172 (2014).
- [21] Y.Tang, C.He, L. A.Mitchell, D. A. Parrish and J. M. Shreeve, *Angew. Chem. Int. Ed.*, **55**, 5565 (2016).
- [22] B. F. Henson, B. W. Asay, R. K.Sander, S. F. Son, J. M. Robinson and P. M. Dickson, *Phys. Rev. Lett.*, **82**, 1213 (1999).
- [23] L.Smilowitz, B. F.Henson, B. W. Asay, P. M. Dickson, *J. Chem. Phys.*, **117**, 3789 (2002).
- [24] L. Smilowitz, B. F.Henson, M.Greenfield, A.Sas, B. W.Asay and P. M. Dickson, *J. Chem. Phys.*, **121**, 5550 (2004).
- [25] H.Kim, A.Lagutchev, D. D. Dlott, *Propellants Explos. Pyrotech.*, **31**, 116 (2006).
- [26] J. Yinon, *Counter-terrorist Detection Techniques of Explosives*, Elsevier, UK., 2007, 279-362. ISBN: 978-0-444-52204-7.

- [27] M. C. Payne, M. P. Teter, D. C. Allan, T. A. Arias and J. D. Joannopoulos, *Rev. Mod. Phys.*, **64**, 1045 (1992).
- [28] M. D. Segall, P. J. D. Lindan, M. J. Probert, C. J. Pickard, P. J. Hasnip, S. J. Clark and M. C. Payne, *J. Phys. Cond. Matter*, **14**, 2717 (2002).
- [29] T. H. Fischer and J. Almlof, *J. Phys. Chem.*, **96**, 9768 (1992).
- [30] H. J. Monkhorst and J. D. Pack, *Phys. Rev. B*, **13**, 5188 (1976).
- [31] D. Vanderbilt, *Phys. Rev. B*, **41**, 7892 (1990).
- [32] D. M. Ceperley and B. J. Alder, *Phys. Rev. Lett.*, **45**, 566 (1980).
- [33] J. P. Perdew and A. Zunger, *Phys. Rev. B*, **23**, 5048 (1981).
- [34] J. P. Perdew and Y. Wang, *Phys. Rev. B*, **45**, 13244 (1992).
- [35] J. P. Perdew, K. Burke and M. Ernzerhof, *Phys. Rev. Lett.*, **77**, 3865 (1996).
- [36] F. Ortmann, F. Bechstedt and W. G. Schmidt, *Phys. Rev. B*, **73**, 205101 (2006).
- [37] D. R. Hamann, M. Schlüter and C. Chiang, *Phys. Rev. Lett.*, **43**, 1494 (1979).
- [38] S. Baroni, S. de Gironcoli, A. Dal Corso and P. Giannozzi, *Rev. Mod. Phys.*, **73**, 515 (2001).
- [39] E. B. Wilson, J. C. Decius and P. C. Cross, *Molecular Vibrations: the theory of infrared and Raman vibrational spectra*, McGraw-Hill, New York, 1955.
- [40] X. Gonze, *Phys. Rev. B*, **55**, 10337 (1997).
- [41] M. A. Blanco, E. Francisco and V. Luaña, *Comput. Phys. Commun.*, **158**, 57 (2004).

- [42] P. Blaha, K.Schwarz, G. K. H. Madsen, D.Kvasnicka and J.Luitz, *WIEN2K, An Augmented Plane Wave + Local Orbitals Program for Calculating Crystal Properties* Karlheinz Schwarz, Techn. Universität Wien, Austria,2001. ISBN 3-9501031-1-2.
- [43] B. Moses Abraham, N. Yedukondalu and G. Vaitheeswaran, Poster presented at National Conference on Recent trends in Condensed Matter Physics, at Bose Institute, Kolkatta, Oct-31 to Nov-3 (2017).
- [44] E. N. Rao, G. Vaitheeswaran, A. H. Reshak and S. Auluck, *Phys. Chem. Chem. Phys.*, **19**, 31255 (2017).
- [45] D.Koller, F.Tran and P. Blaha, *Phys. Rev. B*, **85**, 155109 (2012).
- [46] J.P.Perdew, A.Ruzsinszky, G.b.I.Csonka, O.A.Vydrov, G.E.Scuseria, L.A. Constantin, X. Zhou and K.Burke, *Phys. Rev. Lett.*, **102**, 039902 (2009).
- [47] F. Tran and P.Blaha, *Phys. Rev. Lett.*, **102**, 226401 (2009).
- [48] J. J. Haycraft, L. L.Stevens and C. J.Eckhardt, *J. Chem. Phys.*, **124**, 024712 (2006).
- [49] J. M. Brown, E. H.Abramson and R. J. Angel, *Phys. Chem. Miner.*, **33**, 256 (2006).
- [50] F. l. Mouhat and F. o.-X. Coudert, *Phys. Rev. B*, **90**, 224104 (2014).
- [51] S.Appalakondaiah, G.Vaitheeswaran and S. Lebègue, *Chem. Phys. Lett.*, **605**, 10 (2014).
- [52] D. I. A. Millar, *Energetic materials at extreme conditions, Springer Theses* 2012.
- [53] C. E. Weir, S. Block and G. J.Piermarini, *J. Chem. Phys.*, **53**, 4265 (1970).

- [54] W. H. Andersen, *Propellants Explos. Pyro.*, **6**, 17 (1981).
- [55] J.K. D. Verma and B.D. Nag, *J. Phys. Soc. Jpn.*, **20**, 635 (1965).
- [56] R.Hill, *Proc. Phys. Soc. Section A*, **65**, 349 (1952).
- [57] C. F.Yu, H. C. Cheng and W. H. Chen, *ICEP 2016 Proc.*, 362 (2016).
- [58] S. F.Pugh, *The London, Edinburgh, and Dublin Philosophical Magazine and Journal of Science*, **45**, 823 (1954).
- [59] R S. Igor and L I. Alexander, *J. Phys. Cond. Matter* **20**, 415218 (2008).
- [60] J. Haines, J. M.Léger and G.Bocquillon, *Annu. Rev. Mater. Res.*, **31**, 1 (2001).
- [61] S. I. Ranganathan and M.Ostoja-Starzewski, *Phys. Rev. Lett.*, **101**, 055504 (2008).
- [62] S. J. P.Palmer and J. E.Field, *Proc. Royal Soc. Lond. Series A.*, **383**, 399 (1982).
- [63] K.Jagannathan, S.Kalainathan and T.Gnanasekaran, *Mater. Lett.*, **61**, 4485 (2007).
- [64] E.N.Rao, G.Vaitheeswaran, A. H. Reshak and S.Auluck, *RSC Adv.*, **6**, 99885 (2016).
- [65] T.Fang and J. C. Lambropoulos, *J. Am. Ceram. Soc.*, **85**, 174 (2002).
- [66] S.Kumar, S.Pandey and S.Auluk, *Adv. OptoElectron. Mat. (AOM)*, **2**, 10 (2014).
- [67] P.Ravindran, R. Vidya, A. Kjekshus, H.Fjellvåg and O.Eriksson, *Phys. Rev. B*, **74**, 224412 (2006).
- [68] J. F. Federici, B.Schulkin, F.Huang, D.Gary, R.Barat, F.Oliveira and D.Zimdars, *Semicond. Sci. Technol.*, **20**, S266 (2005).

-
- [69] P. D. Cunningham and L. M. Hayden, *Opt. Express*, **18**, 23620 (2010).
- [70] H.Zhang, F.Cheung, F. Zhao and X. -L. Cheng, *Int. J. Quantum Chem.*, **109**, 1547 (2009).
- [71] W. Zhu and H.Xiao, *Structural Chemistry*, **21**, 847 (2010).
- [72] N.Yedukondalu and G.Vaitheeswaran, *J. Chem. Phys.*, **143**, 064508 (2015).
- [73] R. -Z. Wu, Z.-X. Fang, P.Liu, Q. -Z. Cao, M. Qiu, Y.Li, W. -K.Chen, X.Huang and Y. -F.Zhang, *Acta Physico-Chimica Sinica*, **29**, 2534 (2013).
- [74] E. Narsimha Rao, S.Appalakondaiah, N.Yedukondalu and G.Vaitheeswaran, *J. Solid State Chem.*, **212**, 171 (2014).
- [75] Q.Jing, G.Yang, J.Hou, M.Sun and H.Cao, *J. Solid State Chem.*, **244**, 69 (2016).

Summary and future scope

7.1 Summary

In this chapter, we summarise the crucial outcomes of the thesis which are believed to show some good impact on the research community of understanding nonlinear optical materials development. As we mentioned in motivation chapter, the first aim of thesis is to understand structure-property correlations of various nonlinear optical materials and role of density functional theory functionals in predicting the various ground state properties. The second aim of thesis is to explore structure-property correlations of noncentrosymmetric green high energy materials. Since there are very less number of experimental & theoretical reports available on the nonlinear optical responses and applications of explosive materials in the literature, based on these expertise acquired from the first part of thesis we focused on exploring the nonlinear applications of HEM's using density functional theory simulations. We further extended our analysis on explaining the sensitivity correlations of these highly sensitive primary explosives.

In structural properties point of view, we observed that vdW interactions are dominant in RbCaCO_3F , CsCaCO_3F , CsPbCO_3F materials when compared with other studied compounds. The elastic constants and bulk modulus results reveal that all these materials except Lead carbonate are relatively harder than KH_2PO_4 (KDP) crystal and mechanically stable. All the studied materials are ductile in nature except KCaCO_3F (which is found brittle) and show considerable mechanical anisotropy. The vibrational properties study reveals that all these ma-

materials are dynamically stable at Brillouin zone centre. The charge density maps and BEC analysis reveal the mixed covalent-ionic bonding character of the compounds. This analysis also confirms the higher optical activity of CsPbCO_3F than other carbonates. The thermodynamic properties indicate that the lead based compound possess the highest thermal conductivity (32.430 W/m K) among the studied carbonate materials. The results also informs that the CsPbCO_3F could show better durability than LiNbO_3 , $\alpha\text{-SiO}_2$, CaCO_3 , $\text{Ba}_3\text{B}_6\text{O}_{12}$ hexagonal NLO materials. The structural, mechanical properties of K_2BDAF and K_2DNABT informs that, these crystals are mechanically stable and possess lower bulk modulus values K_2BDAF (18.91 GPa) $<$ K_2DNABT (22.4 GPa) than KDP and lead azide $\text{Pb}(\text{N}_3)_2$. The born effective charge (BEC), vibrational, thermodynamic and phonon dispersion studies reveal that, both the crystals are dynamically stable and K_2BDAF is found to be more polarizable and easily detectable than K_2DNABT . Both crystals possess better Debye temperature values than well known organic NLO material Urea (Debye: 135K ; Melting: 408K) and better heat capacity values than carbonate fluoride crystals.

In electronic properties point of view, these materials are wide band gap insulators with good birefringence values and found to be good phase matchable materials in UV and deep-UV regions. Our results confirm the presence of the large SOI in CsPbCO_3F compound and the splitting of Pb p-states is observed to show considerable effects on the electronic band gap and related optical properties. The calculated static birefringence of CsPbCO_3F is found to be larger than the other carbonate fluorides. From the Born effective charge (BEC) analysis we notice that, Cs atom shows negative contribution to total birefringence whereas Pb, C, F atoms show positive contribution. We have analysed the different possible electronic transitions contributing to the optical properties. The calculated nonlinear optical coefficients of CsPbCO_3F single crystal using the FP-LAPW method are found to be ($d_{11} = d_{12} = 4.35 \text{ pm/V}$ at 1064 nm) 11.2 times higher than d_{36} of KDP. Overall, from our present electronic properties results we can

say that CsPbCO₃F is a good phase matchable NLO material in the UV region among all the other carbonate fluorides. In case of metal organic NLO crystals, the K₂BDAF is found to be an indirect band gap material whereas K₂DNABT is direct band gap material. The density of states and charge density plots of these explosive materials describes that, both the crystals possess mixed covalent and ionic bonding nature and these results are consistent with BEC analysis. From the optical properties study, it is found that studied explosive materials have the lowest dielectric constant than DAST crystal and show similar birefringence as DAST and DSTMS nonlinear crystals. Overall, our results on K₂DNABT, K₂BDAF are in good agreement with the experimentally reported sensitivity data. The study of optical properties (low dielectric constant, high birefringence value) suggests that, these studied organic explosive materials are showing better features for NLO applications than best known organic DAST and DSTMS crystals.

7.2 Future scope

We successfully explained the reasons behind the experimentally reported sensitivity trends of explosive materials using the structure-property correlation studies. We strongly believe that these kinds of studies must be continued to build a database on explosive structure-sensitivities correlations with proper explanations. The easy way to do this is through density functional theory simulations. Especially, studies on the nonlinear optical $\chi_{ijk}^{(2)}(-2\omega;\omega,\omega)$ dispersion of noncentrosymmetric explosive single crystals and comparison of these properties with well known NLO materials are most important to design new efficient NLO crystals. We strongly believe based on the reading of available literature on organic, inorganic and semi-organic NLO materials and from our results on explosive materials that, one needs to initially understand the $\chi_{ijk}^{(2)}(-2\omega;\omega,\omega)$ dispersion of very active explosives and make them more and more stable by suitable doping mechanism. This can be done by other way also, like first take a explosive molecule

and explore its second harmonic generation capability at molecular level. Then in second step, one needs to repeat this study at solid state level using density functional theory simulations. Based on the outcome of the study on structure-property correlation studies of noncentrosymmetric explosives, it is possible to give new way to design a path breaking “highly nonlinear SHG material + stable explosive” for defence and optical technological applications. Later one can synthesise these theoretically proposed molecules or crystals. Our present thesis is the starting point in this direction. We continue this wonderful project till we invent an ideal crystal for NLO applications. Importantly, it is known from the literature that, the knowledge of structural, mechanical, vibrational, electronic, optical properties and origin of polarizability of a noncentrosymmetric explosive materials play a crucial role in understanding the phase transition & hot spot formation mechanism’s and to explore stand-off detection of high energy material (HEM) residues on the surfaces, interfaces. The studies in this point of view are very scarce in the literature. To explore more about the laser-explosive matter interactions for latest detection technologies [1], our proposed work is very important. Many suitable references are given in chapter 1 and 6.

References

- [1] P. M. Pellegrino, E. L. Holthoff and M. E. Farrell, *Laser-Based Optical Detection of Explosives*, CRC Press, Taylor Francis Group, LLC (2015).

List of publications

Publications included in the thesis

- [1] E. Narsimha Rao, S. Appalakondaiah, N. Yedukondalu, G. Vaitheeswaran, “Structural, electronic and optical properties of novel carbonate fluorides $ABCO_3F$ (A=K, Rb, Cs; B=Ca, Sr)”, *Journal of Solid State Chemistry*, **212**, 171-179 (2014). (IF:2.299)
- [2] E. Narsimha Rao, G. Vaitheeswaran, A. H. Reshak and S. Auluck, “Effect of lead and caesium on the mechanical, vibrational and thermodynamic properties of hexagonal fluorocarbonates: A comparative first principles study”, *RSC Advances*, **6**, 99885-99897 (2016). (IF:3.108)
- [3] E. Narsimha Rao, A. H. Reshak, S. Auluck and G. Vaitheeswaran, “Role of spin-orbit interaction on the nonlinear optical response of $CsPbCO_3F$ using DFT”, *Physical Chemistry Chemical Physics*, **19**, 31255-31266 (2017). (IF:4.123)
- [4] E. Narsimha Rao and G. Vaitheeswaran, 5. “Structure-property correlation studies of Potassium 4,4'-Bis (dinitromethyl)-3,3'-azofurazanate: A noncentrosymmetric primary explosive”, *to be submitted*.

Publications not included in the thesis

- [1] A. Parveen, E. Narsimha Rao, A. Bushnagar, P. Anees, G. Vaitheeswaran, “Topological behaviour of ternary non-symmorphic crystals $KZnX$ (X = P, As, Sb) under pressure and strain : A first principles study”, *Physical Chemistry Chemical Physics*, **20**, 5084-5102 (2018). (IF:4.123)
- [2] B. Adivaiah, E. Narsimha Rao, A. Parveen, G. Vaitheeswaran, “Lattice dynamics and thermodynamic properties of alkaline-earth metal nitrates

$M(\text{NO}_3)_2$ ($M = \text{Sr}, \text{Ba}$): A first principles study”, *Journal of Physics and Chemistry of Solids*, **122**, 268-277 (2018). (IF:2.048)

Publications under preparation

- [1] J.Prathap Kumar, **E. Narsimha Rao** and G.Vaitheeswaran , “Structure-optical isotropy correlations of alkali metal perchlorates MClO_4 ($M = \text{Li}, \text{Na}, \text{K}, \text{Rb}, \text{Cs}$)”. (submitted to *Journal of Physics: Condensed Matter*)(IF:2.617)
- [2] D. Ganesh, **E. Narsimha Rao**, M. Venkatesh, K. Nagarjuna, G. Vaitheeswaran, Akhila K. Sahoo, A.K. Chaudhary, “Effects of explosophoric groups on the optical response of Aryl Tetrazole Derivatives: A time domain terahertz, UV-visible spectroscopy and DFT study”.

s under preparation

f Physics and Chem-

aran , "Structure-
ClO₄ (M = Li, Na,
Matter)(IF:2.617)

Nagarjuna, G.
s of explosophoric
s: A time domain

"Structure-Property Correlation Studies of Carbonate Fluorides and Metal-Organic Energetic Solids"

by Narsimha Rao Elaprolu

Submission date: 09-Aug-2018 03:20PM (UTC+0530)
Submission ID: 988684889
File name: ENR-2018-PhD-Thesis-ACRHEM.pdf (10.94M)
Word count: 42845
Character count: 208729

Similarity Screening Done @ IGM Library
Sub ID: *DL/AL*
3/9/18
Librarian / DL / AL
IGM Library (UOH)

"Structure-Property Correlation Studies of Carbonate Fluorides and Metal-Organic Energetic Solids"

ORIGINALITY REPORT

34%
SIMILARITY INDEX

6%
INTERNET SOURCES

31%
PUBLICATIONS

20%
STUDENT PAPERS

PRIMARY SOURCES

1 Submitted to University of Hyderabad,
Hyderabad
Student Paper

13%

G. Vaitheeswaran

2 E. Narsimha Rao, S. Appalakondaiah, N. Yedukondalu, G. Vaitheeswaran. "Structural, electronic and optical properties of novel carbonate fluorides $ABCO_3F$ (A=K, Rb, Cs; B=Ca, Sr)", Journal of Solid State Chemistry, 2014
Publication

7%

G. Vaitheeswaran

3 E. Narsimha Rao, G. Vaitheeswaran, A. H. Reshak, S. Auluck. "Effect of lead and caesium on the mechanical, vibrational and thermodynamic properties of hexagonal fluorocarbonates: a comparative first principles study", RSC Advances, 2016
Publication

7%

G. Vaitheeswaran

G. S. Vaitheeswaran
Associate Professor
School of Physics
University of Hyderabad
Hyderabad-500 046 (TS) INDIA

4 Submitted to Indian Institute of Technology
Student Paper

1%

Similarity Screening Done @ IGM Library
Sub ID: 988684889
Sub DT: 09/08/2018
Librarian / DL / AL
IGM Library (UOH)
[Signature] 29/1/18

"Structure-Property Correlation Studies of Carbonate Fluorides and Metal-Organic Energetic Solids"

ORIGINALITY REPORT

40%	7%	36%	24%
SIMILARITY INDEX	INTERNET SOURCES	PUBLICATIONS	STUDENT PAPERS

PRIMARY SOURCES

- 1** Submitted to University of Hyderabad, Hyderabad
Student Paper **15%**
G. Vaitheeswaran
- 2** E. Narsimha Rao, S. Appalakondaiah, N. Yedukondalu, G. Vaitheeswaran. "Structural, electronic and optical properties of novel carbonate fluorides $ABCO_3F$ (A=K, Rb, Cs; B=Ca, Sr)", Journal of Solid State Chemistry, 2014
Publication **9%**
G. Vaitheeswaran
- 3** E. Narsimha Rao, G. Vaitheeswaran, A. H. Reshak, S. Auluck. "Effect of lead and caesium on the mechanical, vibrational and thermodynamic properties of hexagonal fluorocarbonates: a comparative first principles study", RSC Advances, 2016
Publication **8%**
G. Vaitheeswaran
G. S. Vaitheeswaran
Associate Professor
School of Physics
University of Hyderabad
Hyderabad-500 046 (TS) INDIA
- 4** Submitted to Indian Institute of Technology
Student Paper **1%**

Similarity Screening Done @ IGM Library
Sub ID: 988684889
SubDt: 09/08/2018
Librarian / DL / AL
IGM Library (UOH)
[Signature]

UNIVERSITY OF HYDERABAD
School of Physics
Advanced Centre of Research in High Energy Materials (ACRHEM)



Dr. G. S. Vaitheeswaran
Associate Professor

03rd September 2018

Declaration

This is to certify that the Ph.D thesis entitled "Structure-Property Correlation Studies of Carbonate Fluorides and Metal-Organic Energetic Solids" work done by Elaprolu. Narsimha Rao, Reg. No:10ACPP21, under my guidance. The plagiarism originality report shows 15% under the student paper repository submitted to the University of Hyderabad. This 15% work belongs to the scholars research work as part of this thesis.

Thanking You.

Yours sincerely,

A handwritten signature in blue ink that reads 'G. Vaitheeswaran'.

(Dr. G.S. Vaitheeswaran).

Dr. G.S. Vaitheeswaran
Associate Professor
School of Physics
University of Hyderabad
Hyderabad-500 046. (TS) INDIA

Ph.D Thesis

**Structure-Property Correlation Studies of
Carbonate Fluorides and Metal-Organic Energetic Solids**

Elaprolu Narsimha Rao



**ACRHEM, School of Physics,
University of Hyderabad,
Hyderabad - 500046.
Telangana, India.**